Engineering Journal

American Institute of Steel Construction

First Quarter 2015 Volume 52, No. 1

www.aisc.org

ENGINEERING JOURNAL

AMERICAN INSTITUTE OF STEEL CONSTRUCTION

Dedicated to the development and improvement of steel construction, through the interchange of ideas, experiences and data.

ENGINEERING JOURNAL (ISSN 0013-8029) is published quarterly. Subscriptions: Members: one subscription, $40 per year, included in dues; Additional Member Subscriptions: $40 per year. Non-Members U.S.: $160 per year. Foreign (Canada and Mexico): Members $80 per year. Non-Members $160 per year. Published by the American Institute of Steel Construction at One East Wacker Drive, Suite 700, Chicago, IL 60601.

Periodicals postage paid at Chicago, IL and additional mailing offices. **Postmaster:** Send address changes to ENGINEERING JOURNAL in care of the American Institute of Steel Construction, One East Wacker Drive, Suite 700, Chicago, IL 60601.

Recommended Procedures for Damage-Based Serviceability Design of Steel Buildings under Wind Loads

KEVIN ASWEGAN, FINLEY A. CHARNEY and JORDAN JARRETT

ABSTRACT

This paper provides a recommended procedure for nonstructural damage control of steel buildings under serviceability-level wind loads. Unlike traditional procedures that provide a single drift limit under a given reference load, the recommended procedure provides a decision space that spans a range of wind hazards and associated damage states. Central to the procedure are the use of shear strain in nonstructural components as the engineering demand parameter and the use of component fragility as a reference for limiting damage.

Keywords: wind, drift, serviceability, damage, fragility, performance-based engineering.

BACKGROUND

During the design of a building, the structural engineer is typically concerned with both strength and serviceability limit states. Design and detailing requirements for the strength limit states such as yielding, fracture and buckling are prescribed in the applicable building codes. However, the same building codes do not provide prescriptive requirements for the serviceability limit states. This is largely due to the noncatastrophic nature of serviceability failures, as well as the fact that serviceability issues are generally specific to a project and thus require participation from the project owner and other design team members.

Instead of providing serviceability requirements, the codes take a performance-based approach wherein only the expectations of a successful design are provided. The AISC *Specification* (AISC, 2010) defines serviceability as "a state in which the function of a building, its appearance, maintenance, durability and comfort of its occupants are preserved under normal usage." On the topic of drift, the specification states that drift "shall be evaluated under service loads to provide for serviceability of the structure, including the integrity of interior partitions and exterior cladding." ASCE 7-10 (ASCE, 2010) contains similar language, stating that "sufficient stiffness must be provided such that deflection, drift, and vibrations are limited to an acceptable level."

The lack of wind serviceability design standards has led to a wide variation in design practices across the United States. To assess the state of the practice, ASCE created the Task Committee on Drift Control of Steel Building Structures in 1984. The committee surveyed structural engineering firms and released its results in 1988 (ASCE, 1988). In general, the results from the survey showed that there was little consistency in terms of the selection of service-level wind loads, the development of mathematical models of the structural system, the selection of appropriate drift measures and the establishment of drift limits. A more recent survey, conducted in 2006 by the ASCE/SEI Committee on the Design of Steel Building Structures, found similar results (Charney and Berding, 2007). When asked to list the primary motivation for limiting drift, the respondents to the most recent survey reported, in the following order: to prevent structural damage (most common response), to prevent nonstructural damage, to control second-order (P-Δ) effects, and to limit lateral accelerations. With the possible exception of P-Δ effects (which contribute to drift), these motivations are all serviceability considerations.

One approach to improving wind drift serviceability design would be to borrow from the concepts of performance-based earthquake engineering, commonly referred to as PBEE, that are already in use for existing buildings through the provisions of ASCE 41-13 (ASCE, 2013) and that have been recommended for tall buildings (PEERC, 2010). The PBEE concept is built around quantifying hazard intensity measures, engineering demand parameters, damage measures and decision variables (repair cost, repair time or casualties) at multiple limit states. In order to account for inherent uncertainties in the process, the PBEE methodology

Kevin Aswegan, Structural Engineer, Magnusson Klemencic Associates, Seattle, WA. Email: kaswegan@mka.com

Finley A. Charney, Ph.D., P.E. Professor of Structural Engineering, Department of Civil Engineering, Virginia Tech, Blacksburg, VA (corresponding). Email: fcharney@vt.edu

Jordan Jarrett, Structural Engineering Graduate Student, Department of Civil Engineering, Virginia Tech, Blacksburg, VA. Email: jaj14@vt.edu

Paper No. 2013-14

is supported by a probabilistic framework (Moehle and Deierlein, 2004). Various government supported efforts to develop a comprehensive PBEE procedure recently cumulated with the publication of the FEMA P-58 report (FEMA, 2013a) and related materials, including a performance assessment calculation tool.

The development and advancement of performance based wind engineering (PBWE) would logically follow closely that of PBEE. However, there are significant differences related to the wind and seismic hazards, the limit states that need to be considered and the necessity (in seismic design) to explicitly include inelastic behavior associated with life-safety and collapse-prevention limit states. Paulotto, Ciampoli and Augusti (2004), Ciampoli, Petrine and Augusti (2011), and Griffis et al. (2012) proposed the adaptation of the PBEE framework to wind. Paulotto et al. and Ciampoli et al. provide probabilistic frameworks that incorporate the concepts of fragility. Fragility is also central to the FEMA P-58 PBEE procedure, as well as the procedure recommended in this paper. Griffis et al. propose multiple wind-related performance levels, dynamic nonlinear analysis of structures under wind loading and the concept of allowing inelastic behavior at more severe wind limit states. Despite the various proposals, without a coordinated government-supported effort to develop PBWE, it has not gained, nor is it likely to achieve, the same level of usage as PBEE.

The purpose of this paper is to describe a damage-based method for the evaluation and design of steel structures subjected to serviceability-level wind loads. While the proposed method falls short of PBWE as envisioned by the authors cited earlier, it does address three key issues: selection of appropriate wind loads, accurate definition and calculation of the damage measure and selection of rational damage limits. Unlike other methodologies that rely on a single wind return period or a set of established drift limits, the procedure described in the remainder of this paper follows the basic principles on serviceability that were published in 1986 (Committee on Serviceability, 1986), which states:

> *Serviceability guidelines need to be flexible and adapt*able *to different occupancies, use requirements and techniques for integrating nonstructural components. The guidelines ought to be negotiable, within limits, between the engineer, architect and building owner.*

OVERVIEW OF PROCEDURE

The procedure is based on the computation and limitation of shear deformations in nonstructural components. Features of the procedure, described in much more detail later, are as follows:

1. The procedure is developed explicitly for the serviceability assessment of tier-type structures (a structure in which levels are stacked on one another or built in tiers). This limitation is applicable because such buildings have numerous interior architectural partitions and exterior finishes that need to be protected from damage.

2. A broad wind-hazard basis is used, wherein a range of mean recurrence intervals are considered.

3. The deformation that is controlled is shear strain in nonstructural components.

4. A three-dimensional mathematical model of the building is used to perform the structural analysis and is calibrated to provide the best possible estimate of the damaging shear strain deformations in the nonstructural components. A different model would likely be used to address strength limit states.

5. The limiting shear strain is based on the concept of structural fragility and the use of fragility curves. Such curves are based on laboratory testing of nonstructural components and provide the probability of exceeding a given damage state (e.g., minor cracking of drywall partitions) given the computed shear strain.

6. The results of the serviceability analysis provide a broad basis for making decisions about controlling damage in nonstructural components but fall short of providing quantitative information on the consequences of accepting some damage.

While the procedure could be expanded to consider other wind-related serviceability limit states—such as perception of motion—and to include structural damage, the current focus is on the control of damage in nonstructural components, such as interior walls and exterior walls and finishes. Damage under seismic loads could also be controlled using the same general procedure.

WIND LOADS

Current Wind Load Design Provisions

Buildings in the United States are designed for wind loads according to the provisions of ASCE 7. The current edition, ASCE 7-10 (ASCE, 2010), provides three methods for determining wind loads for the main wind-force resisting system of a building: the directional procedure, the envelope procedure and the wind tunnel procedure. The wind tunnel procedure is generally the most accurate but also the most time-consuming and expensive. For the serviceability-level wind loads, any of the allowed procedures are suitable, provided that an appropriate mean recurrence interval (MRI) is selected.

Mean Recurrence Interval (MRI)

The mean recurrence interval is the return period for a wind event. A 10-year MRI refers to a wind event that occurs, on average, once every 10 years. A shorter MRI corresponds to lower-intensity wind loads, while a longer MRI corresponds to higher-intensity wind loads. For risk category II buildings designed according to the provisions of ASCE 7-10, the MRI is 700 years. Risk category I and III–IV buildings are designed using 300- and 1700-year MRIs, respectively. Each of these risk-related MRIs represents ultimate strength-level loading, and as such, the load factor on wind loads is 1.0. Service-level wind speeds (as used in previous editions of ASCE 7) are generally in the range of 50 to 100 years. The wind loads based on these service-level wind speeds must be factored up to strength level for the design of the main lateral load-resisting system. Similarly, the service-level wind speeds are generally factored down for serviceability considerations. It is important to note that "service"-level wind speeds and "serviceability" are not synonymous. It was never the intent in ASCE 7 to use service-level loads for serviceability.

Various authors have recognized that the service-level and, particularly, the ultimate-level wind loads are overly conservative for serviceability considerations when traditional drift limits (in the range of $H/500$, where H is the story height) are used. For this reason, Tallin and Ellingwood (1984), Charney (1990b), and Griffis (1993) proposed serviceability MRIs of 8 to 10 years. This particular MRI range is approximately the length of the average tenancy in the United States and the United Kingdom (Ellingwood and Culver, 1977). Additionally, AISC *Design Guide 3* (West, Fisher and Griffis, 2003) recommends a 10-year wind event for interstory drift checks.

Although many sources have suggested a 10-year MRI, it is recommended that a designer select a wind serviceability MRI based on the specific needs of the owner or other stakeholders relative to the use (risk category) of the building and the probability of and potential consequences of exceeding a particular damage limit state. Another factor in determining the appropriate MRI is the range and resolution of test data have has been used to establish damage limits. This important concept is discussed later in the paper in association with the use of component fragility as a damage indicator.

Recognizing the need to use a lower MRI for serviceability considerations, the commentary to Appendix C of ASCE 7-10 provides wind speed maps for 10-, 25-, 50- and 100-year MRIs. Using the 10-, 25-, 50- and 100-year wind speed maps, a designer can select the appropriate wind speed and use the provisions of ASCE 7 to determine the serviceability wind loads. When a building site is located such that it is difficult to manually determine the wind speed with the ASCE 7 maps, an online tool developed by the Applied Technology Council (ATC, 2013) can be used. This tool, using the same data that was used to generate the ASCE 7 maps, will provide wind speeds for various MRIs given a physical address or latitude and longitude.

Wind and Seismic Hazard Curves

A hazard curve is a plot showing the relationship between a hazard measure (such as wind speed or wind pressure) and likelihood of occurrence. Figure 1 shows wind hazard curves for select cities across the United States. The vertical axis shows the velocity pressure (q_z in ASCE 7-10), assuming that the wind directionality factor (K_d), the velocity pressure exposure coefficient (K_z) and the topographic factor (K_{zt}) are each equal to 1.0. The likelihood of occurrence is represented by MRI on the horizontal axis.

The wind hazard curves contain valuable information relating to service and ultimate level wind loads. For the 10-year MRI, the wind pressures are similar for the six cities shown, varying between 13.3 and 16.0 psf. Examining the wind pressures for one particular MRI, however, can be misleading. For example, in the cities of Charleston and Memphis, the wind pressures due to the 10-year MRI are equal (14.8 psf). This is not the case, however, for higher MRIs. For the 700-year MRI (ultimate-level wind loads), the wind pressure in Charleston significantly diverges from the wind pressure in Memphis. The difference is due to the fact that Charleston is located in the hurricane region of the United States. It should also be noted that due to the location of Charleston, New Orleans, and Boston along the hurricane-prone coast, where the mapped wind speed contours are tightly spaced, seemingly small changes in latitude or longitude between locations can lead to significant differences in speeds and wind pressures.

It is of some interest to compare the wind and seismic hazards, as well as to discuss the MRIs typically used for seismic serviceability. Figure 2 presents seismic hazard curves for the same six U.S. cities shown in Figure 1. These curves show 5% damped, site class B–C boundary, 1-s spectral acceleration, plotted against MRI.

While the shapes of the wind hazard curves are similar for the cities indicated, the shapes of the seismic hazard curves are quite different. The difference is most noticeable when one distinguishes between Pacific west coast and the central and eastern U.S. locations. For example, in Charleston, the 50-year spectral acceleration is only 4.5% of the 500-year value, while in San Francisco, the 50-year acceleration value is much higher at 28% of the 500-year spectral acceleration. A general conclusion from the wind and the seismic hazard curves is that seismic serviceability is not likely to be a controlling issue in the central and eastern United States and that wind serviceability is probably not a controlling issue along the Pacific west coast (except for tall buildings, where perception of motion can become a controlling design consideration).

In performance-based earthquake engineering, serviceability-level drifts are determined for events with an MRI in the range of 43 years (PEERC, 2010) to 72 years (ICC, 2012). The data to assess seismic hazard at MRIs shorter than 43 years is generally not available. It is also important to note that nonstructural and some degree of structural damage (including minor yielding of steel) is *expected* under the 43- to 72-year shaking in the western United States. For example, the Pacific Earthquake Engineering Research Center (PEERC) Tall Building Guidelines limit interstory drift to 0.5% of the story height (*H*/200) when the structure is subjected to the 43-year MRI. Other seismic serviceability drift limits are summarized by Dymiotis-Wellington and Vlachaki (2004).

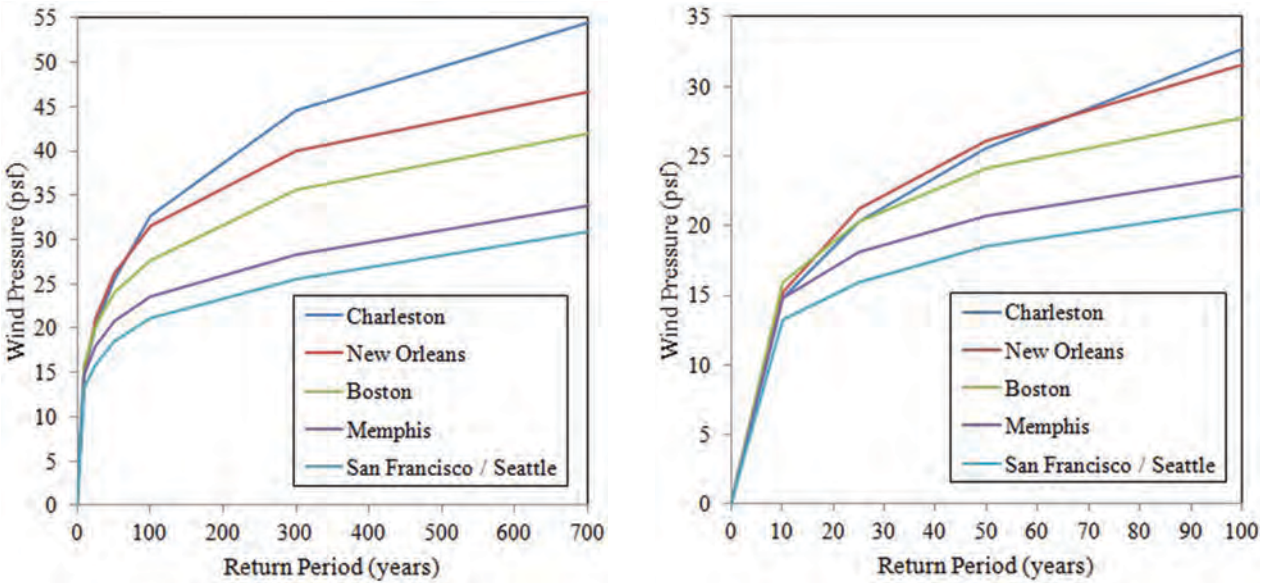

Fig. 1. Wind hazard curves for select U.S. cities: (a) return periods between 0 and 700 years; (b) return periods between 0 and 100 years.

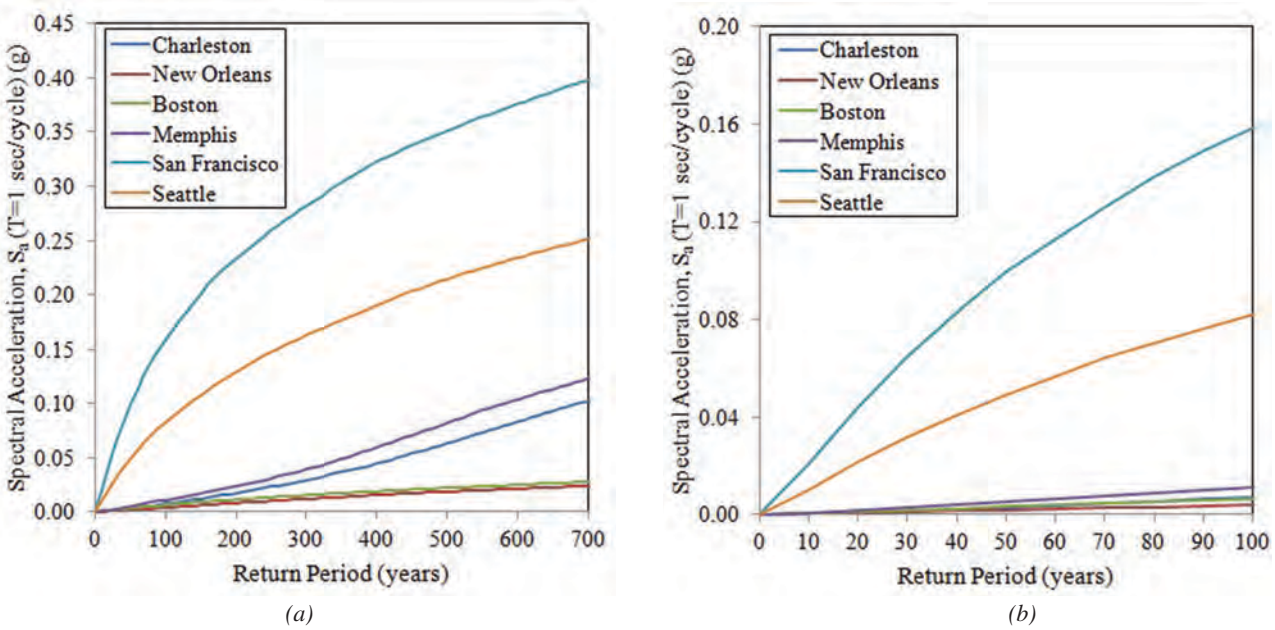

Fig. 2. Seismic hazard curves for select U.S. cities: (a) return periods between 0 and 700 years; (b) return periods between 0 and 100 years.

For wind-based serviceability, MRIs in the range of 10 to 50 years are appropriate because it is in this range of wind loads that nonstructural components will first experience damage. As described later, it is recommended that a 25-year MRI be used as the basic wind speed for wind damage serviceability because it is in this range of loading that the test-based fragility data are likely to be most reliable. Deformation demands for different wind MRIs can be estimated from those determined by the 25-year MRI as follows:

$$\delta_{Mx} = \delta_{M25} \frac{V_{Mx}^2 G_{Mx}}{V_{M25}^2 G_{M25}} \quad (1)$$

where δ_{Mx} is the deformation demand under an x-year MRI wind, δ_{M25} is the same deformation demand under the 25-year MRI wind, V is the basic wind velocity and G is the gust factor for the indicated MRIs. The gust factors are computed in accordance with Section 26.9 of ASCE 7-10. Torsional effects are calculated by applying the ASCE 7 design wind loads cases, which require 75% of the load be applied at an eccentricity of 15% of the width of the building.

PREDICTING DAMAGE IN STRUCTURES

Drift as a Damage Measure

Given that the purpose of the serviceability analysis is to prevent or control damage, the response quantity used to predict damage and the associated damage limits must be consistent with the physical mechanism that causes damage. Borrowing from the field of performance-based earthquake engineering, the following terms are used in this paper:

- ***Engineering demand parameter*** (EDP) is the computed quantity that is used as a predictor of damage. Traditional serviceability analysis uses interstory drift as the EDP. The procedure presented herein uses shear strain as the EDP.
- ***Damage state*** (DS) is a physical description of the expected damage. An example is first observation of cracking in a brick masonry veneer.
- ***Damage measure*** (DM) is the value of the EDP at which a certain damage is expected to occur. Traditional serviceability analysis used an interstory drift limit as the DM. The procedure outlined in this paper does not provide a specific limit and, instead, uses fragility curves to estimate the probability of exceeding a given damage state.

The concept of the EDP is discussed in this section of the paper. The damage measure and damage states are discussed in later sections.

Traditional EDPs include total drift, roof drift, and interstory drift (and, for other applications, floor acceleration and plastic hinge rotations are also used). Total drift is the lateral displacement of a frame at a given level with respect to a chosen datum (typically the ground). Roof drift is simply the total drift measured at the roof level. Interstory drift is the relative lateral displacement between two adjacent levels. Note that throughout this paper the term *interstory drift* is used, although the term *story drift* would also be appropriate. The drift index is the total, roof or interstory drift divided by the height over which the drift applies. For example, the interstory drift index (IDI) is the interstory drift divided by the height of the story. This same quantity is also referred to as the interstory drift ratio. Based on the surveys cited earlier, most engineers attempt to control drift by providing limiting values on the computed interstory drift or the interstory drift ratio.

The interstory drift and the interstory drift ratio are not, however, accurate measures of damage in a nonstructural component and are, therefore, not the most suitable EDPs if the purpose of the analysis is to limit damage in the nonstructural components. This is because interstory drift tracks only lateral displacement (not necessarily equal to deformation) and does not account for vertical racking or rigid-body rotation. A true damage measure for nonstructural components, accounting for both horizontal and vertical racking but excluding rigid-body rotation, would be mathematically equivalent to the in-plane shear strain in the component.

Another reason for using shear strain as the EDP is that it is the best quantity to correlate with laboratory tests on nonstructural components. These tests are typically performed by loading the specimens in pure shear and then correlating the damage, as it occurs, to the shear strain imposed on the specimen at the time the damage is observed. As described later in this paper, the same laboratory tests may produce sufficient information to establish the fragility of the tested component. The use of fragility in wind damage serviceability analysis allows the engineer not only to establish damage limits, but also to determine the probability that damage will occur if the imposed limits are reached or exceeded.

Using Shear Strain as the Engineering Demand Parameter

To alleviate the shortcoming of interstory drift as a damage measure, Charney (1990b) developed a revised damage measure, called the drift damage index, which in this paper is renamed the deformation damage index (DDI) to eliminate the reliance on horizontal drift as a damage measure. In accordance with the terminology adopted in the previous section, the DDI can be used as the EDP for the proposed method. The DDI is mathematically equal to the shear strain in a vertical rectangular panel of the structure, called a drift damageable zone, here renamed a deformation damageable

zone (DDZ). A DDZ spans between floors in the vertical direction and between column lines (real or imaginary) in the horizontal direction. For two-dimensional analysis, only the horizontal and vertical displacements are needed at the four corners (nodes) of the DDZ. For three-dimensional analysis, the two horizontal displacement components would need to be transformed into the plane of the DDZ. As shown later, this procedure can be automated by the use of special finite elements, called *damage gages*.

Conceptually, the DDZ can represent interior, nonstructural partitions (such as a gypsum wall), exterior walls or any other damageable element in a building model. When a building model is created and loaded with the appropriate wind loads, each DDZ will have an associated DDI, defined by the following equation:

$$DDI = 0.5\left[\frac{X_A - X_C}{H} + \frac{X_B - X_D}{H} + \frac{Y_D - Y_C}{L} + \frac{Y_B - Y_A}{L}\right] \quad (2)$$

where X_N is the lateral deflection at node N, Y_N is the vertical deflection at node N, H is the story height and L is the width of the DDZ (usually the bay width). These variables are shown in Figure 3. Note that the terms in Equation 2 containing X-direction lateral deflection values represent the interstory drift index. If the terms representing vertical deflection were set to zero, the DDI would be equal to the IDI.

Damage Gages

Computation of the deformation damage index can be cumbersome, particularly for three-dimensional analysis. When using a finite element analysis program, the DDI can easily be computed by placing membrane or shell elements in the desired location. For example, the DDZ shown in Figure 3a can be represented by a four-node element. When specifying the properties of this element, it is necessary to use a very low thickness and/or modulus of elasticity such that the element does not significantly contribute to the stiffness of the structure. If a shear modulus of 1.0 is used, then the reported shear stress is identical to the shear strain, and thus the DDI is automatically determined. In general, it is preferable to average the shear strains at the four corners of the element to obtain the best estimate of the DDI. It is noted that when finite elements are used to represent the DDZ, the elements can be placed in any orientation, are not restricted to vertical planes and need not be rectangular in shape.

An example of the analysis of a 10-story X-braced planar frame is provided to clarify the concepts of computing DDIs using damage gages. This example will also be used later in

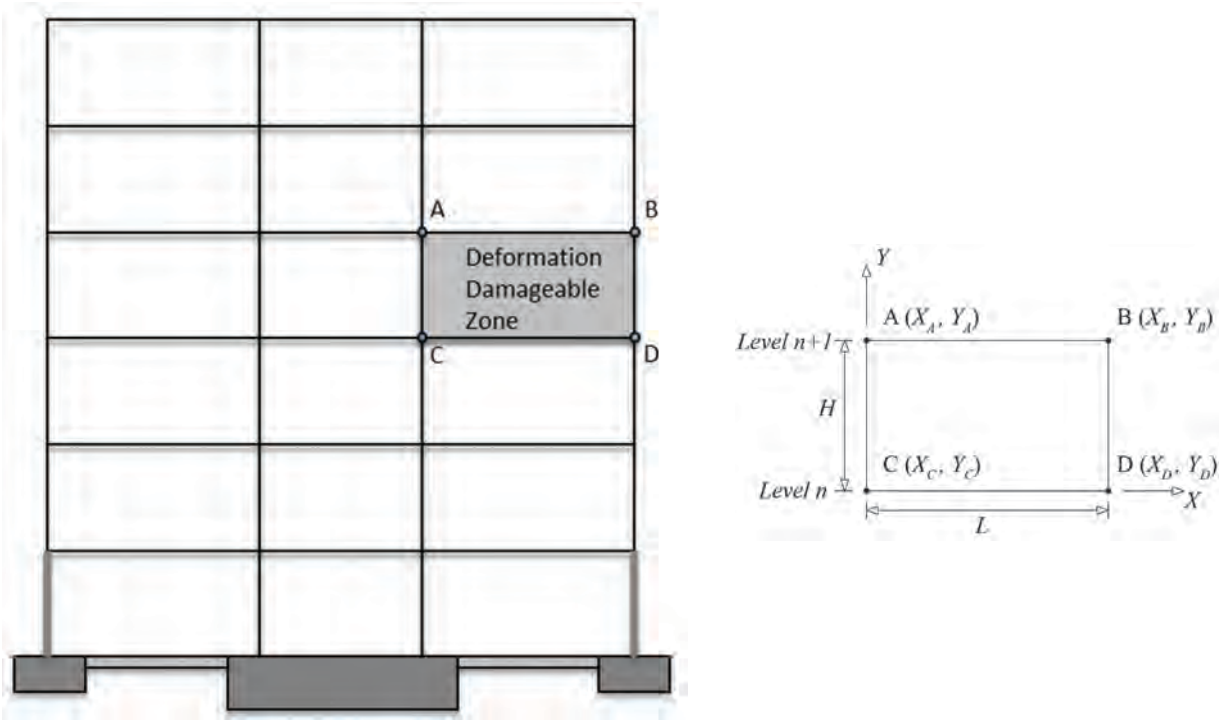

(a) *(b)*

Fig. 3. Deformation damageable zone: (a) location in frame; (b) details for calculation.

Table 1. DDI Calculations for Top Left Bay in Example 1			
Node	**Lateral Displacement (ft)**	**Vertical Displacement (ft)**	**Shear Strain**
A	0.1920	0.0000	0.00315
B	0.1911	0.0270	0.00236
C	0.1686	0.0000	0.00315
D	0.1679	0.0267	0.00235
			DDI = 0.00275
			Average shear strain = 0.00275
			Conventional interstory drift index = 0.00186

the paper to demonstrate the use of fragility in wind damage analysis. A more detailed analysis of a 12-story building is provided in Appendix A.

The example frame has three 30-ft-wide bays, and the story height is constant at 12.5 ft. The building is located in Dallas, Texas, and is designed for the ultimate-level wind speeds for that location. The column sections are W14s, and the beams range from W24s to W30s. The lateral force resisting system is an X-braced frame in the center bays in which the members are W12s. For this example, a service-level wind loading corresponding to a 25-year MRI is applied to the structure. The 25-year MRI was selected due to the hypothetical owner's preference that the serviceability design be based on a 25-year time period.

The structure is modeled in SAP2000 (Computers and Structures Inc., 2009). All connections and column bases are modeled as pinned. To calculate the DDI, a damage gage (DG) shell element is inserted into each bay, representing an interior partition wall. The elements are connected to the frame only at the four corners of each bay. The shear modulus of the DG element is assigned a unit value so that the calculated shear stress in the element is numerically equal to the shear strain. After the shear strains have been calculated for the elements, the DDI will be equal to the average of the shear strain values at the four corners of the element.

The analysis is run for the applied loads, and the nodal displacements and DDIs in the elements are determined. Table 1 contains the displacements and shear strains for the top left bay of the structure. The DDI, average shear strain and conventional interstory drift index are calculated based on the values at the nodes. Figure 4 shows the 10-story braced frame with the applied loading. The shear strain contours are plotted on each element, with the DDI labeled at the center of the element and the conventional interstory drift index labeled in parentheses. Equation 2 can also be used to calculate the DDI given the calculated nodal displacements. However, for the example, the DDI for each bay is calculated by averaging the values of the shear strain at the corners of the element.

Some important observations can be made based on the results shown in Figure 4. The first is that the DDIs in the outer bays are very different than the DDIs in the inner bay, even for the same story. For example, the DDI in the top left bay is equal to 0.00275, while the DDI in the adjacent braced bay is 0.000071 (only 2.6% of the value for the unbraced bay), despite having nearly equal conventional interstory drift indices. This difference is present, but less pronounced, at lower levels as well. A second observation is that the DDIs are significantly different from the conventional interstory drift indices (which only account for horizontal racking). For the top left bay, the conventional interstory drift index is 0.00186, which is 68% of the DDI. In the adjacent braced bay, the conventional interstory drift index is 26 times the DDI. This wide discrepancy is due to the fact that the conventional interstory drift index does not include vertical racking and does not remove the influence of rigid-body rotation. For this example, the nodes comprising the inner braced bays experience significant vertical deflections, particularly in the upper stories.

STRUCTURAL MODELING

Accurate computation of the EDP requires a mathematical model that can account for any source of deformation that contributes to the EDP. Thus, *any part* of the building-foundation system that is stressed under the wind load should, theoretically, be included in the mathematical model. This includes components of the main lateral load-resisting system, components of the gravity load-resisting system, architectural components, diaphragms, the soil-foundation system and all connections. Additionally, second-order (P-Δ) effects should be included. For example, for steel moment frames, the modeling of the columns and (possibly composite) beams should allow for unrestricted axial, flexural, shear and torsional deformation. Additionally, deformations in the panel-zone of the beam-column joints should be considered.

The importance of including all appropriate deformation sources in the structural components was illustrated in a

study performed by Charney (1990a), which quantified the relative influence of the various deformation sources on the overall lateral deflection of a frame. Using the principle of virtual work and the concept of displacement participation factors (Charney, 1991; Charney, 1993), 45 different steel structures were analyzed, ranging from 10 to 50 stories. It was found that flexural deformations are very influential in shorter, stockier structures and that axial deformations are influential in taller slender structures. Shear deformations contributed, on average, 15.6% to the overall lateral deflection. Panel zone deformations were found to constitute an average of 30.5% of the drift in a structure. A study by Berding (2006) found similar results, with panel zone deformations comprising as much as 39% of the total deformation. Based on the results of these studies, it is recommended that any structural model used to calculate deformation include the effects of axial, flexural, shear and panel zone deformations. The exclusion of any of these effects could result in the underestimation of component deformations.

Given that most commercial programs are designed to develop 3D models of building structures, it is recommended that a 3D model be used for all wind damage serviceability analyses. There are several advantages to utilizing a 3D building model, such as modeling the interaction of orthogonal building frames, and the automatic inclusion of inherent torsional response. Torsion can increase the computed shear strain in some parts of a building, while decreasing the shear strain in others. The torsional response is difficult, if not impossible, to model in 2D.

Additional modeling considerations are briefly provided in the following sections. More detailed recommendations can be found in Berding (2006).

Panel Zone Deformations

As previously discussed, panel zone deformations can constitute a significant contribution to the overall drift of a steel moment-resisting frame. There are several methods to model panel zone deformations, including the clearspan model, the

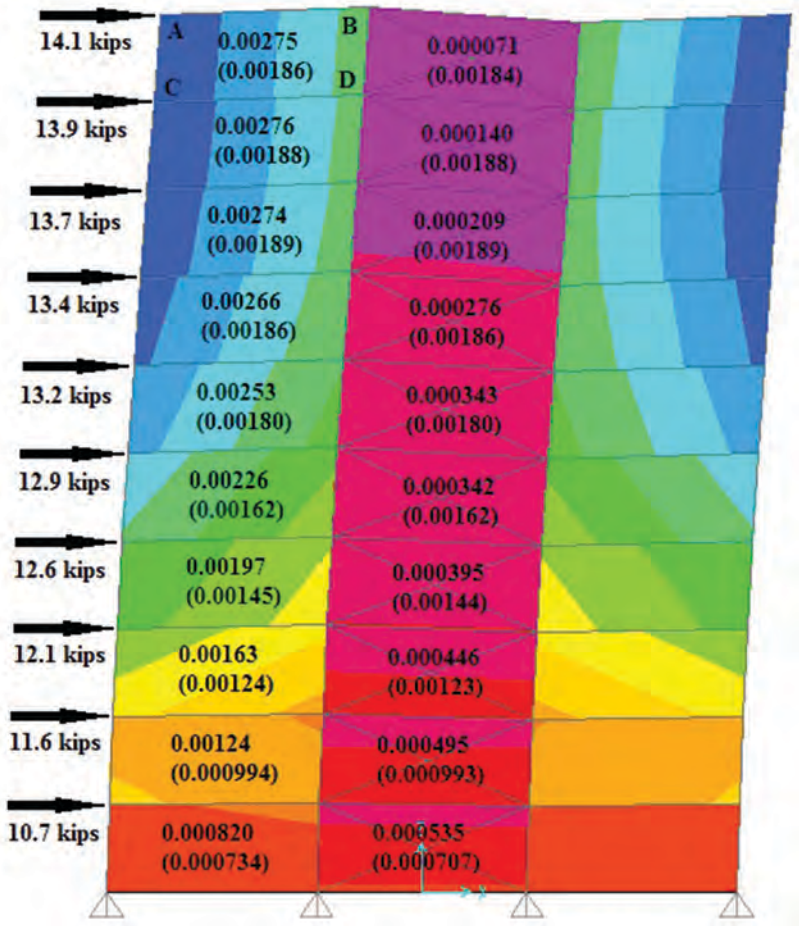

Fig. 4. Shear strains and (interstory drift indices) in a 10-story braced frame under serviceability-level wind loads.

centerline model, and more sophisticated mechanical joint models, such as the Krawinkler joint (KJ) and scissors joint (SJ) models (Charney and Marshall, 2006). The clearspan model unconservatively assumes the panel zone is infinitely rigid and should never be used. The centerline model uses center-to-center dimensions and will tend to overestimate flexural deformations and underestimate shear deformations within the beam-column joint. These effects partially offset each other, leading the centerline model to be sufficiently accurate in most situations (as long as there is no yielding in the panel zone). The KJ and SJ models are the most accurate and incorporate rigid links and rotational springs and explicitly represent both shear and flexural deformation within the beam-column joint. However, these models are somewhat difficult to implement. It is recommended that the centerline model be used when the mechanical joint models are not feasible (Charney and Pathak, 2008).

Floor and Roof Diaphragms

In most circumstances the floor and roof diaphragms may be modeled as rigid in their own plane and flexible out of plane. However, for certain structures, the out-of-plane stiffness of the diaphragms may act to couple the lateral load-resisting elements, thereby having a significant influence on lateral displacements and damage prediction.

Composite Beams

For serviceability analysis, it is generally acceptable to include some contribution from slabs, even if the beams are not designed as fully composite. The main concerns are related to the effective width of slabs to use in analysis and to the effectiveness of the slab if it is likely to be cracked in tension under serviceability wind loads. The slab can generally be broken into four moment regions under lateral loads (Schaffhausen and Wegmuller, 1977): (1) positive bending moment region—slab is located away from the column; (2) positive bending moment region—slab is adjacent to a column; (3) negative bending moment—slab is adjacent to interior column and may have compression reinforcement; and (4) negative bending moment region—slab is adjacent to exterior column and is not likely to have compression reinforcement. In general, for regions 1 and 2, the full effective slab width should be used. In a strict sense, the effective slab width should reduce to the width of the column for region 2. For regions 3 and 4, the girder properties alone should be used. In the determination of the composite moment of inertia for regions 1 and 2, the compressive strength of the concrete and the composite percentage based on the number of shear connectors should be considered. For a discussion on effective width, the reader is directed to Vallenilla and Bjorhovde (1985).

Gravity System

In some cases it may be worthwhile to include the additional lateral stiffness of the gravity system in the structural model. To do so, the engineer must estimate realistic moment-rotation relationships for the connections. *Design Guide 8* (Leon, Hoffman and Staeger, 1996) provides guidance on the calculation of the connection's rotational stiffness, as does the ASCE Standard 41-13 (ASCE, 2013). An example of the possible influence of the stiffness and strength of the gravity connections is shown in Figure 5, which is taken

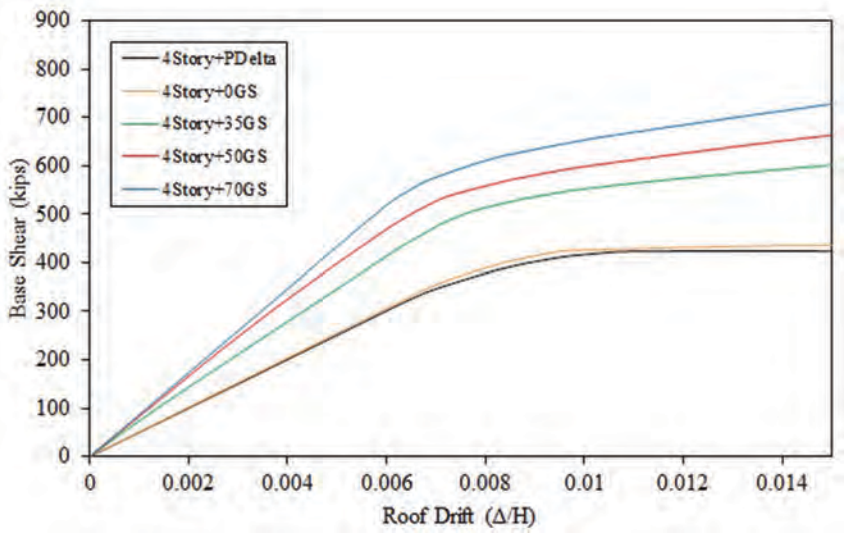

Fig. 5. Nonlinear static pushover curves for a four-story frame.

from analyses of a four-story steel moment frame (Flores and Charney, 2013). The different curves from nonlinear static pushover analysis represent different assumptions regarding the effective strength and stiffness of the connections from the beams to the columns. The curve marked "4Story+PDelta" represents the lateral system only, and the curve marked "4Story+35GS" assumes that the gravity connections have 35% of the stiffness of the full beam section. As may be seen, there is a considerable increase in system stiffness and strength when the gravity system is considered.

While it is recommended that the gravity system be included in the wind serviceability analysis, it is recognized that neglecting the gravity system will be conservative.

Architectural Components

The influence of architectural components on the response of a building under serviceability wind loads depends on the number of components, the location and orientation of the components, the basic in-plane unit stiffness of the component, the method of attachment and the total contributing stiffness of components relative to the overall stiffness of the lateral load-resisting system. In this sense, an infill masonry wall in a three-story building would significantly influence the computed response, but drywall partitions in a 30-story office building would likely provide negligible stiffness. Due to uncertainties in establishing component location and to estimating the component stiffness, it is recommended that architectural components not be included in wind drift serviceability analysis.

Second-Order (P-Δ) Effects

Second-order effects typically increase lateral deflection and should always be included in the model. When modeling second-order effects, a decision must be made concerning gravity loads. Actual live load values are typically much less than design values (Ellingwood and Culver, 1977), making it unreasonable to use design live loads in a serviceability-based P-Δ analysis. It is recommended that unfactored dead loads be used with the mean expected live loads, taken from live load surveys. Table C4-2 of ASCE 7 (2010) contains survey loads for office buildings, residences, hotels and schools.

Foundation

The significance of the flexibility of the foundation on nonstructural deformations depends on several factors, including the composition of the soil and the characteristics of the foundation itself. Consider, for example, the simple structure shown in Figure 6. Here, slight rotation of the mat foundation under the X-braced frame would contribute to the vertical racking in the adjacent bays, as would the axial elongation in the basement columns. Additionally, the P-Δ

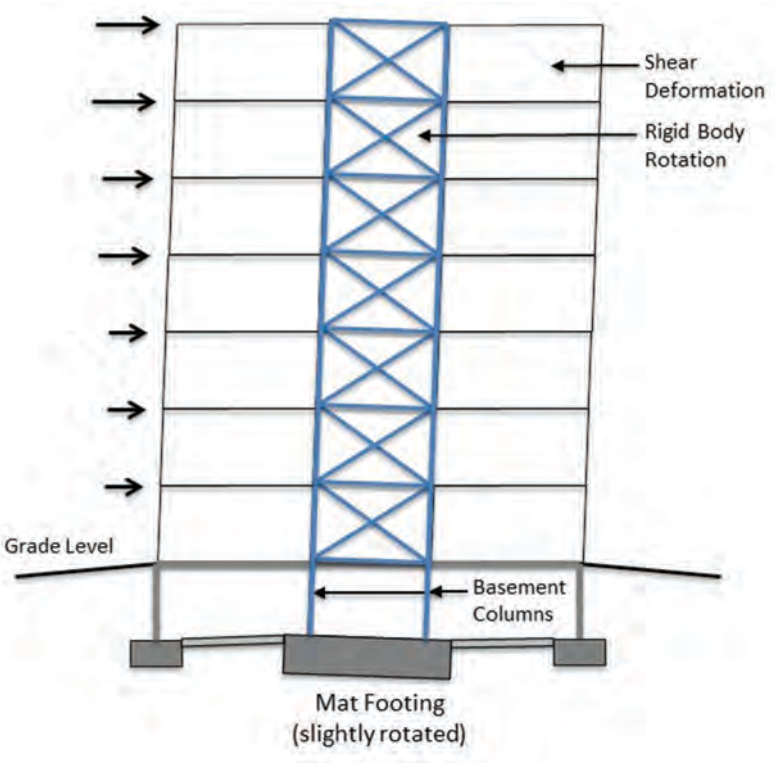

Fig. 6. Foundation modeling concerns.

Table 2. Selected Recommended Shear Strain Limits (Griffis, 1993)			
Building Element	**Supporting Structural Element**	**Deformation Type**	**Recommended Limit**
Brick veneer	Wind frame	Shear strain	*H*/400
Concrete masonry unreinforced (exterior)	Wind frame (1 story)	Shear strain	*H*/600
	Wind frame (2 story)	Shear strain	*H*/400
Concrete masonry reinforced (exterior)	Wind frame (1 story)	Shear strain	*H*/200
	Wind frame (2 story)	Shear strain	*H*/400
Gypsum drywall, plaster	Wind frame	Shear strain	*H*/400
Brick (interior partition)	Wind frame	Shear strain	*H*/1250

effects would be more significant if the foundation and subgrade structure were included in the model. Thus, the shear strains, when used as the EDP, could be significantly underestimated if the mat rotation and the basement columns were not included in the mathematical model.

DAMAGE MEASURES

As already discussed in this paper, the engineering demand parameter (EDP) that is recommended for controlling damage in nonstructural components is shear strain. Such strains develop from the three-dimensional displacements that occur at the attachment points between the structure and the nonstructural component. Given a structural model, the shear strains can be computed with relative ease, either manually or by use of the damage gages described previously.

To control damage, the damage measure (DM) must be compatible with the EDP. Thus, it is logical that those levels of shear strain that cause some level of observable damage in nonstructural components be used as the limiting damage measure. As already mentioned, interstory drift or interstory drift ratios are not suitable as damage measures because they include rigid-body rotations (which do not cause damage) and exclude vertical racking (which does cause damage).

Conventional Drift Limits

Interstory drift limits have historically been based on rules-of-thumb, and ASCE (1988) reported structural engineers to be employing drift limits ranging from $H/600$ to $H/200$, where H is the story height. A review of the literature reveals a commonly suggested interstory drift limit of $H/500$, which is also recommended in *Design Guide 3* (West et al., 2003). However, it should be noted that these limits are generally invariant across material type. Galambos and Ellingwood (1986) provide a broad set of interstory drift limits that are tied to specific serviceability problems that can arise. These limits range from $H/1000$ (cracking of brickwork) to $H/100$ (damage to lightweight partitions, impaired operation of windows and doors, etc.). Within this range, the limit of $H/500$ is associated with the cracking of partition walls. The limits provided by Galambos and Ellingwood, however, are not connected to any specific structural or nonstructural material.

The preceding discussion illustrates the wide range of applied interstory drift limits in historical use. However, these limits are typically not modified by engineers to account for specific structural or nonstructural materials, as limits on shear strain would be. Rather, a designer may indiscriminately employ the same interstory drift limit for each bay in the building, or even for two or more buildings with different owner preferences, functions, and material makeup. For a more accurate measure of component damage, rational shear strain limits intended to control damage to a particular material should be defined on the basis of the material's properties. For example, if the goal is to prevent damage to interior gypsum wall partitions, then the damage limit should be defined based on test data of gypsum wallboard. Using rational damage limits will likely lead to a separate shear strain damage limit for each damageable material in a building.

Griffis (1993) recognized this problem and recommended limiting shear strains in a variety of nonstructural components. Selected values are repeated in Table 2. The recommended limits are those that are expected to be at the threshold of causing observable damage in the given building element and are recommended for use in association with a 10-year MRI. The use of limiting strains as shown in Table 2 is a step in the right direction, but there is no information provided as to the type of damage that could be expected, nor is any information provided as to the likelihood that the damage would occur if the recommended drift limit were to be achieved under the designated wind load.

Fragility

A more rational approach for damage control is based on the concept of *fragility*, specifically, *fragility curves*. A fragility

curve is a mathematical relationship between an engineering demand parameter (e.g., shear strain in nonstructural components) and the probability of attaining some observable damage measure. The curves are based on laboratory test data, usually from a number of sources. Appendix B contains additional information on fragility curve theory. Figure 7 contains three sample fragility curves for gypsum wallboard, obtained from the Performance Assessment Calculation Tool (PACT) developed by the Applied Technology Council (FEMA, 2013b) as a part of FEMA P-58 (FEMA, 2013a). The horizontal axis shows the EDP of deformation damage index (or shear strain), and the vertical axis contains the probability of exceeding one of the three damage states shown. Note that many of the fragilities found in PACT use interstory drift ratio as the EDP. As long as racking tests were performed on the individual component to develop the fragilities, the interstory drift ratio will be equal to shear strain, and therefore, those fragilities can be used in this procedure where the EDP is shear strain. The blue curve in Figure 7 represents damage state 1 (DS1), which is screws popping out and minor cracking. The orange curve (DS2) is DS1 plus moderate cracking or gypsum crushing, and the maroon curve (DS3) is DS2 plus significant cracking or crushing. From Figure 7, it may be seen that for a deformation damage index of 0.005 (1/200) corresponding to a hypothetical 10-year MRI, there is a 7.0% probability of no damage occurring, a 71% probability of the gypsum drywall experiencing DS1, a 19% probability of DS2, and a 2.6% probability of DS3.

One of the advantages of the fragility approach is that a *design space* of information is provided instead of information on just one specific damage limit or wind speed. In this sense, the entire plot represents the design space, and the DDIs that could occur under several MRIs can be examined. In addition to the 10-year MRI previously discussed, Figure 7 also contains vertical lines representing the DDIs under the loads corresponding to the 25- and 50-year wind loads. Note that the location of the wind speed MRI lines will shift laterally on the plot when different geographic locations are chosen. Using this design space, the engineer can gather probabilistic information for a range of MRIs.

Example of 10-Story Frame, Continued

The example of the 10-story frame is now continued to illustrate the use of fragility in the context of engineering demand parameters, damage measures and damage states.

After the MRI is selected, the wind loads are determined, the building is modeled and the DDIs are calculated (see Figure 4), the next step is to select damage limits and then compare the DDIs to these limits. For this example, the deformation damageable zones represent interior gypsum wall partitions with metal studs. It is the owner's preference that there is no greater than a 30% chance of minor damage (DS1) to each partition under the 25-year wind loads.

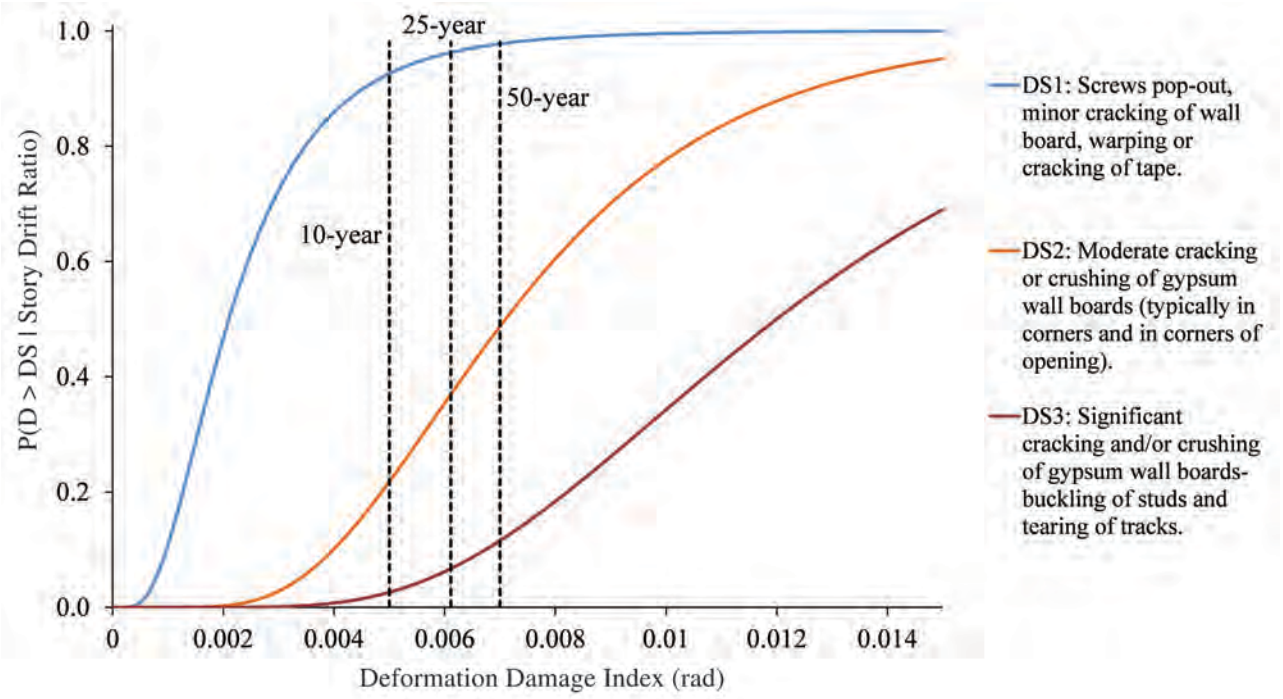

Fig. 7. Gypsum wallboard fragility curves (PACT).

Using the fragility information from Table 5 of Appendix B (median demand = 0.0021, dispersion = 0.6), it is determined that a DDI of 0.00153 corresponds to a probability of exceedance of DS1 of 30%. (See Appendix C for details on computing such probabilities.) Based on the DDIs shown in Figure 4, the outside bays in the top eight levels exceed the limit, while none of the interior (braced) bays do so.

An alternative to comparing the maximum DDI to some limit from the fragility curve is to look at the range of the DDIs in all of the bays of interest. Figure 8 shows the fragility curve for DS1 for gypsum drywall. The middle 50% range of DDIs is shown on the figure, along with the mean of the DDIs for the 10-, 25-, and 50-year wind loads. This figure provides information concerning multiple MRIs. For the 10-year wind loads, the average DDI corresponds to a 10.5% probability of exceeding DS1; for the 25-year MRI, this probability is 18.7%; for the 50-year MRI, it is 26.2%. This constitutes a design space with which the engineer can make a decision based on performance at multiple MRIs.

PERFORMANCE ASSESSMENT AND DECISION MAKING

One of the most challenging aspects of the recommended methodology is making design decisions based on the results of the damage assessment. After the damage assessment has been conducted, the designer must come to a decision concerning the acceptability of the design (either it is adequate or it is not). The decision space (probabilities of damage relative to deformation levels due to various MRIs) aids in this decision-making process, but it is the responsibility of the engineer to set acceptability thresholds (e.g., no more than a 30% probability of exceedance due to the 25-year MRI) in coordination with the architect, building owner and other stakeholders. As discussed later, it will likely be helpful to connect the probability of damage to cost of repair or replacement, thus providing a decision variable in terms of cost, which is typically more useful to a building owner than shear strain or damage probabilities.

OPTIONS FOR REDESIGN IF PERFORMANCE TARGETS ARE NOT MET

In many cases, the designer will find that the structure does not meet the required serviceability requirements and that the system must be re-proportioned to meet such requirements. Unfortunately, it may be difficult to determine which members of the main lateral load-resisting system to modify (make stiffer or more flexible). Virtual work-based procedures (Velivasakas and DeScenza, 1983; Baker, 1990, Charney, 1991, 1993) have been developed to simplify this task and are included in some commercial analysis programs such as SAP2000 (Computers and Structures, 2009), and RAM Frame (Bentley, 2013). These procedures can provide information as to which elements to modify and, even further, to recommend which section properties within these elements (axial area, shear area, moment of inertia) to modify. These simple virtual work methods are the basis of much more complex automated optimization procedures that have been used in tall building design (Chan, Huang and Kwok, 2010).

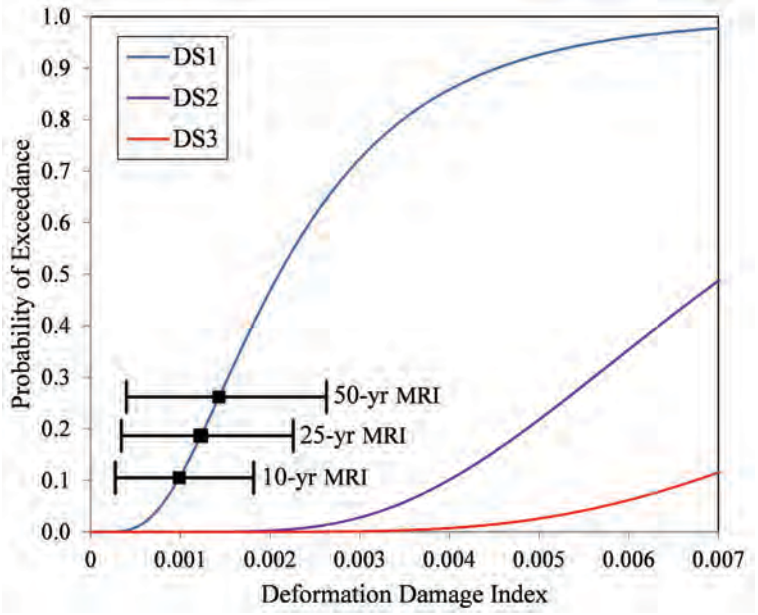

Fig. 8. Middle range of DDIs for the 10-story building.

APPLICATION TO THE FEMA P-58 METHODOLOGY

While the FEMA P-58 (FEMA, 2013a) methodology was developed for seismic response of structures, the procedure and its four goals could easily be adapted to the wind serviceability procedure discussed previously. The FEMA P-58 methodology provides a PBEE framework with four major goals: (1) to include the behavior of nonstructural components; (2) to investigate response at a global level; (3) to relate damages to more meaningful consequences, such as repair time, repair costs, casualties and injuries and potential for unsafe placards; and (4) to account for uncertainties and variations within structural analysis.

The first goal, to include the effects of nonstructural components, is already a crucial part of the wind serviceability procedure presented in this paper, as well as the P-58 procedure. However, the other three P-58 goals could be added to the previous procedure to provide more robust results. The P-58 process gives its final results in terms of the global consequences, using the idea of a building performance model. This model is a collection of information about the structure needed to determine the consequences of a structure under loading. This information includes, among other things, a list of all the structural and nonstructural components in the structure and their potential damage states and consequences. Each individual component will have a set of fragility curves developed for a discrete number of damage states, as discussed previously in this paper. For each of these damage states, the time and cost needed to repair that component under the particular level of damage will be estimated as well.

The wind serviceability procedure developed earlier describes how to relate structural response to component damage through the use of fragility. The FEMA P-58 methodology can be used to take this process one step further and relate the component damages to the global consequences. The P-58 methodology includes hundreds of fragilities for both structural and nonstructural components, as well as their corresponding consequences. By using these fragilities along with their corresponding consequences, the end result will describe the global response and be significantly more meaningful to decision makers because the results will be in terms of repair cost and repair time (time that the structure must be vacated to allow for repair).

This seismic-based methodology could be applied to the wind serviceability procedure because the main input is building information and response. The building information (i.e., shear strains) will be the same regardless of what loads are applied to it, and instead of using the structural response from ground motions, the user could input structural response from wind loads. Traditionally, the P-58 procedure finds the building response under a suite of ground motions and then expands the data using a determined level of dispersion and Monte Carlo simulation (in order to account for variability in seismic analyses). For the wind serviceability procedure, this process could be applied to account for uncertainty in selecting an appropriate serviceability MRI, as discussed earlier. A number of MRIs could be analyzed (e.g., from 10 to 50 years), and a range of possible behaviors could be determined. This range of responses would be converted into potential damages, which will be converted into a distribution of probable consequences.

The P-58 procedure will also be useful if initial targets are not met, as an alternative option to the virtual work methods described in the previous section. When the results are displayed in the corresponding software—the PACT program (FEMA, 2013b)—the consequences are broken down by component. The program determines which components are causing the most problems and have the highest influence on repair cost and time. Along with the global consequences, this methodology could provide valuable information for the engineer to decide which components should be the focus of the redesign.

SUMMARY AND CONCLUSIONS

In this paper, a rational method for the wind serviceability design of steel structures is described. The process includes the calculation of appropriate service loads, accurately modeling all significant sources of deformation and stiffness and the determination of rational shear strain limits based on material test data and fragility curves.

The use of fragility curves combined with an accurate structural model allows the structural engineer more confidence with respect to the building's performance under serviceability level wind loads. Using the recommended procedure, the engineer can estimate probabilities of damage and potentially link these probabilities to cost and repair time, which are meaningful decision variables for owners and decision makers.

The following is a summary of the steps in the procedure recommended in this paper. The proposed method is general and can be adapted for different applications.

1. *Select an appropriate mean recurrence interval.* Various MRIs have been suggested, typically ranging between 10 and 50 years. While the length of the MRI could be adjusted after collaboration with the building owner or decision maker, it is recommended that a basic 25-year wind speed be used as a standard so that the DDIs calculated are generally in the range of the test data used to develop fragility curves for common nonstructural components. Different MRIs may be used for different levels of nonstructural component protection, as appropriate.

2. *Determine wind speed and loading.* The wind speed

corresponding to selected MRIs can be found in ASCE 7-10. Alternatively, there are equations available in the literature to convert between wind speeds associated with a 50-year MRI and wind speeds associated with other MRIs (Peterka and Shahid, 1998). The service wind loads can be determined using the applicable building code.

3. *Accurately model the structure.* The structural model should include all significant sources of deformation and lateral stiffness. The deformation source should include axial, shear, flexural and panel zone deformations, when appropriate. Engineering judgment should be used to determine sources of lateral stiffness to include with the bare frame stiffness. Possible additional lateral stiffness sources include connection flexibility, diaphragm stiffness and gravity frame stiffness. Direct modeling of the soil–foundation interface should also be considered.

4. *Calculate the deformation damage index.* The damage measure for nonstructural components should include vertical racking deformation as well as horizontal racking. For this reason, the DDI should be used instead of the conventional interstory drift index (measuring only horizontal racking). The use of damage gages is recommended because they are easily implemented in most commercial software.

5. *Select rational damage limits.* The deformation damage index should be compared to damage limits that are determined on a rational and consistent basis. In this paper, fragility curves are recommended as the source of information regarding damage to nonstructural components due to shear strain (DDI).

6. *Compare the DDIs with the damage limits.* The calculated DDIs for each bay should be compared with the damage limits determined with fragility curves. Stiffness can be added or subtracted from the structure at locations determined by the engineer.

7. *Repeat steps 1–6 until an economical design is achieved or other loading cases control.*

ACKNOWLEDGMENTS

The authors acknowledge the comments and contributions of the ASCE/SEI Committee on Design of Steel Building Structures. The authors also acknowledge the work of Virginia Tech graduate student Johnn Judd for his work on the wind hazard curves presented in this paper. Funding for authors K. Aswegan and J. Jarrett was partially provided by the Charles E. Via Endowment of the Virginia Tech Department of Civil and Environmental Engineering and by a grant from the National Institute of Standards and Technology (NIST).

SYMBOLS

G	Shear modulus
G_{M25}	Wind gust factor under 25-year MRI
G_{Mx}	Wind gust factor under x-year MRI
H	Interstory height
L	Width of deformation damage zone
K_d	Wind directionality factor (ASCE 7)
K_z	Velocity pressure exposure factor (ASCE 7)
K_{zt}	Topographic factor (ASCE 7)
M	Number of specimens in a set of test data
$P(Z > z)$	Probability of exceedance during time period, T
T	Time period if interest for computing probability of exceedence
V_{M25}	Wind speed under 25-year MRI
V_{Mx}	Wind speed under x-year MRI
X_i	X-coordinate of node i = A, B, C or D of drift damage zone
Y_i	Y-coordinate of node i = A, B, C or D of drift damage zone
i	Rank of sorted set of test data
p_i	Probability of exceedance associated with data point i
q_z	Wind velocity pressure (ASCE 7)
δ_{M25}	Deformation parameter under 25-year MRI
δ_{Mx}	Deformation parameter under x-year MRI
λ	Mean of the natural log of the data set
ξ	Standard deviation of the natural log of the data set (dispersion)

REFERENCES

Applied Technology Council (2013), Wind Speed website, www.atcouncil.org/windspeed.

AISC (2010), *Specification for Structural Steel Buildings,* ANSI/AISC 360-10, American Institute of Steel Construction, Chicago, IL.

Algan, B. (1982), *Drift and Damage Considerations in Earthquake-Resistant Design of Reinforced Concrete Buildings*, PhD Dissertation, Department of Civil Engineering, University of Illinois, Urbana-Champaign, IL.

ASCE (1988), "Wind Drift Design of Steel-framed Buildings: State-of-the-Art Report," *Journal of Structural Engineering*, Vol. 114, No. 9, pp. 2085–2108.

ASCE (2010), *Minimum Design Loads for Buildings and Other Structures*, ASCE 7, American Society of Civil Engineers, Reston, VA.

ASCE (2013), *Seismic Evaluation and Retrofit of Existing Buildings*, ASCE 41, American Society of Civil Engineers, Reston, VA.

Baker, W.D. (1990), "Sizing Techniques for Lateral Systems in Multi-Story Buildings," *Proceedings of the 4th World Congress on Tall Buildings*, Council on Tall Buildings and Urban Habitat, pp. 857–868.

Bentley (2013), www.bentley.com/en-US/Products/RAM+Frame/.

Berding, D.C. (2006), *Wind Drift Design of Steel Framed Buildings: An Analytical Study and a Survey of the Practice*, M.S. Thesis, Department of Civil and Environmental Engineering, Virginia Tech, Blacksburg, VA.

Chan, C.M., Huang, M.F. and Kwok, K.C.S. (2010), "Integrated Wind Load Analysis and Stiffness Optimization of Tall Buildings with 3D Modes," *Engineering Structures*, Vol. 31, pp. 1252–1261.

Charney, F.A. (1990a), "Sources of Elastic Deformation in Laterally Loaded Steel Frame and Tube Structures," *Proceedings of the 4th World Congress on Tall Buildings*, Council on Tall Buildings and Urban Habitat, Bethlehem, PA, pp. 893–915.

Charney, F.A. (1990b), "Wind Drift Serviceability Limit State Design of Multistory Buildings," *Journal of Wind Engineering & Industrial Aerodynamics*, Vol. 36, No. 1–3, pp. 203–212.

Charney, F.A. (1993), "Economy of Steel Framed Buildings through Identification of Structural Behavior," *Proceedings of the Spring 1993 AISC Steel Construction Conference*, Orlando, FL.

Charney, F.A. and Berding, D.C. (2007), "Analysis and Commentary on the Results of a Nationwide State-of-the-Practice Survey on Wind Drift Analysis and Design," *Proceedings of the 2007 Structures Congress*, Long Beach, CA, pp. 1–10.

Charney, F.A. and Marshall, J. (2006), "A Comparison of the Krawinkler and Scissors Models for Including Beam-Column Joint Deformations in the Analysis of Moment-Resisting Steel Frames," *Engineering Journal*, Vol. 43, No. 1, pp. 31–48.

Charney, F.A. and Pathak, R. (2008), "Sources of Elastic Deformation in Steel Frame and Framed-Tube Structures: Part 1: Simplified Subassemblage Models," *Journal of Constructional Steel Research*, Vol. 64, No. 1, pp. 87–100.

Ciampoli, M., Petrine, F. and Augusti, G. (2011), "Performance Based Wind Engineering—Towards a General Procedure," *Structural Safety*, Vol. 33, pp. 367–378.

Committee on Serviceability Research (1986), "Structural Serviceability: A Critical Appraisal and Research Needs," *Journal of Structural Engineering*, Vol. 112, No. 12, pp. 2646–2664.

Computers and Structures Inc. (2009), *SAP2000* (version 14.0.0), CSI, Berkeley, CA.

Dymiotis-Wellington, C. and Vlachaka, C. (2004), "Serviceability Limit State Criteria for the Seismic Assessment of R/C Buildings," *Proceedings of the 13th World Congress on Earthquake Engineering,* Vancouver, BC.

Ellingwood, B.R. and Culver, C.G. (1977), "Analysis of Living Loads in Office Buildings," *Journal of the Structural Division*, Vol. 103, No. 8, pp. 1551–1560.

FEMA (2012), "2009 NEHRP Recommended Seismic Provisions: Design Examples," FEMA P-751, prepared by the Building Seismic Safety Council for FEMA, Washington, DC.

FEMA (2013a), "Seismic Performance Assessment of Buildings: Volume 1—Methodology," FEMA P-58-1, prepared by the Applied Technology Council for FEMA, Washington, DC.

FEMA (2013b), "Seismic Performance Assessment of Buildings: Volume 3—Supporting Electronic Materials and Background Documentation," FEMA P-58-3, prepared by the Applied Technology Council for FEMA, Washington, DC.

Flores, F. and Charney, F.A. (2014), "Influence of Gravity Framing on the Seismic Performance of Steel Moment Frames," *Journal of Constructional Research*, Vol. 101, pp. 351-362.

Galambos, T.V. and Ellingwood, B.R. (1986), "Serviceability Limit States: Deflection," *Journal of Structural Engineering*, Vol. 112, No. 1, pp. 67–84.

Griffis, L.G. (1993), "Serviceability Limit States Under Wind Loads," *Engineering Journal*, Vol. 30, No. 1, pp. 1–16.

Griffis, L.G., Patel, V., Muthukumar, S. and Baldava, S. (2012), "A Framework for Performance-Based Wind Engineering," *Proceedings of the ATC-SEI Advances in Hurricane Engineering Conference*, Miami, FL.

ICC (2012), *ICC Performance Code for Buildings and Facilities*, International Code Council, Washington, DC.

Lee, T., Kato, M., Matsumiya, T., Suita, K. and Nakashima, M. (2006), "Seismic Performance Evaluation of Non-structural Components: Drywall Partitions," *Earthquake Engineering Structural Dynamics*, Vol. 36, No. 3, pp. 367–382.

Leon, R.T., Hoffman, J.J. and Staegar, T. (1996), *AISC Design Guide 8: Partially Restrained Composite Connections*, American Institute of Steel Construction, Chicago, IL.

Microsoft Corporation (2013). *Microsoft Excel*, Microsoft, Redmond, WA.

Miranda, E. and Mosqueda, G. (2013), "Seismic Fragility of Building Interior Cold-Formed Steel Framed Gypsum Partition Walls," *Background Document,* FEMA P-58/BD-3.9.2, Applied Technology Council, Redwood City, CA.

Moehle, J. and Deierlein, G.G. (2004), "A Framework Methodology for Performance-based Earthquake Engineering," *Proceedings of the 13th World Conference on Earthquake Engineering*, Vancouver, CA.

O'Brien, W., Memari, A., Kremer, P. and Behr, R. (2012), "Fragility Curves for Architectural Glass in Stick-Built Glazing Systems," *Earthquake Spectra*, Vol. 2, No. 28, pp. 639–665.

Parametric Technology Corporation (2007). *Mathcad*, PTC, Needham, MA.

Paulotto, C., Ciampoli, M. and Augusti, G. (2004), "Some Proposals for a First Step Towards a Performance Based Wind Engineering," *Proceeding of 1st International Forum in Engineering Decision Making*, Stoos, Switzerland.

PEERC (2010), *Guidelines for Performance-Based Seismic Design of Tall Buildings*. Report 2010/05, November 2010, prepared by the TBI Guidelines Working Group, Pacific Earthquake Engineering Research Center, University of California, Berkeley, CA.

Peterka, J.A. and Shahid, S. (1998), "Design Gust Wind Speeds in the United States," *Journal of Structural Engineering*, Vol. 124, No. 2, pp. 207–214.

Porter, K., Kennedy, R. and Bachman, R. (2007), "Creating Fragility Functions for Performance-based Earthquake Engineering," *Earthquake Spectra*, Vol. 23, No.2, pp. 471–489.

Schaffhausen, R. and Wegmuller, A. (1977), "Multistory Rigid Frames with Composite Girders Under Gravity and Lateral Forces," *Engineering Journal*, 2nd Quarter, pp. 68–77.

Tallin, A. and Ellingwod, B.R. (1984), "Serviceability Limit States: Wind Induced Vibrations," *Journal of Structural Engineering*, Vol. 110, No. 10, pp. 2424–2437.

Vallenilla, C. and Bjorhovde, R. (1985), "Effective Width Criteria for Composite Beams," *Engineering Journal*, 4th Quarter, pp. 169-175.

Velivasakis, E. and DeScenza, R. (1983), "Design Optimization of Lateral Load Resisting Frameworks," *Proceedings of the 8th Conference on Electronic Computation*, American Society of Chemical Engineers, pp. 130–143.

West, M., Fisher, J. and Griffis, L. (2003), *AISC Design Guide 3: Serviceability Design Considerations for Steel Buildings*, American Institute of Steel Construction, Chicago, IL.

APPENDIX A

Example of a 12-Story Perimeter Moment Resisting Frame

In this example, a 12-story, unsymmetrical, steel-framed office building located in Charleston, South Carolina, is analyzed. This building, with slightly different properties, is also used in the Analysis chapter of FEMA P-751 (2012). The first story is 18 ft tall, and the remaining stories are 12.5 ft. The building contains setbacks at levels 5 and 9. At the lower levels of the building, there are seven bays spaced at 30 ft in the east–west direction and seven bays spaced at 25 ft in the north–south direction. The lateral system is composed of perimeter steel moment-resisting frames.

The wind loads are calculated using the ASCE 7 directional procedure (2010). After consultation with the owner of the building, it was determined that a 10-year wind event would be the basis for the serviceability design due to the fact that this is approximately the length of the average tenancy. For completeness, however, results for a 25-year MRI are also provided at the owner's request. The design wind speed of 146 mph and the 10-year MRI serviceability wind speed of 76 mph are determined with the aid of the Applied Technology Council's wind speed calculator. The structure is modeled in SAP2000, and the loads are applied at the nodes. Damage gage elements were added to the exterior corners of the building to represent glazing (glass curtain wall) or drywall and around the interior core (elevator and stairs) to represent ordinary masonry walls or drywall. While the use of drywall on the exterior is not likely for any building, the DDIs computed for these damage gages could be used to represent drywall in unknown or arbitrary locations. Figure A.1 shows two views of the structural model. The vertical shaded elements represent the damage gages located at the perimeter and in the interior of the structure.

Figure A.2 shows the building model with the perimeter DDIs labeled on each damage gage. As expected, the highest DDIs (0.00276, or $1/362$) are found in the first story. Figure A.3a shows the drywall fragilities for DS1 and DS2, together with the maximum DDIs for the 10- and 25-year

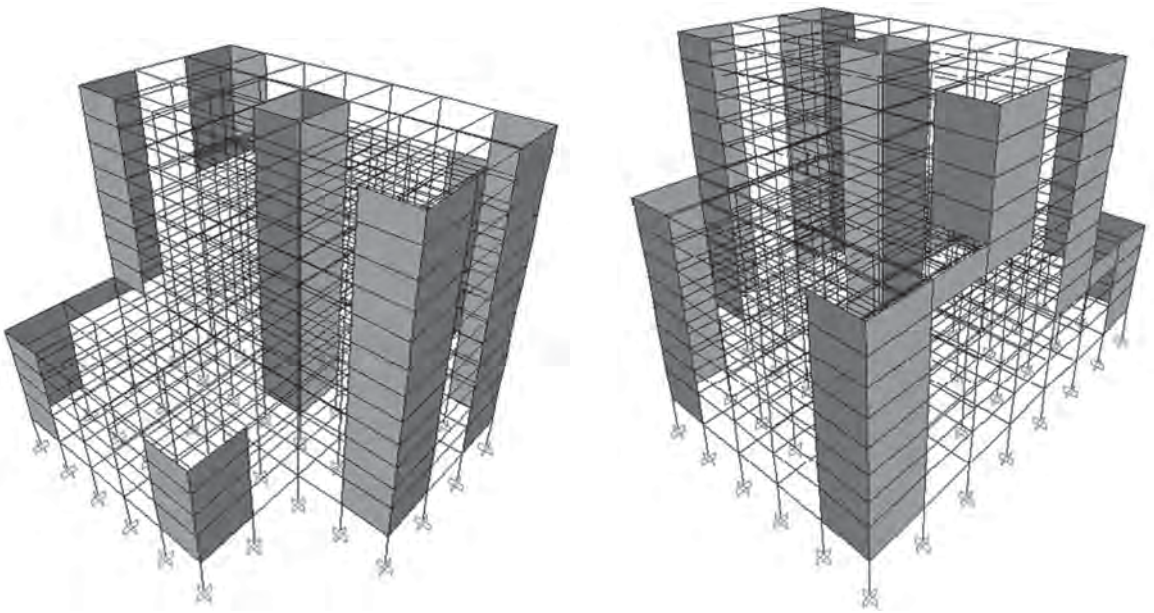

(a) *(b)*

Fig. A.1. Model of 12-story building: (a) from south to west; (b) from north to east.

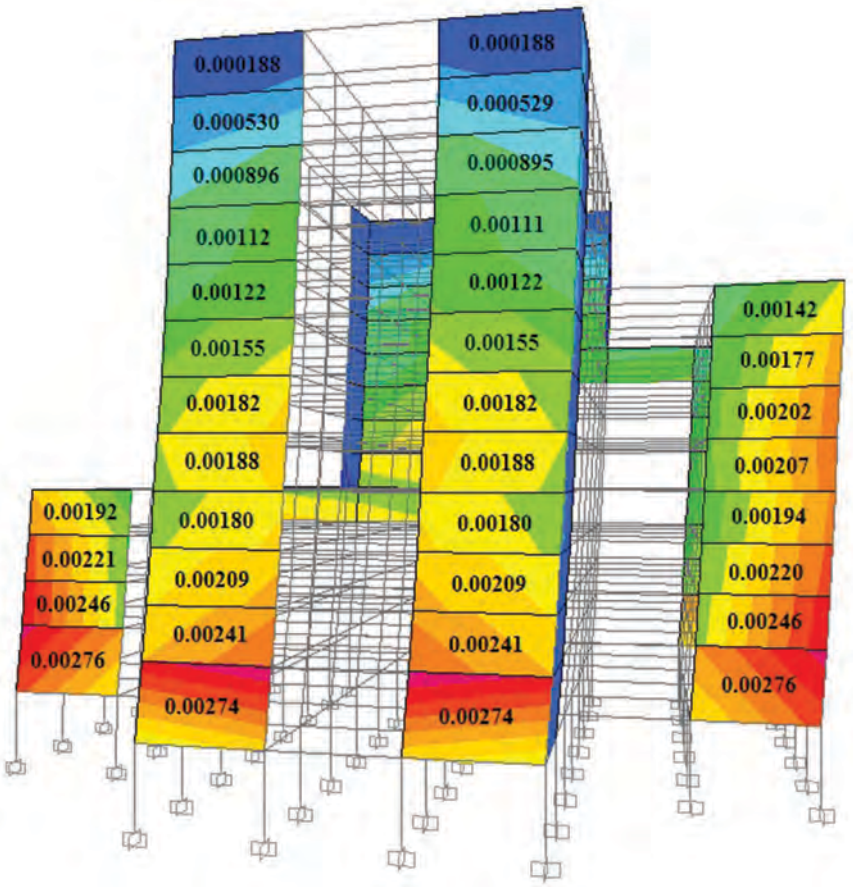

Fig. A.2. Computed DDIs on perimeter of building.

MRIs. There is approximately a 65% probability of exceeding DSI, given the 10-year maximum DDI of 0.00276. Figure A.3b shows the DS1 fragility curve for the glass curtain wall, along with a vertical line at the maximum DDI, computed using the 10-year MRI. The curve illustrates the fact that a DDI of 0.00276 is not an issue for the glass curtain wall because the probability of exceedance of DS1 is negligible.

The interior core masonry walls present a greater issue than the exterior curtain wall. Figure A.4 shows a cross-section of the model under the 10-year wind load with the

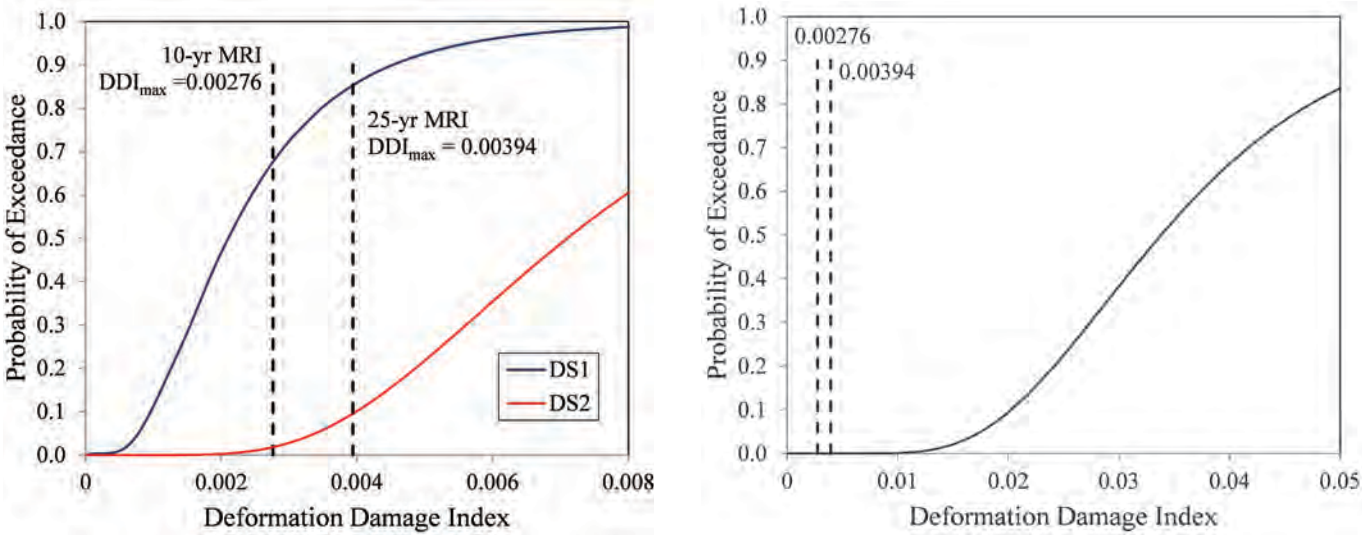

Fig. A.3. Decision spaces for exterior drywall and for exterior curtain wall: (a) drywall; (b) curtain wall for 10-year MRI.

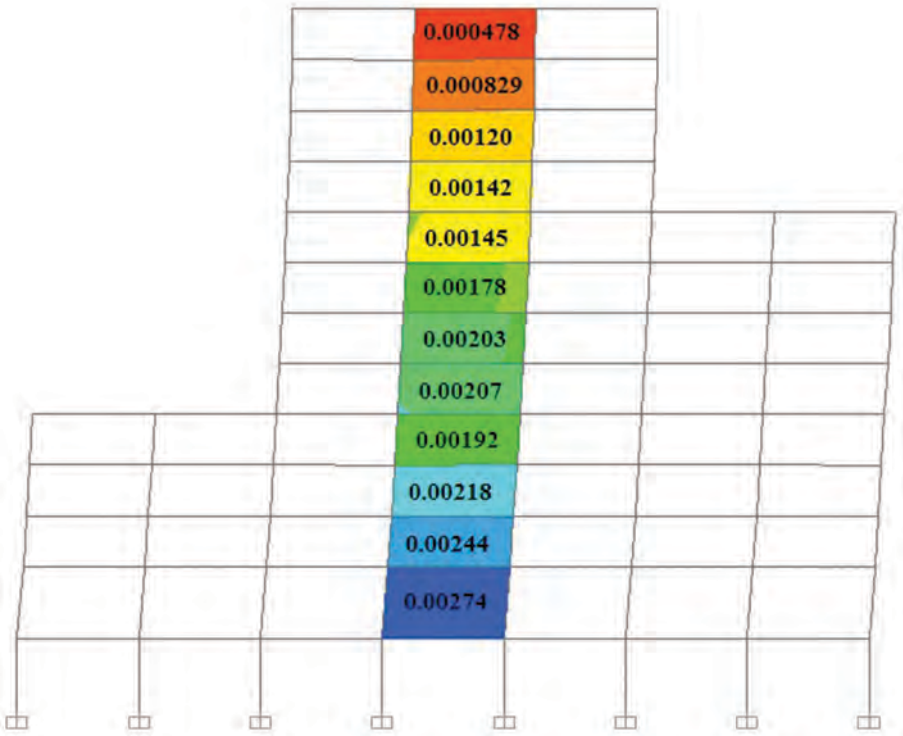

Fig. A.4. Computed 10-year DDIs in core of building.

DDIs for the interior core labeled. The maximum DDI of 0.00274 occurs at the first story, and the minimum of 0.000478 occurs at the top story. Figure A.5a shows two fragility curves for drywall. The minimum, mean, maximum and full range of computed DDI values are illustrated in the figure for the 10-year and 25-year wind loads. Figure A.5b shows the DS1 and DS2 fragility curves for ordinary masonry walls as well as the DDI ranges. The 25-year DDIs were calculated with Equation 1 for a wind speed of 89 mph. The hypothetical building owner has indicated that the average wall in the core (gypsum wallboard or masonry) should have no more than a 30% chance of minor damage (DS1) under the 10-year wind loads and no more than a 70% chance of minor damage under the 25-year wind loads. From Figures A.5a and b, the designer can see that the average DDI (0.00171) under the 10-year wind loads has a probability of exceedance for DS1 greater than 30%, thus failing the owner's requirement. However, the average DDI under the 25-year wind loads is approximately 60%, thus meeting the owner's requirement that it be less than 70%. The DDIs corresponding to other MRIs (such as 50- or 100-year) could also be determined with Equation 1 and incorporated into the decision-making process, provided that the owner has selected an allowable probability of damage corresponding to those MRIs.

A final issue to consider is torsional wind loading. It is prudent to examine the effects of torsional loads, although due to the nature of the lateral load-resisting system (perimeter moment frame) in this building, torsional loading requirements are not likely to control. For this building, torsion was examined according to the provisions of ASCE 7-10, which requires that 75% of the lateral wind load be applied in combination with a torsional moment corresponding to 15% eccentricity. Figure A.6 shows the structure under the 10-year torsional load specified in ASCE 7-10. From Figure A.6, it can be seen that the torsional loading case does not control; the calculated DDIs are lower for this case than for the case in which 100% of the load is applied at no eccentricity (see Figure A.2).

APPENDIX B

Fragility Curve Theory

There are many different methods used to develop fragility curves (FEMA, 2013a; Porter, Kennedy and Bachman, 2007). If the objective of the fragility curve is to obtain rational damage measures, the most useful method is experimental testing. A typical test might involve fixing the base of the component (e.g., a sheet of gypsum wallboard) and applying an in-plane load in order to induce a shear strain. In the ideal testing procedure, there will be no vertical racking and no rigid-body rotation; thus, the shear strain and the interstory drift ratio in the component will be equal. As the test progresses, the load is incrementally increased until a particular damage state is observed (e.g., screws popping out, cracking or crushing). The shear strain at which the damage state occurs is noted, and the test is repeated on a new specimen.

Table B.1 shows data obtained from tests performed on gypsum wall partitions (Miranda and Mosqueda, 2013). The data are collected from six different sources, dating between

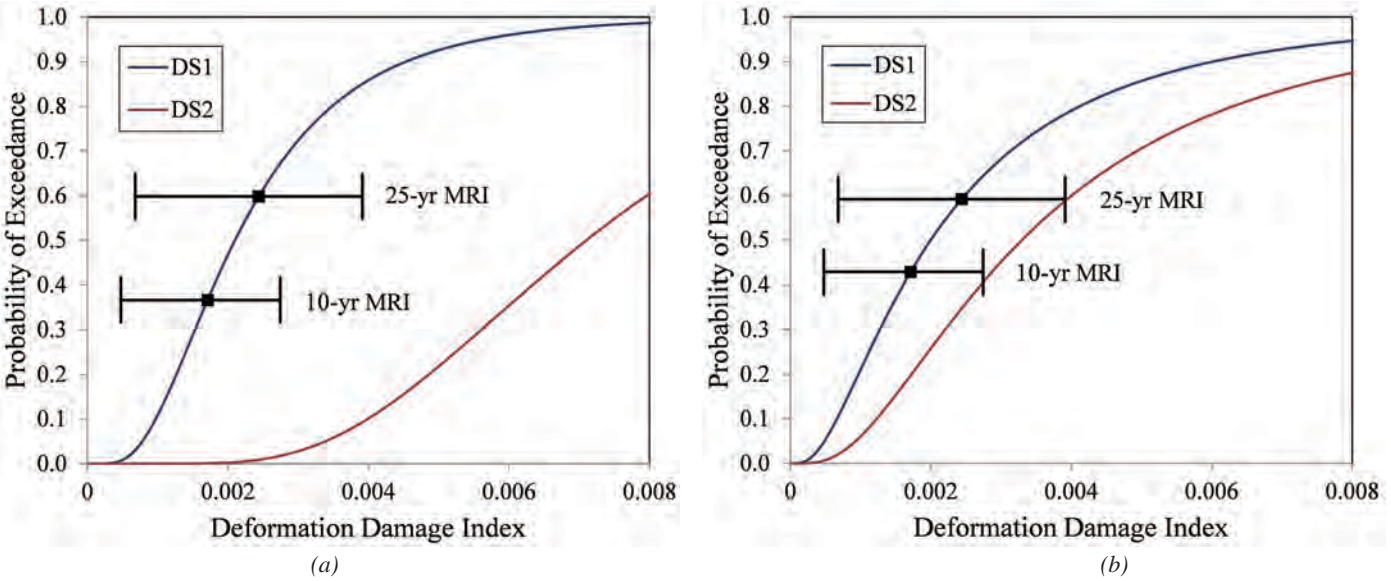

Fig. A.5. Decision spaces for interior drywall and for interior curtain wall: (a) drywall; (b) masonry wall.

Table B.1. Gypsum Partition Wall Data Set (Miranda and Mosqueda, 2013)							
Source	**DS1**	**Source**	**DS1**	**Source**	**DS1**	**Source**	**DS1**
JAB	0.0026	**NEESR**	0.0040	**Rihal**	0.0039	**AMB**	0.0030
	0.0026		0.0020		0.0039		0.0030
	0.0026		0.0040		0.0026		0.0005
	0.0052		0.0020		0.0046		0.0005
	0.0026		0.0040		0.0052		0.0030
	0.0052		0.0020		0.0046		0.0030
	0.0026		0.0020		0.0039		0.0050
	0.0026		0.0040		0.0033		0.0050
	0.0007		0.0040		0.0039		0.0010
	0.0026		0.0040		0.0039		0.0010
	0.0013		0.0040		0.0039		0.0010
	0.0026		0.0040	**Lang**	0.0025		0.0010
Japan	0.0020		0.0040		0.0028		0.0010
							0.0010

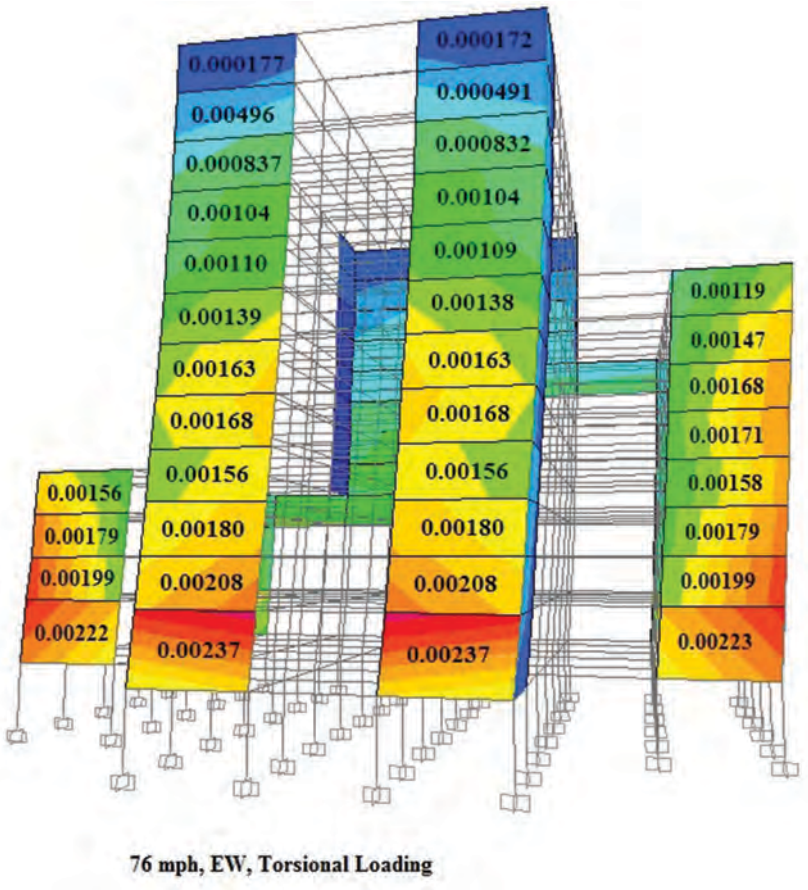

Figure A.6. Computed DDIs on perimeter of building for torsional loading.

Table B.2. Reduced Fragility Data			
(1) Data Point	(2) Sorted Value	(3) Ln(Sorted Value)	(4) Probability
1	0.0005	–7.6	0.0094
2	0.0005	–7.6	0.0283
3	0.0007	–7.264	0.0471
4	0.001	–6.908	0.066
5	0.001	–6.908	0.0948
…	…	…	…
51	0.0052	–5.259	0.9527
52	0.0052	–5.259	0.9716
53	0.0052	–5.259	0.9905
Mean	**0.00297**	**–5.950 = ξ**	—
Standard deviation	**0.00132**	**0.602 = λ**	—

1966 and 2010. The values represent the shear strain (in this case, equivalent to the interstory drift ratio due to the absence of vertical deformation) at which damage state 1 (minor damage such as cracking of drywall or warping of tape) was first observed.

The "raw" fragility data are plotted as solid symbols in Figure B.1. Such a plot is created by first sorting the fragility data in ascending order and then assigning a probability to each data point as follows:

$$p_i = \frac{i - 0.5}{M} \tag{B.1}$$

where M is the number of sample points and i is the rank of the sorted data point.

Table B.2 shows some of the data from Table B.1 that are used to plot the symbols in Figure B.1, where column (2) of the table provides the X-axis values, and column (4) of the table provides the Y-axis values.

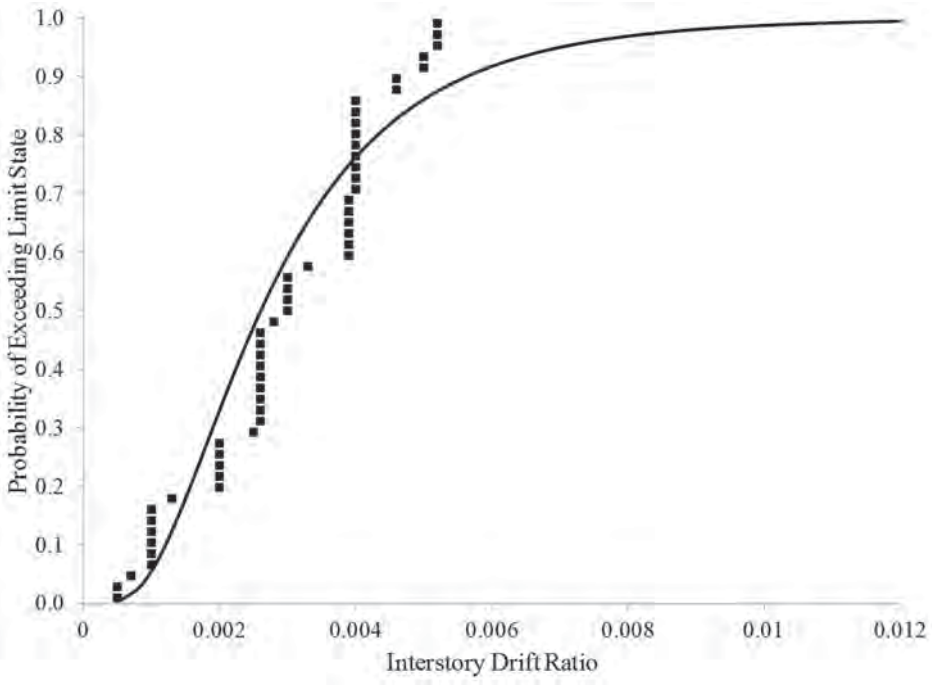

Fig. B.1. Fragility curve construction.

Table B.3. Fragility Information for Gypsum Drywall Building Elements (PACT)				
Building Element[1,2,3]	**Damage State**	**Mean Demand**	**λ**	**Dispersion (ξ)**
Fixed below, fixed above	DS1	0.0021	–6.166	0.60
	DS2	0.0071	–4.948	0.45
Fixed below, slip track above with returns	DS1	0.002	–6.215	0.70
	DS2	0.0050	–5.298	0.40
Fixed below, slip track above without returns	DS1	0.0035	–5.655	0.70
	DS2	0.0093	–4.678	0.45

Notes:
1. DS1 is screw pop-out, minor cracking of wallboard, warping or cracking of tape. DS2 corresponds to moderate cracking or crushing.
2. Full height wall with gypsum on metal studs.
3. These fragilities also apply to gypsum plus wallpaper, gypsum plus ceramic tile and high-end marble or wood panel, provided that the fixities (below and above) are equivalent. See PACT for more information.

Table B.4. Fragility Information for Exterior Enclosure Building Elements (PACT)				
Building Element	**Damage State**	**Mean Demand**	**λ**	**Dispersion (ξ)**
Glass curtain wall (monolithic)[1]	DS1	0.0338	–3.387	0.40
	DS2	0.0383	–3.262	0.40
Glass curtain wall (insulating glass units)[1]	DS1	0.021	–3.863	0.45
	DS2	0.024	–3.730	0.45
Generic storefront (monolithic)[2]	DS1	0.029	–3.540	0.50
	DS2	0.0473	–3.051	0.25
Generic storefront (insulating glass units)[2]	DS1	0.059	–2.830	0.25
	DS2	0.0665	–2.711	0.35

Notes:
1. Generic midrise stick-built curtain wall. Aspect ratio = 6:5. DS1 corresponds to glass cracking. DS2 corresponds to glass falling from frame. For fragility information relating to other glass types, aspect ratios and installation details, see PACT.
2. Aspect ratio 6:5. DS1 corresponds to a gasket seal failure. DS2 corresponds to glass cracking.

The mathematical fragility curve is simply the integral of a probability distribution function (PDF). In most cases, a lognormal PDF is used, as follows:

$$f_X(x) = \frac{1}{(x\zeta)\sqrt{2\pi}} \exp\left[-\frac{1}{2}\left(\frac{\ln x - \lambda}{\zeta}\right)^2\right] x \geq 0 \quad \text{(B.2)}$$

where λ is the mean of the natural log of the set (ln x) and ξ is the standard deviation of the natural log of the data set. For example, for the gypsum partition wall data shown in Table B.1, λ = –5.95 and ξ = 0.602. These values are computed as shown in column (3) of Table B.2.

The smooth mathematical fragility function is given by:

$$P(X \leq x) = \int_0^x f_X(x)\,dx \quad \text{(B.3)}$$

The fitted curve in Figure B.1 represents the mathematical fragility function given by Equation B.3.

Note that before using a curve developed from test data for design purposes, a goodness-of-fit test should also be performed (Porter et al., 2007). Additional caution should be exercised when using shear strains that correspond to sections of a fragility curve where there is little data resolution. To avoid this problem, it may be appropriate to select an MRI such that the corresponding shear strains from the fragility curve fall within a segment of the curve with a high resolution of tested data points.

Tables B.3 through B.6 contain λ values (mean of the natural log of the data), dispersion ξ values (standard deviation of the natural log of the data) and the descriptions of the associated damage states for a variety of nonstructural and structural components. The values in the tables were taken from the Performance Assessment Calculation Tool (FEMA, 2013b), which contains the same type of information for hundreds of structural and nonstructural components. PACT also contains useful data on the cost of repairing or replacing the building elements. When the cost data are combined with the probability of damage occurring,

Table B.5. Fragility Information for Concrete and Masonry Building Elements (PACT)				
Building Element	**Damage State**	**Mean Demand**	**λ**	**Dispersion (ξ)**
Reinforced concrete wall (low aspect ratio)[1]	DS1	0.0055	–5.203	0.36
	DS2	0.0109	–4.519	0.30
Low-rise reinforced concrete wall[2]	DS1	0.0076	–4.880	0.35
	DS2	0.0134	–4.313	0.45
Slender concrete wall[3]	DS1	0.0076	–4.880	0.35
	DS2	0.0134	–4.313	0.45
Ordinary reinforced masonry walls[4]	DS1	0.002	–6.215	0.86
	DS2	0.0033	–5.714	0.77
Special reinforced masonry walls[5]	DS1	0.0036	–5.627	0.59
	DS2	0.0059	–5.133	0.51

Notes:
1. DS1 corresponds to cracks of width between 0.04 and 0.12 in. DS2 represents crushed concrete core, localized concrete cracking (width > 0.12 in.) and buckling of vertical rebar.
2. Wall with return flanges. DS1 is crushed concrete core, localized concrete cracking (widths > 0.12 in.) and buckling of vertical rebar. DS2 is sliding of the wall resulting in distributed cracking.
3. DS1 corresponds to spalling of cover and vertical cracks. DS2 is exposed longitudinal reinforcing and buckling of vertical rebar. DS2 is sliding of the wall resulting in distributed cracking.
4. Partially grouted cells, shear dominated. DS1 is first occurrence of major diagonal cracks. DS2 is wide diagonal cracks in each direction, crushing or spalling at wall toes.
5. Fully grouted cells, shear dominated. DS1 is first occurrence of major diagonal cracks. DS2 is wide diagonal cracks in each direction, crushing or spalling at wall toes.

Table B.6. Fragility Information for Structural Steel Building Elements (PACT)				
Building Element	**Damage State**	**Mean Demand**	**λ**	**Dispersion (ξ)**
Braced frame (no seismic detailing)[1]	DS1	0.0042	–5.473	0.25
Ordinary steel concentric braced frame[2]	DS1	0.00159	–6.444	0.70
	DS2	0.010	–4.605	0.30
Special steel concentric braced frame[3]	DS1	0.0035	–5.655	0.46
	DS2	0.0058	–5.150	0.65

Notes:
1. Design for factored loads, no additional seismic detailing. DS1 corresponds to the fracture of brace or gusset plate, gusset buckling and significant decrease in lateral stiffness.
2. DS1 is minor damage, including some buckling of the brace and initial yielding of the gusset. DS2 is moderate damage, including additional brace buckling, gusset yielding and yielding of members.
3. WF braces, balanced design criteria. DS1 corresponds to initial brace buckling, yielding of the gusset and slight residual drift. DS2 is moderate damage, significant buckling of brace, initiation of yielding and out-of-plane deformation of the gusset, initiation of cracking of welds of gusset and yielding of members.

the engineer can estimate an expected repair cost over the time period in question. This aspect of the serviceability design is discussed later with regard to the potential adaptation and application of PACT to PBWE. More information on component testing and fragility development for specific components can be found in Miranda and Mosqueda (2013), Lee et al. (2006), O'Brien et al. (2012), and Algan (1982). Additionally, if the fragility parameters for a particular component cannot be found, fragility curves can be developed by the engineer, using the FEMA P-58 Appendix H procedures (FEMA, 2013a). If actual test data are available, the engineer should use the mean and dispersion (appropriately adjusted for testing procedures) to create a fragility curve. In the absence of test data, other procedures may be used, including Monte Carlo simulation, "expert opinion" and the "single calculation" procedure, which consists of determining a best estimate for the average capacity (Q) of the component and setting the mean value equal to $0.92Q$, with a dispersion equal to 0.40. This procedure can be applied when damage state means are known, but dispersions are unknown or difficult to quantify.

APPENDIX C

Creating Fragility Curves with Software Programs

Although the Performance Assessment Calculation Tool (PACT) can be used to create and view fragility curves, the engineer may wish to create and manipulate the curves with the use of commercial software such as Microsoft Excel, Mathcad, or some other program. Many software programs contain built-in functions capable of producing fragility curves through the use of lognormal distribution functions.

In Microsoft Excel (Microsoft Corporation, 2013) the fragility curve can be plotted using the **lognorm.dist** function. This function takes the following form: **lognorm.dist(*x*, mean, dispersion, cumulative)**, where x is the engineering demand parameter at which the probability of exceedance is to be evaluated, mean is λ, dispersion is ξ and cumulative is true or false (if true, the cumulative distribution function is returned; if false, the probability density function is returned). Referring to the 10-story example, it was determined that a DDI of 0.00153 represents a 30% probability of exceedance of DS1 (mean demand = 0.0021, dispersion = 0.6). This can be calculated using **lognorm.dist(0.00153, ln(0.0021), 0.6, TRUE) = 0.30**.

In Mathcad (Parametric Technology Corporation, 2007) the fragility curve is created with the **plnorm** function, of the form **plnorm(*x*, mean, dispersion),** where the required inputs are defined in the same manner as the Excel function.

ABBREVIATIONS

DDI	deformation damage index
DDZ	deformation damageable zone
DG	damage gage
DM	damage measure
DS	damage state
EDP	engineering demand parameter
IDI	interstory drift index
MRI	mean recurrence interval
PACT	performance Assessment Calculation Tool
PBEE	performance-based earthquake engineering
PBWE	performance-based wind engineering

Panel Zone Deformation Capacity as Affected by Weld Fracture at Column Kinking Location

DONG-WON KIM, COLIN BLANEY and CHIA-MING UANG

ABSTRACT

Three full-scale specimens were tested to evaluate the cyclic performance of rehabilitated pre-Northridge steel beam-to-column moment connections. A Kaiser bolted bracket (KBB) was used on the beam bottom flange for all specimens, but different rehabilitation schemes (another KBB, a notch-tough beam flange replacement weld, or a double-tee welded bracket) were used to strengthen the top flange. All specimens were able to sustain an interstory drift angle of 0.04 radian, with large inelastic deformations in the panel zone. Two specimens experienced fracture at the replacement complete-joint-penetration (CJP) welds, mainly due to the large shear deformation in the panel zone. Because it may not be economically feasible to mitigate weak panel zones in seismic rehabilitation, an analytical model was developed to predict the panel zone deformation capacity and the associated strength. In this model, it was postulated that the ultimate panel zone deformation capacity corresponded to that when each column flange was fully yielded and excessive kinking would cause fracture of the beam flange CJP welds. This postulation was verified by the test data of two specimens that experienced weld fracture due to excessive panel zone deformation. It was shown that the deformation capacity is a function of d_b/t_{cf} (beam depth-to-column flange thickness ratio). The effect of column axial load was also studied.

Keywords: special moment frame, moment connection, panel zone, shear deformation, Kaiser bolted bracket, rehabilitation.

INTRODUCTION

The Kaiser bolted bracket (KBB) moment connection is a proprietary connection prequalified by AISC 358-10 (AISC, 2010a) for applications in seismic regions. In a KBB moment connection, a cast high-strength steel bracket is fastened to each beam flange and bolted to the column flange; a pair of brackets is placed symmetrically on both the top and bottom flanges of the beam. The bracket attachment to the beam flange can be either welded (W-series brackets) or bolted (B-series brackets). Figure 1 shows one example of a bolted KBB connection, and Figure 2 shows one of the two bolted brackets prequalified by AISC. The prequalification is mainly based on full-scale tests (Kasai, Hogdon and Bleiman, 1998, Gross et al., 1999, Newell and Uang 2006); see Adan and Gibb (2009) for a summary of the development of this connection.

Note that AISC 358-10 is intended for new construction, not seismic rehabilitation. When bolted KBB connections are used, one major advantage is to eliminate field welding. This is desirable, especially for seismic rehabilitation of existing steel moment frame buildings. The bracket configuration is proportioned to develop the probable maximum moment strength of the connected beam. According to AISC 358-10, yielding and plastic hinge formation are intended to occur primarily in the beam at the end of the bracket away from the column face. Limited yielding in the column panel zone may occur, and the panel zone shear strength per AISC 341-10 (AISC, 2010b) needs to be satisfied. The beam size is limited to W33×130.

The KBB connections were recently proposed for the seismic rehabilitation of a pre-Northridge steel moment frame building (Blaney et al., 2010). Qualification tests were conducted for this project because of the following challenges. First, AISC 358-10 requires that the KBBs be symmetrically placed above and below the beam. For seismic rehabilitation, it is not architecturally desirable to place a KBB above the beam because it may extrude beyond the floor slab. It has been shown, however, that the bottom-only bracket configuration cannot prevent fracture of the beam top flange complete-joint-penetration (CJP) groove weld in a pre-Northridge moment connection (Gross et al., 1999). Second, the beam flanges are not welded to the column flange in the AISC prequalified KBB moment connections, while this is not the case for the rehabilitated moment connections. Such a difference may alter the force transfer mechanism in the connection. Third, both the beam size and the required KBB size (type B1.0C) exceed those permitted by AISC 358-10. Finally, because steel moment frames designed and

Dong-Won Kim, Research Assistant, Department of Structural Engineering, University of California, San Diego, La Jolla, CA. Email: dwk008@ucsd.edu

Colin Blaney, Executive Principal, ZFA Structural Engineers, San Francisco, CA, Email: colinb@zfa.com

Chia-Ming Uang, Professor, Department of Structural Engineering, University of California, San Diego, La Jolla, CA (corresponding author). Email: cmu@ucsd.edu

Paper No. 2013-17R

Table 1. Width-to-Thickness Ratios			
Member	**Size**	$b_f/2t_f$	h/t_w
Beam	W36×150	6.37	51.9
Column	W14×193	5.45	12.8
Note: $\lambda_{hd} = 0.30\sqrt{E/F_y} = 7.22$ for flange; $\lambda_{hd} = 2.45\sqrt{E/F_y} = 59$ for web ($P_u = 0$).			

constructed prior to the 1994 Northridge earthquake could have very weak panel zones, where the demand-capacity ratio for shear yielding in the panel zone is much higher than that of flexural hinging of the connected beams, and because it is not practical to rehabilitate existing moment connections to achieve the intended performance of AISC 358-10 (i.e., beam plastic hinging with limited or no panel zone yielding), full-scale testing was needed to verify the proposed connection rehabilitation scheme with a weak panel zone.

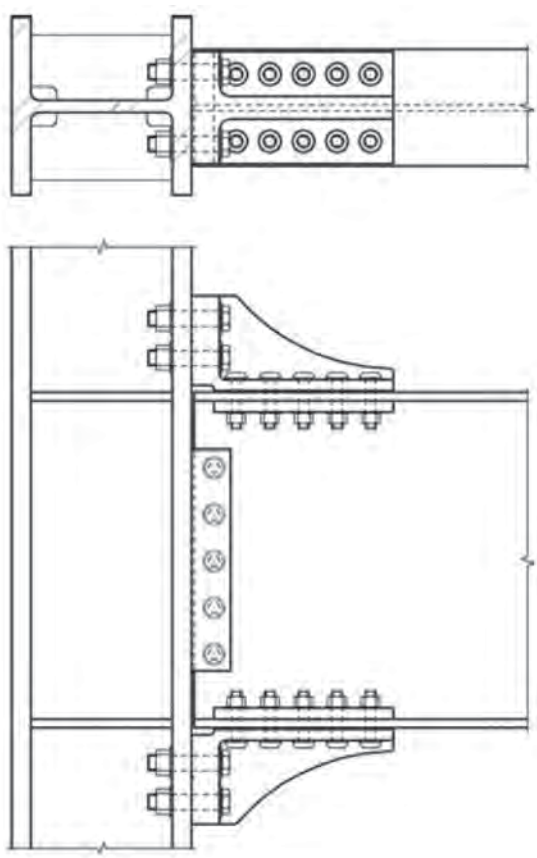

Fig. 1. KBB connection (figures reprinted from AISC, 2010a).

TEST PROGRAM

Test Specimens

A total of three nominally identical, full-scale pre-Northridge moment connections with a W36×150 beam and a W14×193 column were rehabilitated and tested. Table 1 shows that the beam and column sections satisfied the AISC 341-10 compactness requirement as highly ductile members. The pre-Northridge style, welded flange-bolted web moment connections were first fabricated and constructed following the pre-Northridge practice. Beam flange-to-column flange CJP groove welds were made with an E70T-4 electrode. Steel backing, runoff tabs, and weld dams were also used in a manner consistent with the pre-Northridge practice. Stiffeners inside the panel zone and one stiffener in the beam web were included to simulate an existing condition in the building.

For rehabilitation, runoff tabs and weld dams were removed while the steel backing remained. Then a B-series bracket (B.1.0C) was installed on the beam bottom flange of all three specimens. Table 2 summarizes the bracket details. To attach the bracket to the column and beam flanges, 1⁄16- and 1⁄32-in. oversized holes were made using a magnetic-base drill to the column and beam flanges, respectively. The high-strength bolts were fully tensioned with a calibrated hydraulic torque wrench. The treatment of the beam top flange was different for all three specimens, as described below.

For specimen 1, the same bracket was also added to strengthen the top flange (see Figure 3), a configuration required by AISC 358-10 for new construction. For

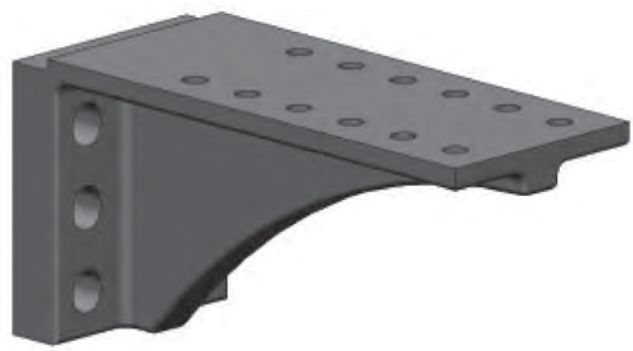

Fig. 2. KBB type B1.0 (figures reprinted from AISC, 2010a).

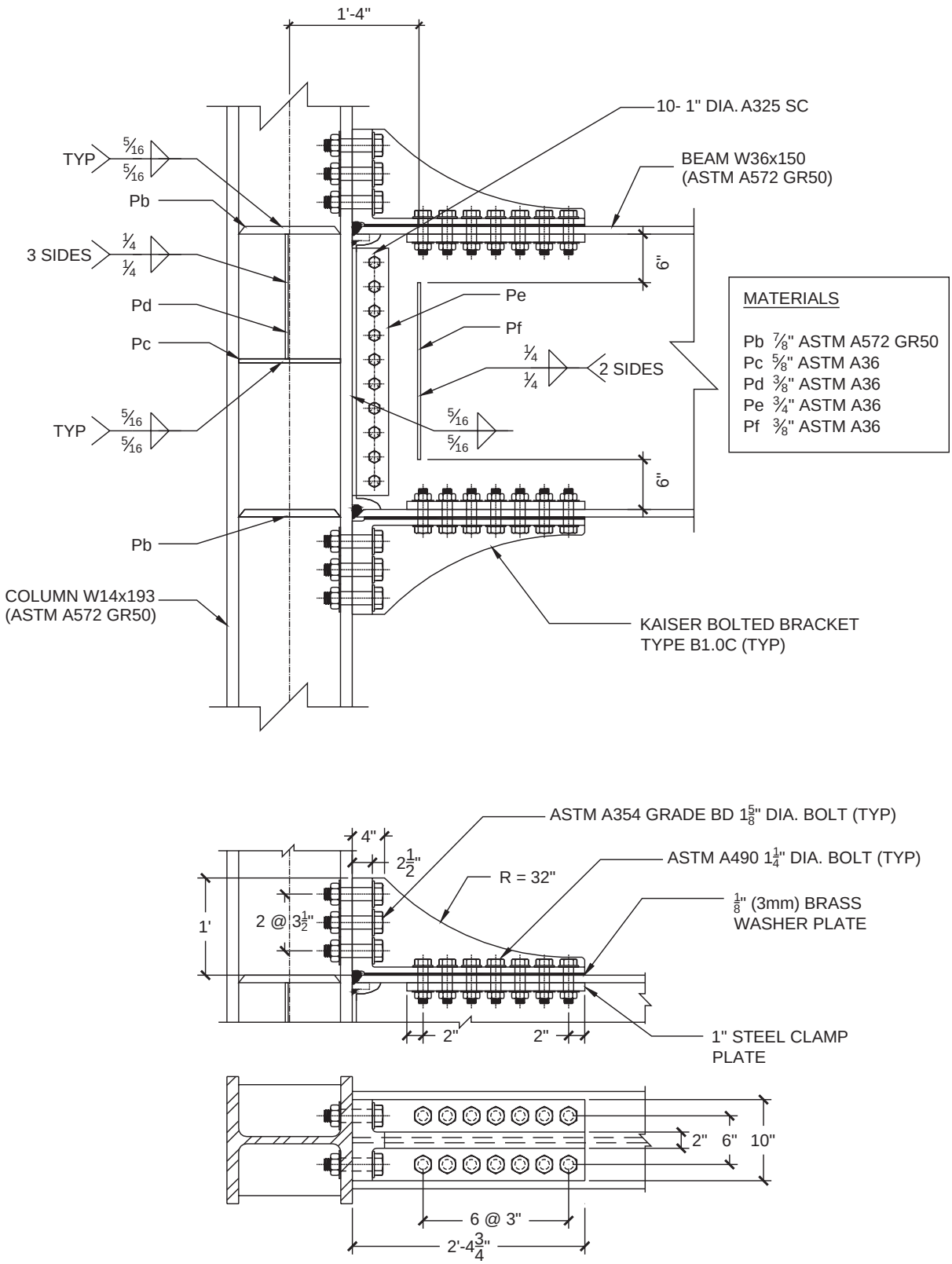

DETAILS OF KAISER BOLTED BRACKET (B1.0C)

Fig. 3. Specimen 1 connection details.

Table 2. Kaiser Bolted Bracket B1.0.C					
Proportions					
Bracket Length, L_{bb} (in.)	**Bracket Height, h_{bb} (in.)**	**Bracket Width, b_{bb} (in.)**	**Number of Column Bolts, n_{cb}**	**Column Bolt Gage, g, (in.)**	**Column Bolt Diameter (in.)**
28¾	12	10	6	6½	1⅝
Design Proportions					
Column Bolt Edge Distance, d_e (in.)	**Column Bolt Pitch, p_b (in.)**	**Bracket Stiffener Thickness, t_s (in.)**	**Bracket Stiffener Radius, r_v (in.)**	**Number of Beam Bolts, n_{bb}**	**Beam Bolt Diameter (in.)**
2	3½	2	32	14	1¼
See Figure 9.5 in AISC 358 for bracket parameter definition.					

Table 3. Steel Member Sizes and Mechanical Properties of Specimens 1, 2 and 3			
Member	**Yield Stress (ksi)**	**Tensile Strength (ksi)**	**Elongation* (%)**
Beam flange (W36×150)	61.6	75.9	33
Column flange (W14×193)	62.1	80.5	31.5
*Elongation is based on a 2-in. gage length.			

specimen 2, the existing beam top flange weld was gouged out and then replaced by a notch-tough CJP weld made with an E71T-8 electrode; the minimum required Charpy V-Notch impact test values were 20 ft-lb at 20 ºF and 40 ft-lb at 70 ºF. The steel backing remained but was reinforced with a 5⁄16-in. fillet weld. The existing weld access hole was not modified.

After testing of specimen 2, it was decided to not only replace the existing beam top flange CJP weld as in specimen 2 (see Figure 4), but to also strengthen the new weld with a welded double-tee bracket for specimen 3 (see Figure 5). The height of the welded bracket (5 in.) was selected to be flush with the surface of the existing concrete slab. The cross-section of the double-tee bracket was selected such that the beam top-flange stress at the column face was about 50% of the yield stress; the top-flange stress was calculated based on the elastic beam theory and a beam moment extrapolated from the probable maximum moment (M_{pr}) defined in AISC 358-10.

As noted earlier, the beam flanges were not connected to the column in the AISC 358-10 prequalified KBB connections. But CJP welds did exist in the rehabilitated moment connections. The bolted KBB brackets used had a notch to clear the existing CJP weld in the top flange and steel backing in the bottom flange.

Material Properties

ASTM A572 Grade 50 steel was specified for the beams, columns, continuity plates and the double-tee bracket. A36 steel was specified for all other plates. Table 3 shows the mechanical properties of the materials obtained from tensile coupon tests. The material for the KBB high-strength castings was ASTM A958 Grade SC8620, class 90/60. This material has a specified minimum yield and tensile strengths of 60 and 90 ksi, respectively. ASTM A354 Grade BD 1⅝-in.-diameter, high-strength bolts were specified for the KBB-to-column fasteners, and ASTM A490 1¼-in.-diameter, high-strength bolts were specified for the KBB-to-beam fasteners.

Design Parameters

Based on AISC 341-10 and AISC 358-10, the design parameters (column-beam moment ratio and panel zone demand-capacity ratio) were calculated as provided in Table 4. Based on both nominal yield stresses (F_y) and actual yield stresses from the tensile coupon test results, the design parameters were computed for both the existing and rehabilitated conditions. To compute the column-beam moment ratio, the beam moment (M^*_{pb}) was determined by extrapolating the expected beam plastic moment to the centerline of the column, and the column moment strength (M^*_{pc}) was calculated by extrapolating the nominal flexural strength (including haunches where used) above and below the joint to the centerline of the beam. The column-beam moment ratios, $\sum M^*_{pc} / \sum M^*_{pb}$, were greater than 1.0 in all cases, indicating a strong-column weak-beam (SC/WB) configuration. The same table also shows that the panel zone demand-capacity ratios (V_{pz}/V_n) were much larger than 1.0 for all cases, implying very weak panel zones in these rehabilitated specimens.

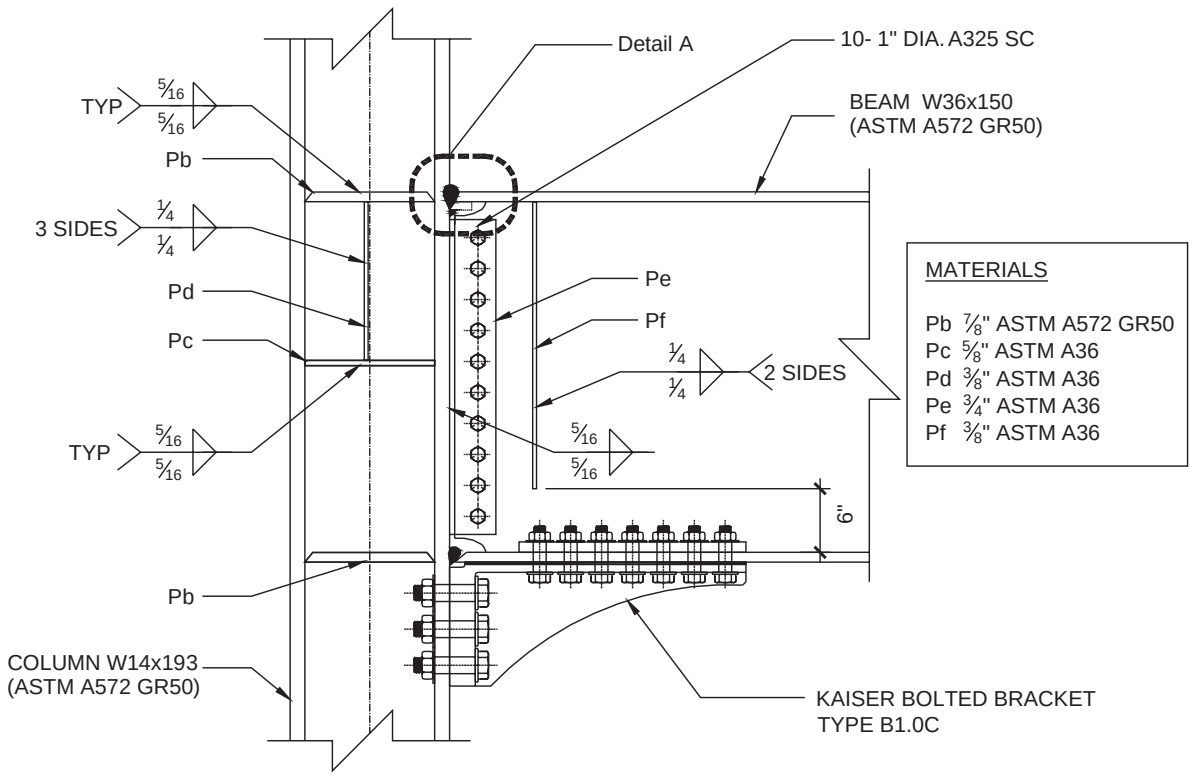

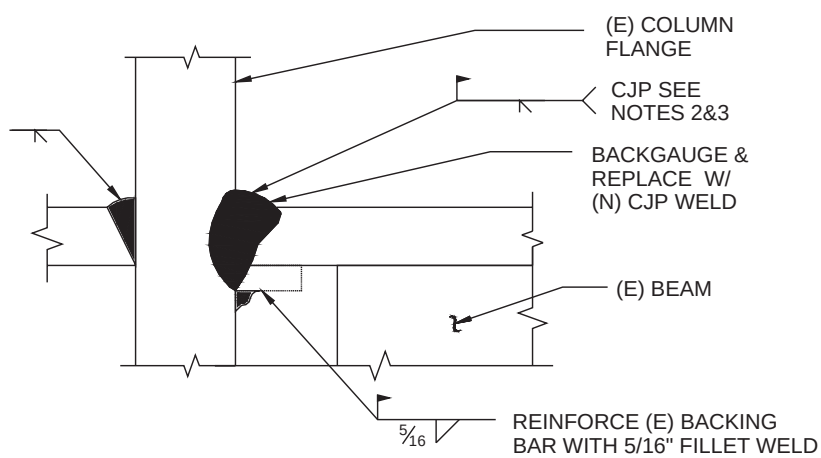

Detail A

NOTES:

1. PREPARE ORIGINAL TOP FLANGE WELD TO PRE-NORTHRIDGE CONDITION W/ CJP GROOVE WELD
2. GOUGE OUT (E) TOP FLANGE WELD & PREPARE JOINT FOR NEW WELD
3. PROVIDE (N) COMPLETE PENETRATION GROOVE WELD. (POST-NORTHRIDGE)

Fig. 4. Specimen 2 connection details.

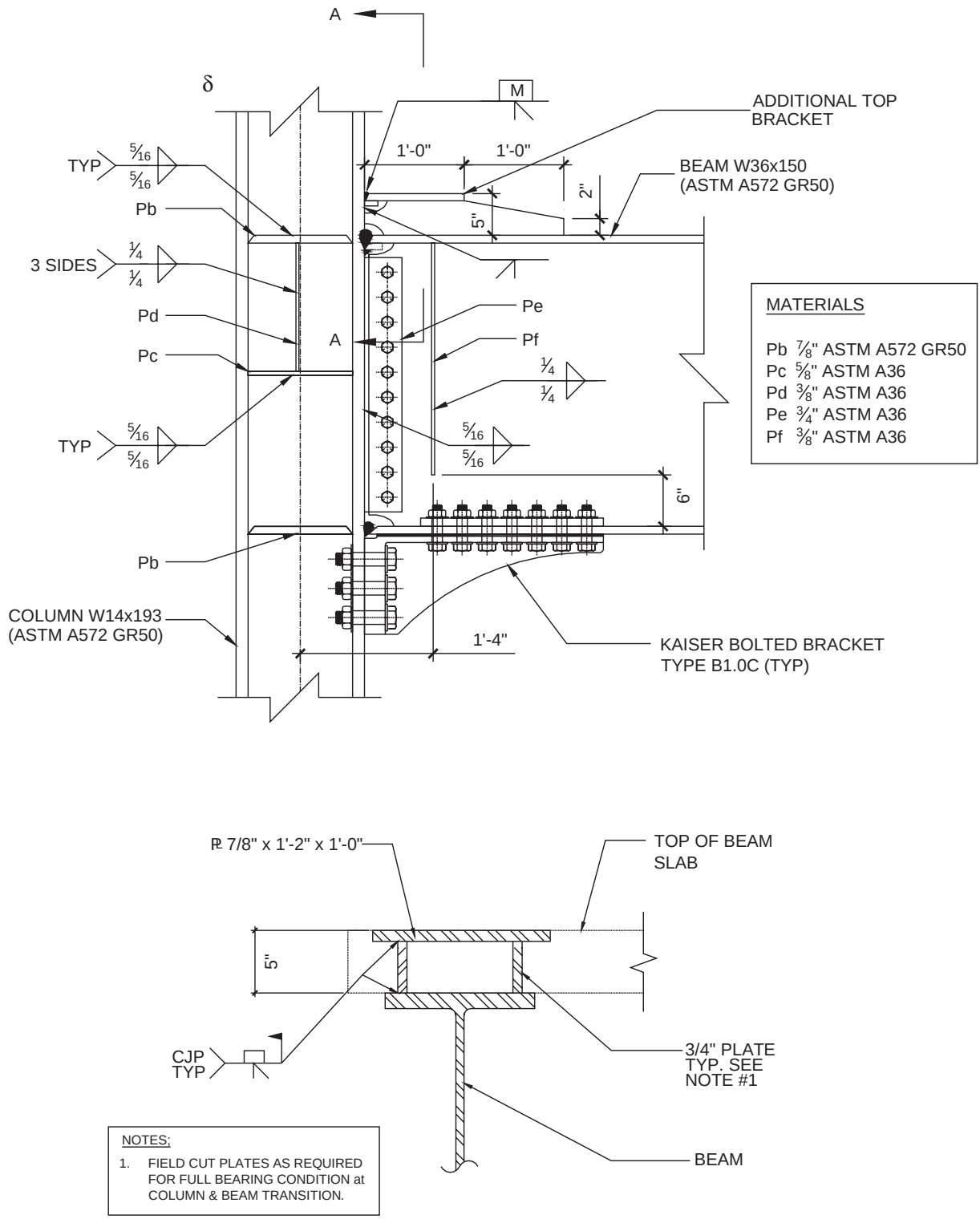

SECTION A - A

Fig. 5. Specimen 3 connection details.

Table 4. Column-Beam Moment Ratio and Panel Zone Demand-Capacity Ratio					
Specimen No.	Design Parameters	Before Rehabilitation		After Rehabilitation	
		Nominal F_y	Actual F_y	Nominal F_y	Actual F_y
Specimen 1	$\sum M_{pc}^* / \sum M_{pb}^*$	1.03	1.14	1.15	1.27
	V_{pz}/V_n	1.96	1.76	1.47	1.33
Specimen 2	$\sum M_{pc}^* / \sum M_{pb}^*$	1.03	1.14	1.05	1.16
	V_{pz}/V_n	1.96	1.76	1.75	1.58
Specimen 3	$\sum M_{pc}^* / \sum M_{pb}^*$	1.03	1.14	1.09	1.20
	V_{pz}/V_n	1.96	1.76	1.53	1.38

Test Setup and Loading Sequence

Figure 6 shows the test setup. A corbel was bolted to the end of the beam and attached to two 220-kip hydraulic actuators.

With some minor modification, the loading sequence specified in Section K2 of AISC 341-10 for beam-to-column moment connection test was used. A performance-based seismic rehabilitation study established a target story drift ratio of 3.5% (Liu et al., 2009). Therefore, the AISC loading protocol was modified to include two additional cycles at 3.5% story drift. The loading began with six cycles each at 0.375, 0.5, and 0.75% drift. The next four cycles in the loading sequence were at 1% drift, followed by two cycles each at 1.5, 2, 3, 3.5, and 4%. Beyond that, the specimens were cycled to 4.5% until failure due to the limitation of the actuator stroke. Testing was conducted in a displacement-controlled mode, and the cyclic displacement was applied at the end of the beam.

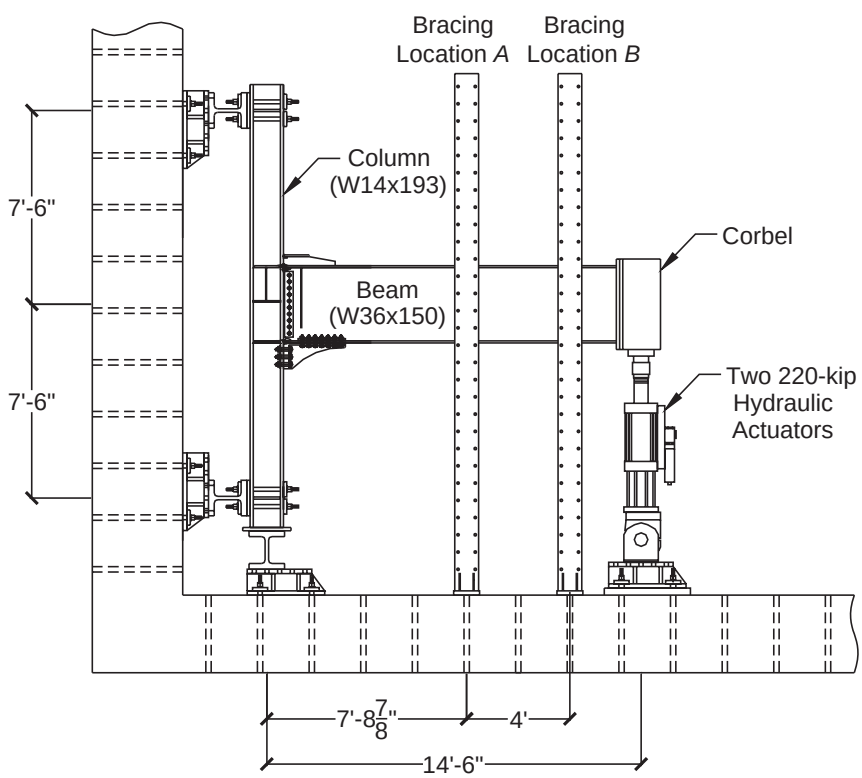

Fig. 6. Test setup (specimen 3).

TEST RESULTS

Figure 7 summarizes the damage pattern in three test specimens. The cyclic responses are presented in Figure 8. Significant shear yielding in the panel zone was observed in all three specimens. Also, the KBBs remained intact and showed no sign of yielding or damage. For specimen 1, the double KBBs forced beam plastic hinging in the form of flange and web local buckling as well as lateral-torsional buckling near the tip of the KBBs. The testing was stopped after completing two cycles at 4.5% story drift due to significant lateral-torsional buckling of the beam. Note that one lateral brace was provided at location *A* in specimen 1 (see Figure 6). This corresponded to an unbraced length of 92.9 in., which was less than that (123.2 in.) permitted by AISC 341-10. Because significant lateral-torsional buckling

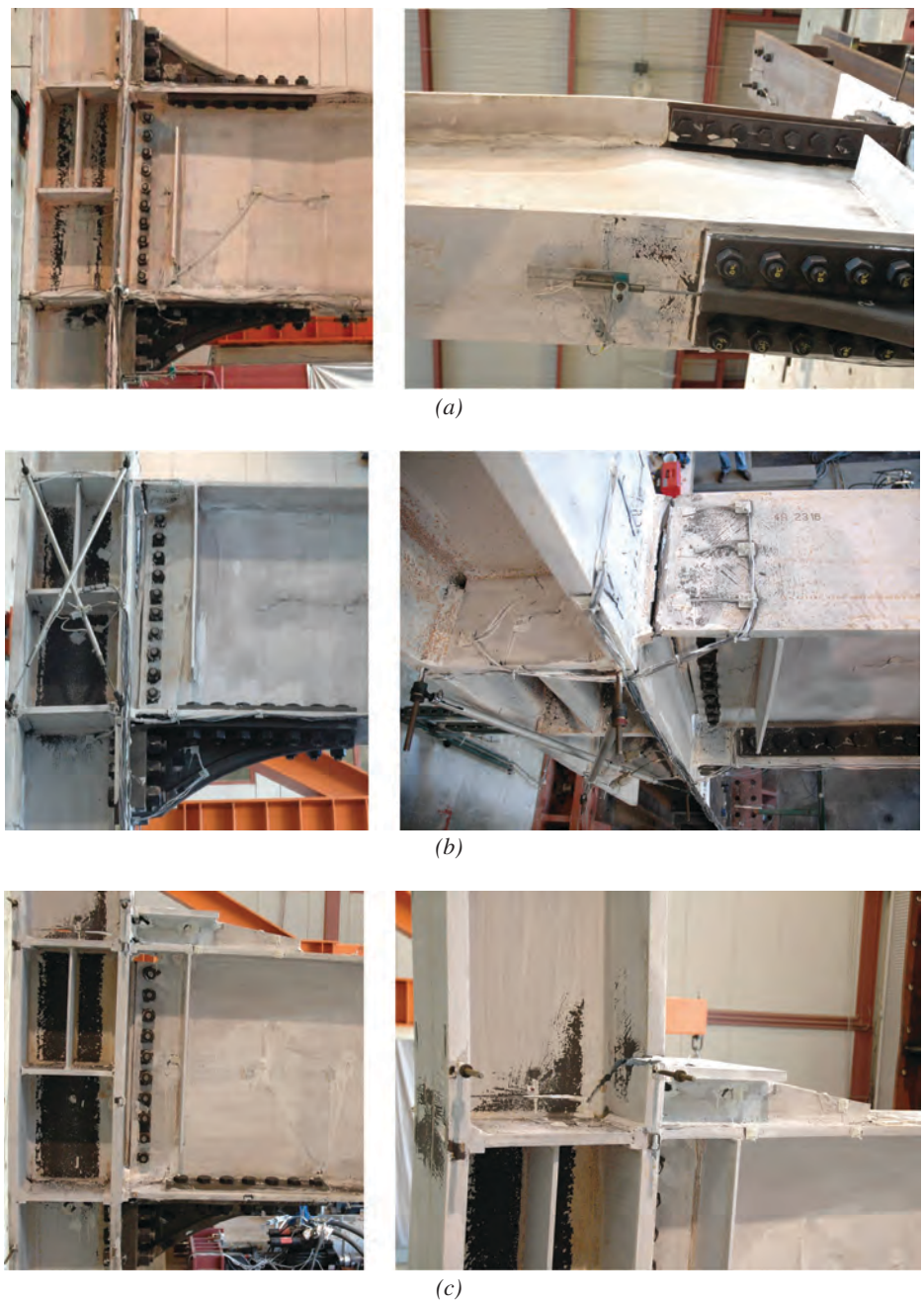

Fig. 7. Damage patterns: (a) specimen 1 panel zone yielding and beam lateral buckling; (b) specimen 2 panel zone yielding and top flange weld fracture; (c) specimen 3 panel zone yielding and top flange bracket weld fracture.

of the beam occurred in specimen 1, it was decided to add another lateral bracing at location *B* for specimens 2 and 3. The additional bracing was used to brace the top flange only to simulate the restraint provided by the concrete slab in the real building.

Specimen 2 experienced significant yielding in the panel zone, but the extent of beam plastic hinging was very limited with no sign of buckling. After completing one cycle at 4% story drift, fracture of the beam top flange at the replacement weld occurred during the second cycle (see Figure 7b).

The behavior of specimen 3 was similar to that of specimen 2—that is, inelastic action occurred mainly in the panel zone. The CJP weld connecting the horizontal plate of the double-tee bracket to the column flange started to fracture at 4% story drift. The specimen was then cycled at 4.5% story drift repeatedly until failure; see Figure 8c for the cyclic response. Brittle fracture occurred during the fifth negative cycle (see Figure 7c).

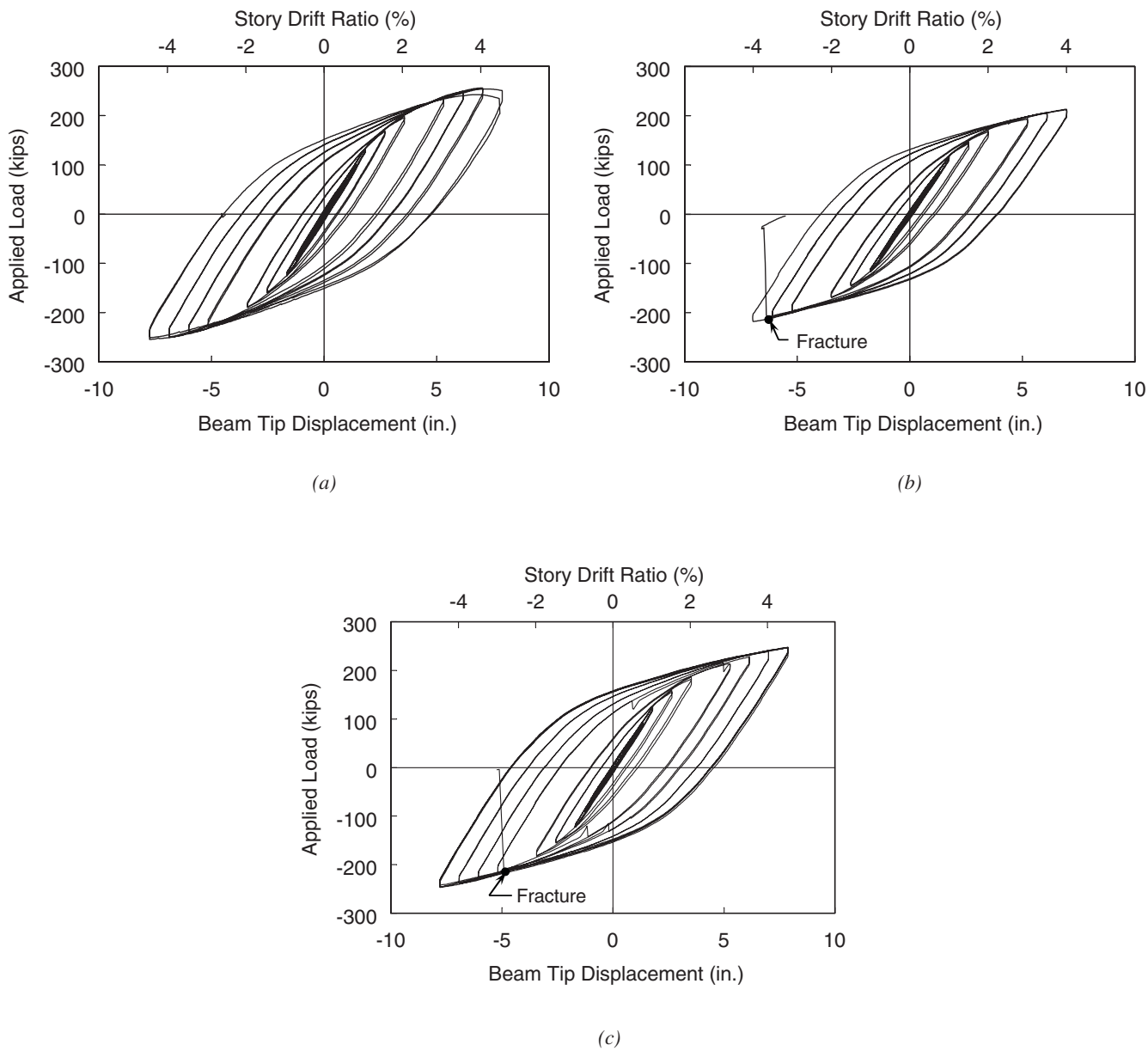

Fig. 8. Load versus beam tip displacement: (a) specimen 1; (b) specimen 2; (c) specimen 3.

PANEL ZONE BEHAVIOR

Effective Depth of Extended Panel Zone

With the addition of KBBs above and below the beam, the panel zone is extended in depth. AISC 358-10 (AISC, 2010a) defines the effective depth, d_{eff}, of the extended panel zone as the centroidal distance between column bolt groups in the upper and lower KBBs (see Figure 9a). Generalizing the AISC definition to specimens 2 and 3 with only one KBB used, the definition of d_{eff} is also shown in the figure.

The average shear deformations of the original and extended panel zones can be computed from test data based on Equations 1 and 2:

$$\gamma_{pz} = \frac{\sqrt{a^2 + d^2}}{2ad}\left(\delta_1 + \delta_2\right) \quad (1)$$

$$\gamma_{epz} = \frac{\sqrt{a^2 + \left(d_{eff}\right)^2}}{2ad_{eff}}\left(\delta_3 + \delta_4\right) \quad (2)$$

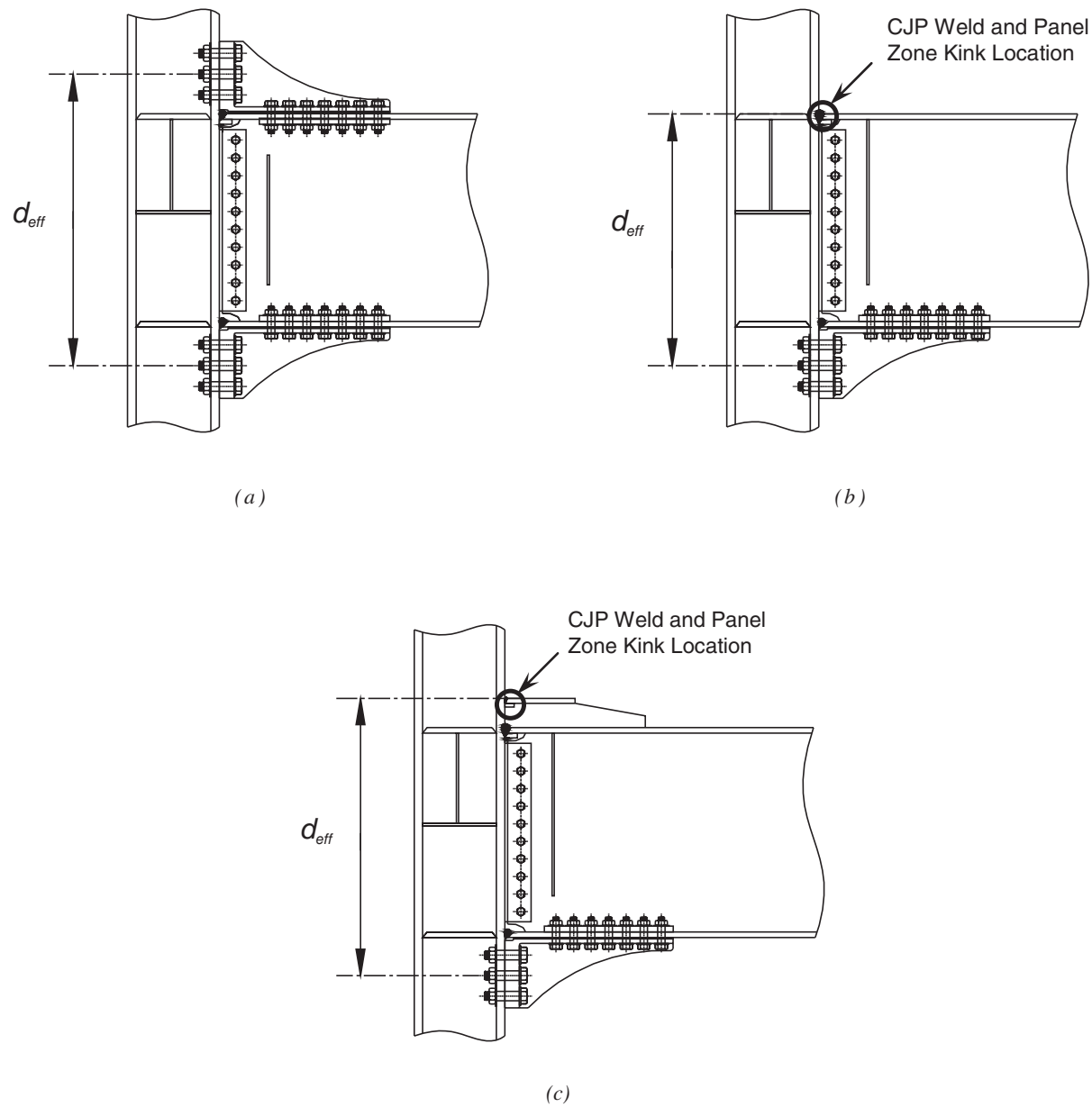

(a) *(b)* *(c)*

Fig. 9. Effective depth of extended panel zone: (a) specimen 1; (b) specimen 2; (c) specimen 3.

where the instrumentation for the panel zone deformations is shown in Figure 10. Figure 11 compares the shear deformations of the panel zones for all test specimens. It shows that the shear deformation was mainly concentrated in the original panel zone.

Based on a pair of diagonal measurements in the extended panel zone, the average shear deformation can be computed. The shear in the extended panel zone can also be computed by using the effective depth:

$$V = \frac{M_f}{0.95d_{eff}} - V_c \tag{3}$$

where M_f is the moment at the face of column and V_c is the shear in the column. The cyclic responses of the extended panel zones for specimens 2 and 3 are presented in Figure 12.

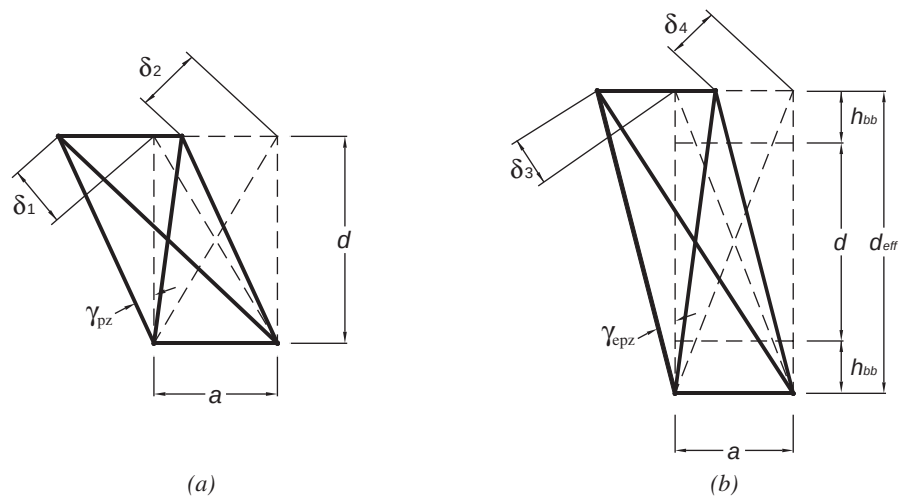

Fig. 10. Panel zone deformation measurements: (a) original panel zone before rehabilitation; (b) extended panel zone after rehabilitation (specimen 1).

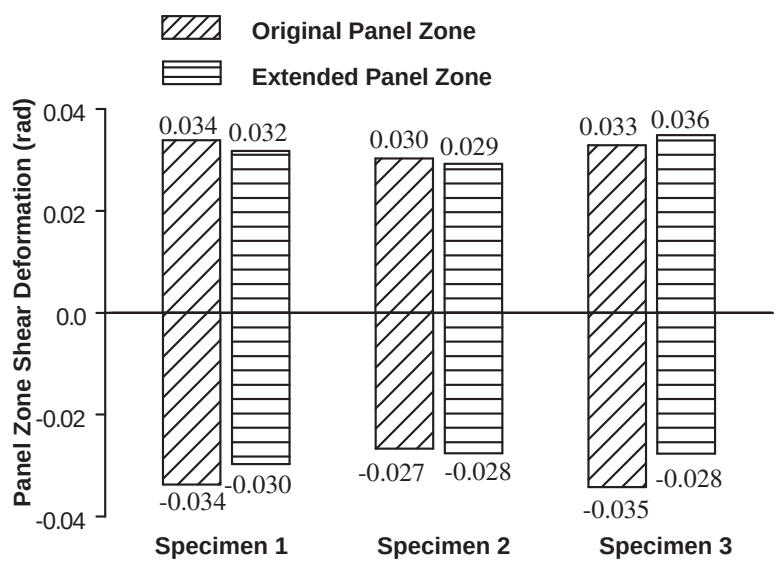

Fig. 11. Comparison of panel zone shear deformation.

Column-Flange Kinking and CJP Weld Fracture

Large panel zone deformation caused the column flange to kink at four corners of the panel zone. Figure 13 shows localized yielding of the flange on the backside of the column. On the front side, the location of the rehabilitated notch-tough CJP welded joint also coincided with one panel zone kinking location in specimens 2 and 3 (see Figure 9). Although these connections performed adequately to satisfy AISC 341-10 for special moment frames, repeated loading eventually caused fracture of the notch-tough CJP welds at the kinking locations. The relationship between CJP weld fracture and panel zone deformation is presented next.

WELD FRACTURE AND PANEL ZONE DEFORMATION CAPACITY

The panel zone behavior was extensively researched (e.g., Krawinkler, Bertero and Popov, 1971; Krawinkler, 1978; Kato, Chen and Nakao, 1988; Schneider and Amidi, 1998; El-Tawil et al., 1999; Lee et al., 2005). As will be shown, past research was mainly focused on the strength, not deformation capacity, of the panel zone, and the nominal shear strength of the panel zone in AISC 360 corresponds to a deformation at four times the yield shear strain. In this section, the relationship between CJP weld fracture and panel zone deformation is studied. Also, in performance-based

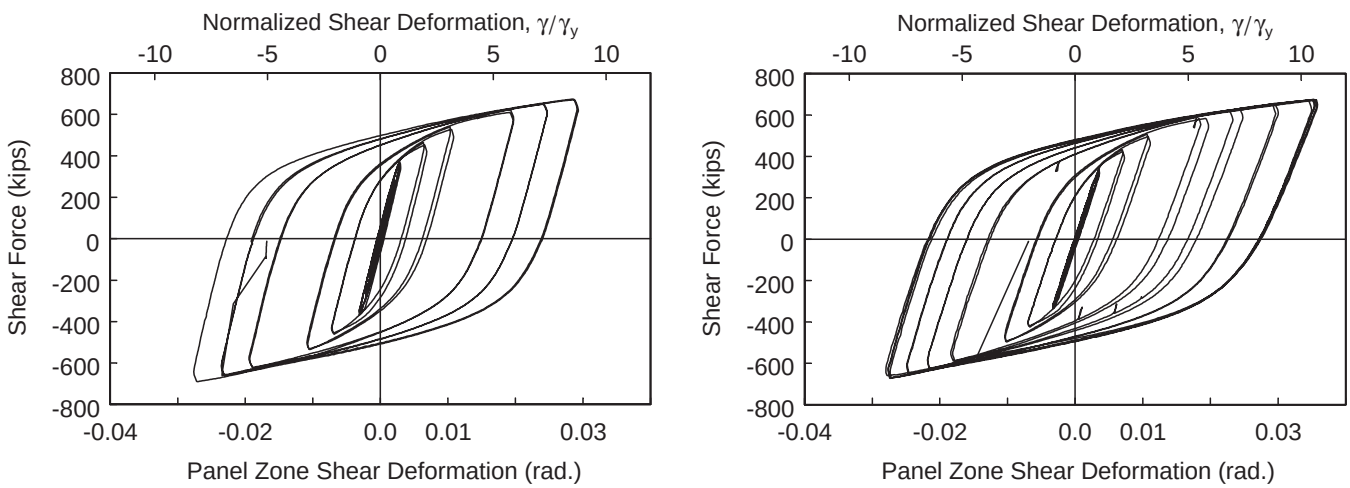

Fig. 12. Cyclic response of extended panel zone: (a) specimen 2; (b) specimen 3.

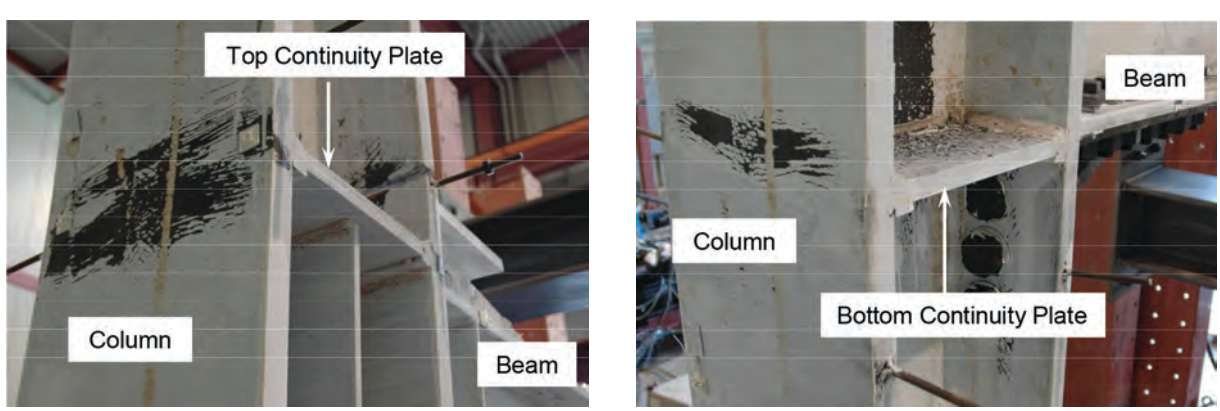

Fig. 13. Yielding pattern at column back side (specimen 3): (a) at top continuity plate level; (b) at bottom continuity plate level.

seismic analysis and design of tall buildings, PEER/ATC 72-1 (PEERC/ATC, 2010) suggested that a panel zone deformation capacity of 0.08 radian be used when panel zone shear distortion does not contribute to the incident of fractures at the beam-to-column connection. This deformation capacity is consistent with that accepted for link elements in eccentrically braced frames in AISC 341-10 (AISC, 2010b). Otherwise, a deformation capacity of 0.02 radian should be used when column-flange kinking would cause weld fracture at the beam-column connection. But no guidance is provided to determine when column-flange kinking is detrimental to weld fracture.

Krawinkler Model

Figure 14 shows the moment and shear diagrams of a column produced by seismic loading. The panel zone is in high shear with a reverse curvature (see Figure 15a). In the panel zone, the column web (together with doubler plates, if used) panel zone is bounded by two column flanges. Krawinkler (1978) used the superposition of column web and column flange in modeling the panel zone behavior. The column web was subjected to shear (see Figure 16a), where the web area was assumed to be $0.95d_c t_{cw}$, with d_c equal to the column depth and t_{cw} equal to the panel zone thickness and where the shear yield stress, τ_y, was $F_y/\sqrt{3}$ (equal to $0.577F_y$). The panel zone depth was also assumed to be $0.95d_b$, where d_b is the beam depth. A conservative assumption was made by ignoring strain hardening after yielding.

Although the bounding column flanges deform in reverse curvature, Krawinkler modeled theses flanges as rigid members and, instead, used rotational springs at four corners (i.e., kinking locations) of the panel zone to model the contribution from column flanges (see Figure 15b). It was assumed that column flanges contributed to both the stiffness and strength of the panel zone only when $\gamma \geq \gamma_y$, where $\gamma_y = \tau_y/G$ and G is the shear modulus. That is, the contribution from column flanges was ignored when $\gamma < \gamma_y$. Based on finite element analysis, Krawinkler et al. (1971) proposed the following rotational stiffness, K_s, at each corner:

$$K_s = \frac{M}{\theta} = \frac{Eb_{cf}t_{cf}^2}{10} \tag{4}$$

where b_{cf} is the column-flange width and t_{cf} is the column-flange thickness. Considering four rotational springs and the work equation $0.95d_b(\Delta V)(\Delta\gamma) = 4M\theta$) with $\theta = \Delta\gamma$, the proposed post-elastic stiffness, K_p, of the joint due to the column flanges (see Figure 16) was

$$K_p = \frac{\Delta V}{\Delta\gamma} = \frac{1.095b_{cf}t_{cf}^2 G}{d_b} \tag{5}$$

Furthermore, the panel zone shear strength was defined at $4\gamma_y$. From the superposition shown in Figure 16, the following panel zone shear strength at $4\gamma_y$ was developed by Krawinkler (1978):

$$V_{pz}^K = 0.55F_y d_c t_{cw}\left(1+\frac{3.45b_{cf}t_{cf}^2}{d_b d_c t_{cw}}\right) \tag{6}$$

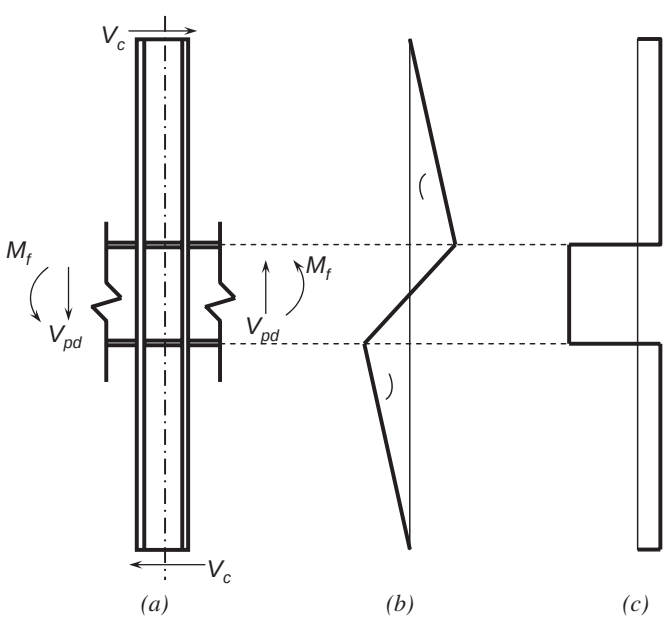

Fig. 14. Forces on column: (a) column free-body diagram; (b) moment diagram; (c) shear diagram.

AISC Design Strength

The AISC *Specification* (AISC, 2010c) uses $0.6F_y$ instead of $0.577F_y$ as τ_y. Furthermore, the web shear area is taken as $d_c t_{cw}$ instead of $0.95d_c t_{cw}$. The slightly modified form of Equation 6 is used in the AISC *Specification*:

$$V_{pz}^{AISC} = 0.6F_y d_c t_{cw}\left(1+\frac{3b_{cf}t_{cf}^2}{d_b d_c t_{cw}}\right) \tag{7}$$

Alternate Panel Zone Model

It was shown in Figure 12 that a panel zone could deform to a deformation level much higher than $4\gamma_y$. But excessive deformation could cause fracture in the beam flange-to-column flange CJP weld. In this paper, an alternate model is presented to compute the ultimate deformation capacity and the associated strength of the panel zone. This deformation capacity uses the fracture of a notch-tough CJP weld at the column kinking location as the limit state. As will be

shown, the deformation capacity can be significantly higher than the $4\gamma_y$ value assumed in AISC 360-10. This model also shows that a panel zone's deformation can be less than $4\gamma_y$ in some situations.

The panel zone behavior is again established by superimposing the responses of the column web and flanges (see Figure 17). The web area is taken as $0.95d_c t_{cw}$. Therefore, the shear yield strength of the column web is

$$V_{cw,y} = 0.6F_y\left(0.95d_c t_{cw}\right) \tag{8}$$

With $\gamma_y = 0.6F_y/G$, the elastic shear stiffness of the column web is

$$K_{cw} = \frac{V_{cw,y}}{\gamma_y} = 0.95d_c t_{cw} G \tag{9}$$

The Krawinkler's model ignores strain hardening after yielding. But, because strain hardening generally exists for the steel grades ($F_y \leq 50$ ksi) permitted in AISC 341-10, a strain hardening ratio of 0.03 is adopted as shown in Figure 17a. The strain hardening ratio of 0.03 is based on monotonic torsional coupon test results conducted by Slutter (1981).

Because each column flange in the panel zone region would bend about its weak axis in reverse curvature (see Figure 15a), the model in Figure 18a is used to consider the contribution from column flanges. It is idealized that each column flange will deform elastically until the plastic moment of the column flange is reached:

$$M_{p,cf} = \left(\frac{b_{cf} t_{cf}^{\,2}}{4}\right) F_{yc} \tag{10}$$

where F_{yc} is the column-flange yield stress. The associated deformation, which is the chord angle in Figure 18b, corresponds to γ_{pz} in Figure 17. It is postulated that γ_{pz} can be defined as the plastic deformation capacity of the panel zone beyond which the notch-tough CJP weld at the kinking locations is prone to fracture. This postulation is to be verified by test data in the following.

Consider one fix-ended column-flange flexural member with a span of $0.95d_b$ and a depth of t_{cf}. The shearing effect

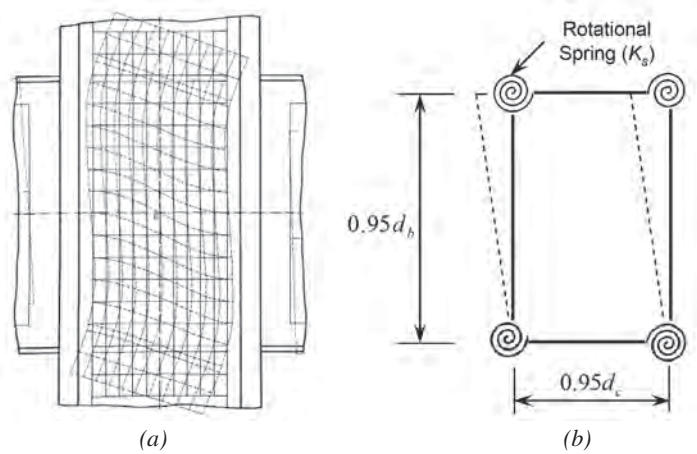

Fig. 15. Krawinkler's model of panel zone: (a) panel zone deformed shape; (b) mathematical model (figures reprinted from Krawinkler, 1978).

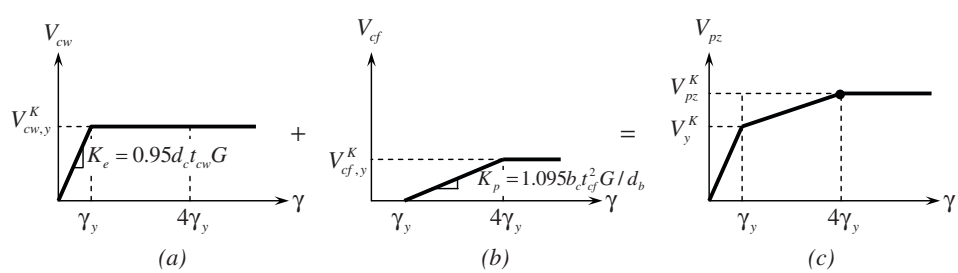

Fig. 16. Superposition of shear strength components per Krawinkler's model: (a) column web component; (b) column flange component; (c) superposition.

of this flexural member can be significant when the span is small (smaller d_b) and the column flange, t_{cf}, is thick. Applying elastic beam theory, the midspan deflection when the fixed-end moment reaches $M_{p,cf}$ is

$$\begin{aligned}\Delta &= \frac{1}{3EI_{cf}}\left[\frac{M_{p,cf}}{(0.95d_b/2)}\right]\left(\frac{0.95d_b}{2}\right)^3 \\ &+ \frac{1}{GA_{s,cf}}\left[\frac{M_{p,cf}}{(0.95d_b/2)}\right]\left(\frac{0.95d_b}{2}\right) \\ &= \left[\frac{d_b^2}{1.11t_{cf}^2}+3.12\right]\frac{M_{p,cf}}{Eb_{cf}t_{cf}} \\ &= \left[\frac{\alpha^2}{1.11}+3.12\right]\frac{M_{p,cf}}{Eb_{cf}t_{cf}}\end{aligned} \tag{11}$$

In Equation 11, the coefficient α is the span-depth ratio of the column-flange flexural member:

$$\alpha = d_b/t_{cf} \tag{12}$$

The first term on the right-hand side in Equation 11 is the flexural component, and the second term is the shearing component, where $I_{cf} = b_{cf}t_{cf}^3/12$ and $A_{s,cf} = 5b_{cf}t_{cf}/6$ are the moment of inertia and shear area of one column flange, respectively. Dividing Δ by $0.95d_b/2$ and simplifying gives the shear deformation capacity of the panel zone (see Figure 18):

$$\gamma_{pz} = \frac{0.475F_{yc}}{E}\left(\alpha+\frac{3.45}{\alpha}\right) \tag{13}$$

The elastic stiffness of one column flange is

$$K_{cf} = \frac{V_{p,cf}}{\gamma_{pz}} = \frac{2M_{p,cf}}{0.95d_b\gamma_{pz}} = \frac{1.11Eb_{cf}t_{cf}}{\alpha^2+3.45} \tag{14}$$

The total elastic stiffness for both column flanges is $2K_{cf}$, as shown in Figure 17b. Therefore, the total panel zone shear

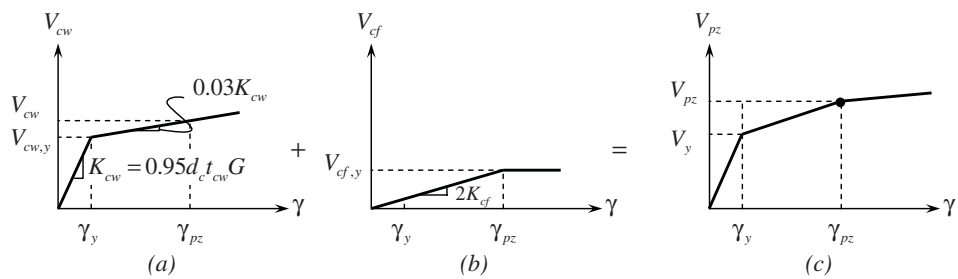

Fig. 17. Superposition of proposed shear strength components: (a) column web panel zone response; (b) response of two column flanges; (c) superposition.

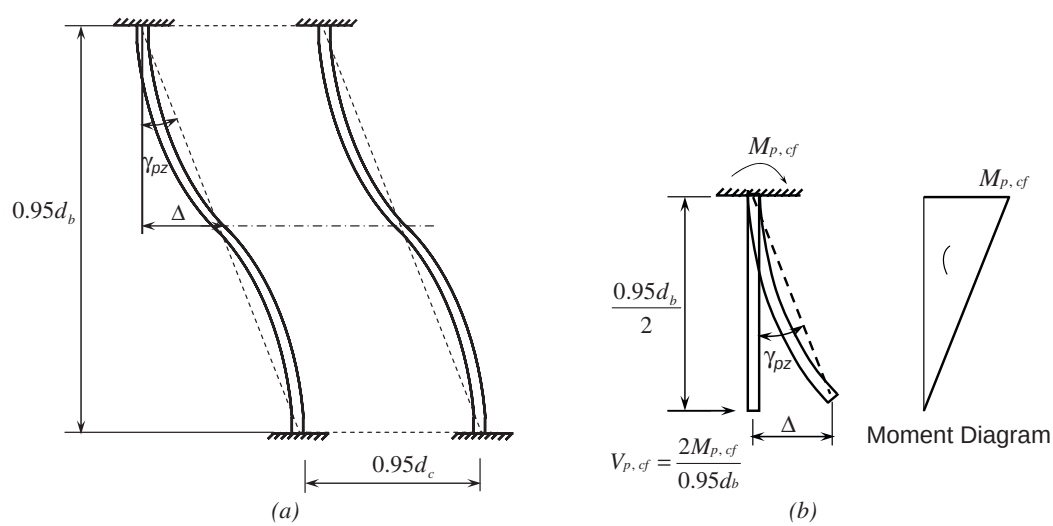

Fig. 18. Panel zone model: (a) panel zone deformation; (b) mathematical model.

strength in the elastic range is

$$V_{pz} = \left(K_{cw} + 2K_{cf}\right)\gamma \text{ when } 0 \le \gamma \le \gamma_y \quad (15)$$

When $\gamma_y < \gamma \le \gamma_{pz}$, the component of panel zone shear strength due to column web is (see Figure 17a)

$$V_{cw} = V_{cw,y} + 0.03K_{cw}\left(\gamma - \gamma_y\right) \quad (16)$$

The component of panel zone shear strength due to two column flanges is

$$V_{cf} = 2K_{cf}\gamma \quad (17)$$

Therefore, the total panel zone shear strength is

$$V_{pz} = V_{cw} + V_{cf} \quad \text{when } \gamma_y < \gamma \le \gamma_{pz} \quad (18)$$

Based on Equations 15 and 18, and replacing d_b with d_{eff}, the predicted panel zone responses for specimens 2 and 3 up to γ_{pz} are shown in Figure 19. Specimen 1 was not used in this correlation because replacement CJP welds were not used and existing CJP weld locations did not coincide with the column kinking locations. The ratios between the predicted and experimental panel zone ultimate deformations are 1.02 and 0.94 for specimens 2 and 3, respectively.

Normalizing the panel zone deformation capacity, γ_{pz}, in Equation 13 by $\gamma_y = 0.6F_y/G$ gives the following:

$$\frac{\gamma_{pz}}{\gamma_y} = 0.30\left(\alpha + \frac{3.45}{\alpha}\right) \quad (19)$$

Figure 20 shows the variation of the normalized panel zone shear deformation with respect to $\alpha = d_b/t_{cf}$. It is shown that the AISC assumed panel zone deformation capacity, $4\gamma_y$,

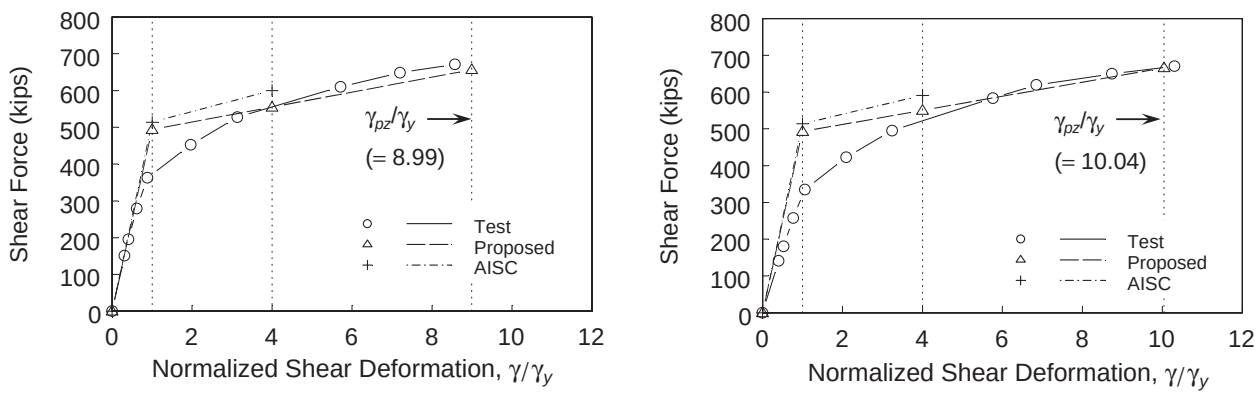

Fig. 19. Comparison of panel zone responses: (a) specimen 2; (b) specimen 3.

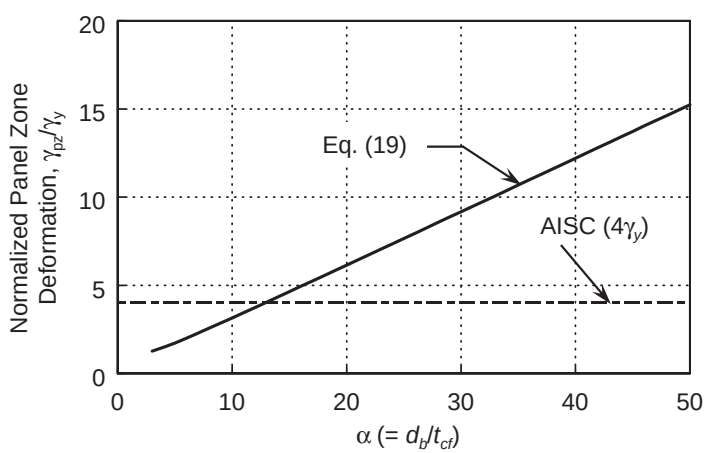

Fig. 20. Relationship between panel zone shear deformation and α.

can be very conservative for a high d_b/t_{cf} ratio. When the d_b/t_{cf} ratio is low (i.e., a shallow beam connected to a thick column flange), the panel zone deformation can be lower than $4\gamma_y$. Therefore, column flanges at kinking locations would yield early when d_b/t_{cf} is low, which makes the beam flange-to-column flange CJP welds more prone to fracture at a low panel zone deformation ($\leq 4\gamma_y$). This observation is valid for either rehabilitated or newly constructed moment connections.

Effect of Column Axial Force

With the presence of an axial load, Krawinkler et al. (1971) reported that column flanges carry all the axial load after the panel zone web has completely yielded. This is also the basis of the panel zone design shear strength with high axial load in AISC 360-10.

A column-flange cross-section and the stress distribution for the plastic moment condition are shown in Figure 21. The total stress distribution can be separated into the contributions of the axial force and bending moment. Because each column flange takes half of the column axial load, P, the axial stress equilibrium of one column flange is

$$\frac{P}{2} = (2y_p - t_{cf})\, b_{cf} F_{yc} \tag{20}$$

The axial demand-capacity ratio of one column flange is

$$\frac{P/2}{P_{y,cf}} = \frac{(2y_p - t_{cf})b_{cf} F_{yc}}{b_{cf} t_{cf} F_{yc}} = \frac{2y_p - t_{cf}}{t_{cf}} \tag{21}$$

where $P_{y,cf} = A_f F_{yc} = b_{cf} t_{cf} F_{ye}$ is the axial yield strength of one column flange and y_p designates the plastic neutral axis location. Therefore, the plastic neutral axis location is

$$y_p = \frac{t_{cf}}{2}\left(1 + \frac{P}{2P_{y,cf}}\right) \tag{22}$$

The reduced moment capacity of one column flange can be derived from Figure 21 as

$$M'_{p,cf} = 2(t_{cf} - y_p) b_{cf} F_y \left(\frac{t_{cf}}{2} - \frac{t_{cf} - y_p}{2}\right) = M_{p,cf}\left[1 - \left(\frac{P}{2P_{y,cf}}\right)^2\right] \tag{23}$$

The corresponding shear of one column-flange flexural member in Figure 18 is

$$V'_{p,cf} = \frac{2M'_{p,cf}}{0.95 d_b} = V_{p,cf}\left[1 - \left(\frac{P}{2P_{y,cf}}\right)^2\right] \tag{24}$$

Following the similar procedure described in Equations 11 and 13, the reduced plastic shear deformation can be derived by replacing $M_{p,cf}$ and $V_{p,cf}$ with $M'_{p,cf}$ and $V'_{p,cf}$:

$$\gamma'_{pz} = \frac{0.475 F_{yc}}{E}\left(\alpha + \frac{3.45}{\alpha}\right)\left[1 - \left(\frac{P}{2P_{y,cf}}\right)^2\right] = \gamma_{pz}\left[1 - \left(\frac{P}{2P_{y,cf}}\right)^2\right] \tag{25}$$

Figure 22 shows the effect of column axial load on the panel zone deformation capacity.

The associated panel zone shear strength at γ'_{pz} is established as follows. The component of panel zone shear strength due to column web from Equation 16 can be approximated as

$$V'_{cw} = V_{cw,y} + 0.03 K_{cw}\left(\gamma'_{pz} - \gamma_y\right) \tag{26}$$

From Equation 24, the component of the panel zone shear strength due to two column flanges is

$$V'_{cf} = 2V'_{p,cf} = 2V_{p,cf}\left[1 - \left(\frac{P}{2P_{y,cf}}\right)^2\right] \tag{27}$$

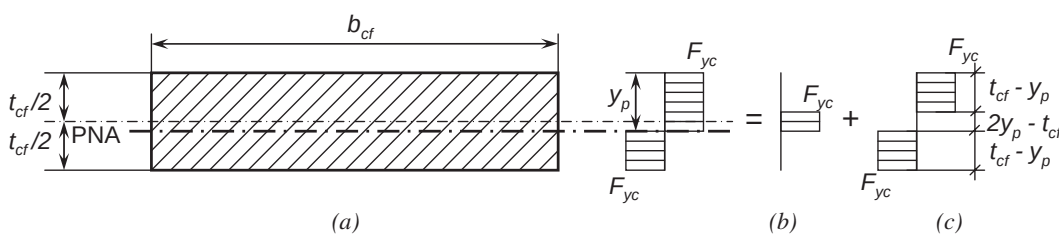

Fig. 21. Stress distribution of one column flange cross-section: (a) stress distribution in one column flange; (b) axial component; (c) flexural component.

Therefore, the total panel zone shear strength is

$$V'_{pz} = V'_{cw} + V'_{cf} \tag{28}$$

Figure 23 shows example plots of the panel zone axial load–shear strength interaction curves. A W36×150 beam with three different W14 column sections in Figure 23a and W36 column sections in Figure 23b are considered. It is observed that axial load has a more significant effect on the panel zone deformation capacity than on the shear strength. Because the interaction between axial load and panel zone shear strength is relatively weak, the axial load effect can be ignored for simplicity when $P/2P_{y,cf} < 0.6$ (or $P/P_{y,cf} < 1.2$).

SUMMARY AND CONCLUSIONS

Three full-scale specimens were tested to evaluate the cyclic performance of rehabilitated pre-Northridge steel beam-to-column moment connections. The rehabilitation included a Kaiser bolted bracket (KBB) on the beam bottom flange for all specimens, but different rehabilitation schemes were used to strengthen the beam top flange, which included the use of another KBB (specimen 1), a notch-tough complete-joint-penetration (CJP) beam flange replacement weld (specimen 2) or a welded double-tee bracket together with a replacement weld (specimen 3).

Test results showed that the proposed rehabilitation schemes adequately protected the existing pre-Northridge moment connections to the acceptable interstory drift angle. Large panel zone deformation with significant yielding occurred in all specimens; only specimen 1 also experienced beam buckling. Significant column kinking due to large panel zone deformation caused brittle fracture of the notch-tough CJP welds in specimens 2 and 3; panel zone deformation reached 0.029 rad and 0.036 rad in these specimens, respectively. Because these fractured welds were located at the column kinking locations, the test results provided useful information to verify the proposed panel zone

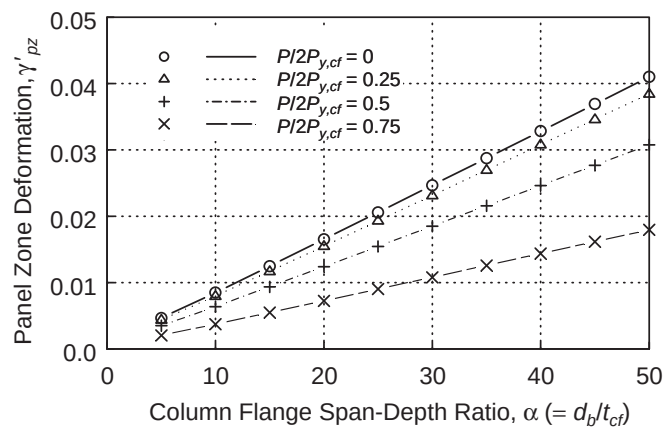

Fig. 22. Effect of column axial load on panel zone shear deformation capacity (ASTM A992 steel).

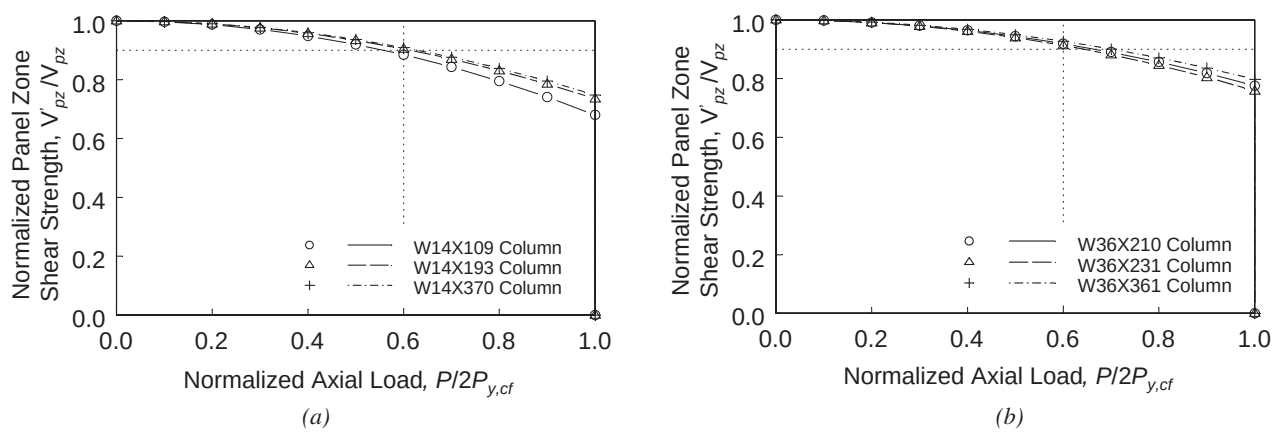

Fig. 23. Interaction of shear and axial force: (a) W14 columns; (b) W36 columns.

ultimate deformation capacity model, which used the fracture of notch-tough CJP welds at the kinking location as the limit state; the effect of column axial load was also included in the model formulation. The conclusions are summarized as follows.

1. The panel zone shear strength specified in AISC 360 corresponds to a shear deformation of $4\gamma_y$. But test results showed that the panel zone can deform more than $8\gamma_y$, although column kinking due to excessive panel zone deformation eventually caused weld fracture. Because it may not be economical and practical in seismic rehabilitation to avoid weak panel zones, a model (Figure 18) was proposed to predict the deformation capacity of the panel zone. It was postulated that the notch-tough beam flange CJP weld would fracture when the column flange was fully yielded at the kinking location. This limit state was used to define the ultimate deformation capacity of the panel zone. This postulation was calibrated with specimens 2 and 3, which experienced weld fracture. (For specimen 1, no CJP welds were located at the kinking locations.) The proposed model (see Equations 13 or 19) showed that the deformation capacity is a function of d_b/t_{cf}, where d_b = beam depth and t_{cf} = column flange thickness. The panel zone deformation capacity is small when the d_b/t_{cf} ratio is low (i.e., when a shallow beam is connected to a thick column flange), which results in earlier yielding of the column flanges at the kinking locations and makes the CJP welds more vulnerable to fracture.

2. The associated panel zone shear strength at the proposed deformation capacity level was also derived. In addition, the effect of column axial load on both the panel zone shear strength and deformation was also considered in the formulation. Its effect on the shear deformation capacity can be significant (see Equation 25). But the effect on shear strength is relatively insignificant (see Figure 23) and can be ignored when the column axial load is less than 1.2 times the yield force of one column flange.

The proposed model is also applicable to other moment connection types where the notch-tough CJP welds, not the pre-Northridge E70T-4 welds, are located at the column kinking locations. The test data available for calibrating the proposed model are scarce; only two specimens from this test program were available. Additional testing of moment connections that subject the panel zone to large deformation to induce beam flange weld fracture is needed to confirm the proposed model and to verify that the d_b/t_{cf} ratio is a key factor in determining the panel zone ultimate deformation.

ACKNOWLEDGMENTS

This project was sponsored by Civic Facilities Division of the City of Fremont and the City of Fremont Police Department. Crosby Group provided test specimen designs and technical guidance throughout the project. Steel Cast Connections provided the bolted bracket assemblies for all specimens.

REFERENCES

Adan, S.M. and Gibb, W. (2009), "Experimental Evaluation of Kaiser Bolted Bracket Steel Moment Resisting Connections," *Engineering Journal*, AISC, Vol. 46, No. 3, pp. 181–193.

AISC (2010a), *Prequalified Connections for Special and Intermediate Steel Moment Frames for Seismic Applications*, ANSI/AISC 358-10, American Institute of Steel Construction, Chicago, IL.

AISC (2010b), *Seismic Provisions for Structural Steel Buildings*, ANSI/AISC 341-10, American Institute of Steel Construction, Chicago, IL.

AISC (2010c), *Specification for Structural Steel Buildings*, ANSI/AISC 360-10, American Institute of Steel Construction, Chicago, IL.

Blaney, C., Uang, C.M., Kim, D.W., Sim, H.B. and Adan, S.M. (2010), "Cyclic Testing and Analysis of Retrofitted Pre-Northridge Steel Moment Connections Using Bolted Brackets," *Proceedings*, Annual Convention, Structural Engineers Association of California, Sacramento, CA.

El-Tawil, S., Vidarsson E., Mikesell T. and Kunnath, S.K. (1999), "Inelastic Behavior and Design of Steel Panel Zones," *Journal of the Structural Division,* ASCE, Vol. 125, No. 2, pp. 183–193.

Gross, J.L., Engelhardt, M.D., Uang, C.M., Kasai, K. and Iwankiw, N.R. (1999), "Modification of Existing Welded Steel Moment Frame Connections for Seismic Resistance," *AISC Design Guide No. 12*, American Institute of Steel Construction, Chicago, IL.

Kasai, K., Hodgon, I. and Bleiman, D. (1998), "Rigid-Bolted Repair Methods for Damaged Moment Connections," *Engineering Structures*, Vol. 20, No. 4–6, pp. 521–532.

Kato, B., Chen, W.F. and Nakao, M. (1998), "Effects of Joint-Panel Shear Deformation on Frames," *Journal of Constructional Steel Research*, Vol. 10, pp. 269–320.

Krawinkler, H., Bertero, V.V. and Popov, E.P. (1971), "Inelastic Behavior of Steel Beam-to-Column Subassemblages," EERC Report No. 71-7, University of California, Berkeley, CA.

Krawinkler, H. (1978), "Shear in Beam-Column Joints in Seismic Design of Steel Frames," *Engineering Journal*, AISC, Vol. 5, No. 3, pp. 82–91.

Lee, D., Cotton, S.C., Hajjar, J.F., Dexter, R.J. and Ye, Y. (2005), "Cyclic Behavior of Steel Moment-Resisting Connections Reinforced by Alternative Column Stiffener Details II. Panel Zone Behavior and Doubler Plate Detailing," *Engineering Journal*, AISC, Vol. 42, No. 4, pp. 215–238.

Liu, W., Givens, D., Kantikar, R. and Blaney, C. (2009), "Seismic Evaluation and Rehabilitation of a Three Story Pre-Northridge Steel Frame Essential Service Facility," *Proceedings*, ATC & SEI Conference on Improving the Seismic Performance of Buildings and Other Structures, pp. 56–67, American Society of Civil Engineers, Reston, VA.

Newell, J. and Uang, C.M. (2006), "Cyclic Testing of Steel Moment Connections for the CALTRANS District 4 Office Building Seismic Rehabilitation," UCSD Report No. SSRP-05/03, Department of Structural Engineering, University of California, San Diego, CA.

PEERC/ATC (2010), *Modeling and Acceptance Criteria for Seismic Design and Analysis of Tall Buildings,* PEER/ATC 72-1, Pacific Earthquake Engineering Research Center and Applied Technology Council.

Schneider, S.P. and Amidi, A. (1998), "Seismic Behavior of Steel Frames with Deformable Panel Zones," *Journal of the Structural Division,* ASCE, Vol. 124, No. 1, pp. 35–42.

Slutter, R.G. (1981), "Test of Panel Zone Behavior in Beam-Column Connections," Report No. 200.81.403.1, Fritz Engineering Laboratory, Lehigh University, Bethlehem, PA.

Plastic Strength of Connection Elements

BO DOWSWELL

ABSTRACT

Many connection elements are modeled as rectangular members under various combinations of shear, flexural, torsional and axial loads. Strength design is now used for steel members and connections; therefore, the traditional method of combining loads using beam theory needs to be updated to comply with strength design philosophy. Due to the extensive research available on the plastic interaction of rectangular members, a review of existing equations forms the basis of this paper. In cases where existing research is unavailable, new derivations are provided. An interaction equation is developed for strength design of rectangular connection elements under any possible loading combination.

Keywords: connections, plastic design, rectangular elements.

INTRODUCTION

For design, connections are divided into elements and modeled as structural members with well-documented and predictable behavior. Many connection elements can be modeled as rectangular members under various combinations of shear, flexural, torsional and axial loads. Traditionally, loads have been combined using beam equations with a first-yield criterion; however, a plastic strength approach is more appropriate for connections designed to the AISC *Specification* (AISC, 2010), which is based on a strength design philosophy.

The purpose of this paper is to determine the strength of rectangular connection elements subjected to various loads acting simultaneously. An interaction equation is developed for strength design of rectangular connection elements under any possible loading combination. Due to the extensive research available on the plastic interaction of rectangular members, a review of existing equations forms the basis of this paper. In cases where existing research is unavailable, new derivations are provided.

Rectangular Connection Elements

Figure 1a shows a moment connection, where the flange plates are modeled as rectangular members under axial tension and compression loads. Although other loads—such as a portion of the beam shear—will transfer through the flange plates, inelastic material behavior will allow load redistribution in ductile connection elements. This redistribution of loads allows the flange plates to be designed based on the simplified assumption of axial load only.

Bo Dowswell, P.E., Ph.D., Principal, ARC International, LLC, Birmingham, AL. Email: bo@arcstructural.com

Paper No. 2013-21

Figure 1b shows a single-plate connection, which is subjected to a constant shear load and a maximum moment at the face of the column. In some cases, such as for drag strut connections, these connections must also carry a substantial axial load. Because the moment, shear and axial loads occur at the same location on the connection element, the load interaction must be accounted for. Although typically neglected in design, twisting deformations in tests by Moore and Owens (1992), Sherman and Ghorbanpoor (2002) and Goodrich (2005) have shown that torsional stresses are also present.

The bracket, gusset and hanger connections in Figures 1c through 1e are additional examples of rectangular connection elements subjected to strong-axis bending in addition to shear and/or axial loads. Figure 1f shows the prying action of a flange, which is a rectangular connection element in weak-axis bending. In this case, the effect of the shear force is usually small and is neglected in practice.

Von Mises Criterion

Several theories have been proposed to predict the behavior of materials under multiaxial states of stress. Von Mises' criterion is considered the most accurate for predicting the initiation of yield in ductile metals when loaded by various combinations of normal and shear stresses. For plane stress, von Mises' equation reduces to

$$\sigma_e = \sqrt{\sigma_x^2 + \sigma_z^2 - \sigma_x \sigma_z + 3\tau^2} \quad (1)$$

where

σ_e = effective stress, ksi
σ_x = normal stress in the x-direction, ksi
σ_z = normal stress in the z-direction, ksi
τ = shear stress, ksi

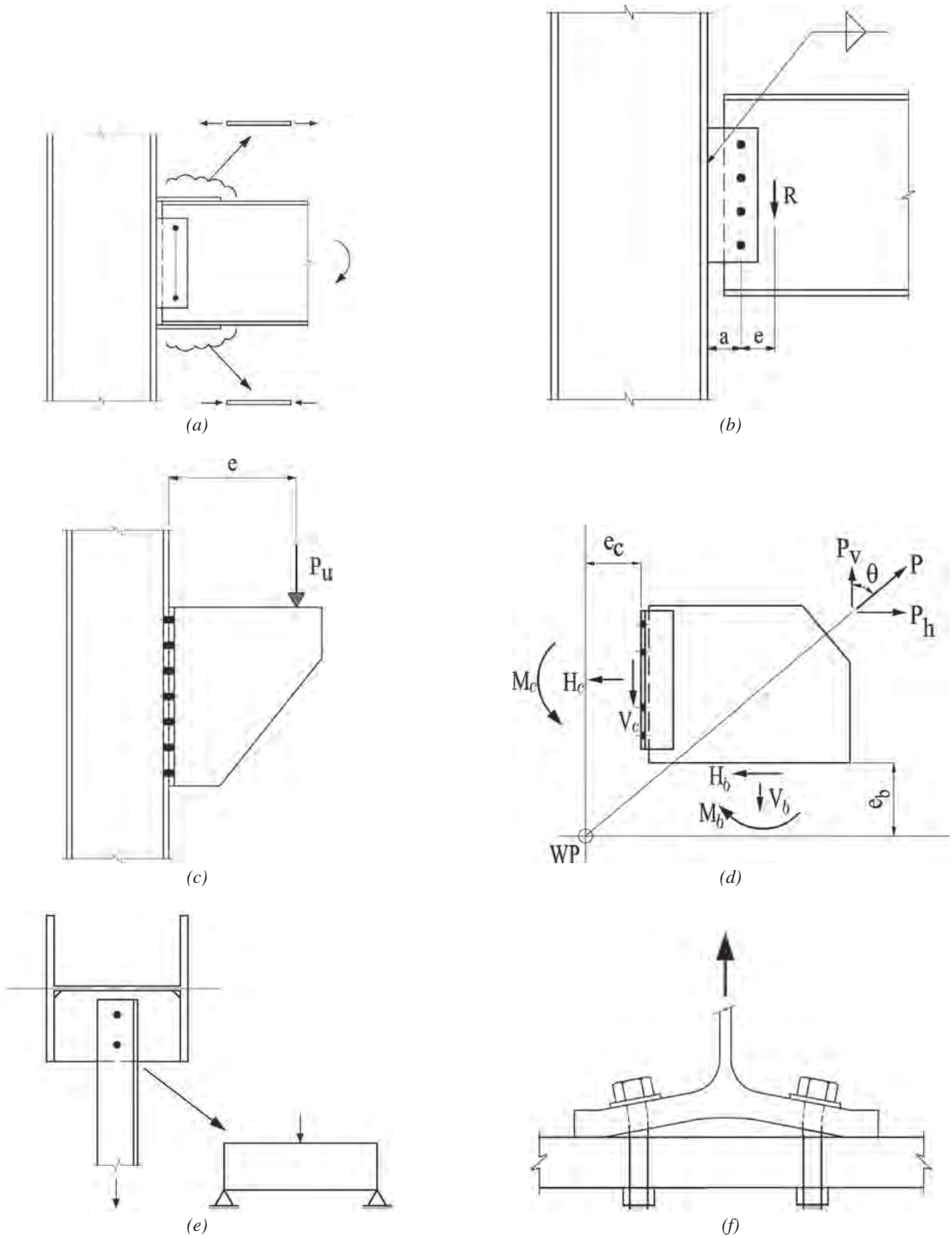

Fig. 1. Rectangular connection elements: (a) moment connection; (b) single-plate connection; (c) bracket; (d) gusset plate; (e) hanger plate; (f) prying at flange.

For elastic conditions, σ_e is limited to the tension yield strength of the steel, σ_y.

The Need for Plastic Interaction Equations

Historically, rectangular connection elements have been designed using beam theory. The normal and shear stresses are calculated with Equations 2 and 3, respectively:

$$\sigma = \frac{P}{A} \pm \frac{Mc}{I} \tag{2}$$

$$\tau = \frac{VQ}{It} \tag{3}$$

where

A = cross-sectional area, in.^{2}
M = bending moment, in.-kips
P = axial force, kips
Q = first moment of area, in.^{3}
V = shear force, kips
I = moment of inertia, in.^{4}
c = distance to outermost fiber, in.
t = thickness of the member, in.

Because the maximum normal and shear stresses occur at different locations on the cross-section, combining these stresses is not required.

To predict the true first yield load in a member, the residual stresses must be estimated. Connection elements are subjected to a wide variety of operations during manufacture, fabrication and erection. The edges have traditionally been rolled (bars and UM plates), saw-cut, sheared or thermally cut with an oxy-fuel torch. All of these operations produce different residual stress patterns. Adding to the complexity, the residual stress patterns produced by newer technologies—such as plasma cutting and water-jet cutting—are also different. Many of the cut edges are smoothed with an angle grinder, which can alter the residual stress pattern, causing a residual tension stress in most cases. A general assessment of residual stresses that accounts for all of these factors is impractical. However, because residual stresses have no effect on the plastic strength of an element, knowledge of the residual stresses are not required for strength design.

It is well known that beam theory is inaccurate at low span-to-depth ratios. Research by Karr (1956), Shawki and Hendry (1961) and Barry and Ainso (1983) generally agreed that beam theory is accurate only for simple beams with span-to-depth ratios of at least 1.5. Ahmed, Idris and Uddin (1996) showed that fixed-end beams require a span-to-depth ratio of at least 3 to get accurate results with beam theory. Tests on gusset plates by Wyss (1923), Rust (1938), Perna (1941), Sandel (1950), Whitmore (1952), Sheridan (1953), Irvan (1957), Hardin (1958), Lavis (1967) and Vasarhelyi (1971) showed that measured shear and normal stresses deviated significantly from the theoretical stresses calculated with beam equations. This was confirmed by the finite element models of Struik (1972) and White et al. (2013).

Beam theory leads to erroneous results for some plate geometries. In Figure 2a, a simple hanger connection is shown where, if $a = b$, the gusset plate is subjected to a uniform tension stress. Figure 2b shows a plot of the normalized strength versus the b/a ratio. The normalized strength is

$$\frac{P_n}{2atF_y} \tag{4}$$

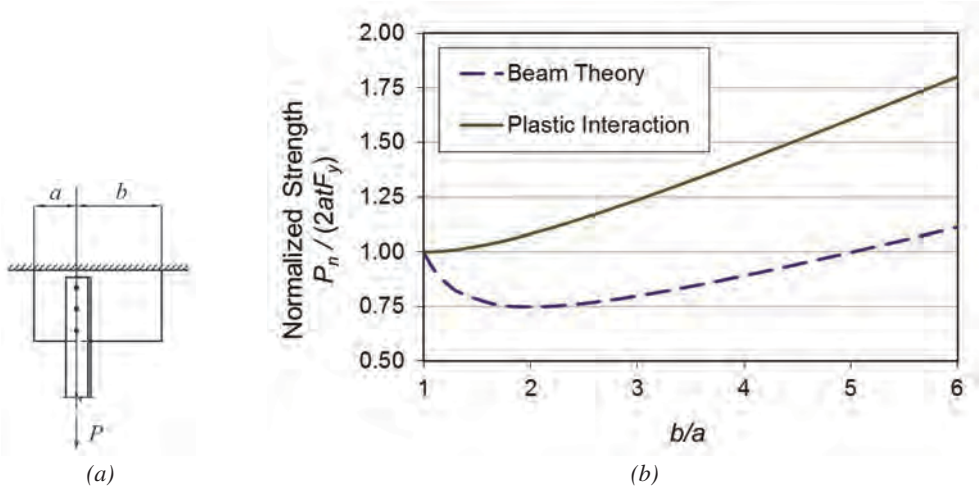

Fig. 2. Hanger connection with axial load and moment: (a) connection geometry; (b) normalized strength versus b/a ratio.

where

P_n = nominal axial strength, kips

a = plate dimension as shown in Figure 2a, in.
= half plate width for concentrically loaded case

F_y = specified minimum yield strength, ksi

If a remains constant and b increases, it is intuitive that that the strength of the gusset plate will increase; however, the dashed line in Figure 2b shows that beam theory predicts a decrease in strength in the range $1 < b/a < 5$. For the case where $b = 2a$, the plate is 50% wider than if $b = a$, but beam theory predicts only 75% of the strength. Plastic interaction, shown in Figure 2b by the solid line, conforms to the expected result—the strength increases as the plate width increases.

Strength design is now used for steel members and connections; therefore, the traditional method of combining loads using beam theory needs to be updated to comply with strength design philosophy. With difficulties in predicting the elastic stresses, the presence of discontinuities and uncertainty concerning residual stresses, plastic interaction equations are required to accurately predict the strength of connection elements.

BENDING

Due to a shape factor of 1.5, the benefit of using the plastic flexural strength of rectangular members is substantial. For this strength to be realized, the element must have sufficient rotational capacity to allow the stresses to redistribute without rupture or buckling. Schreiner (1935) and Jensen and Crispen (1938) tested cantilever plates in strong-axis bending, welded to a fixed support. They determined that the plates, which had maximum depth-to-thickness ratios of 10, can reach their plastic bending strength. More recently, tests on single-plate connections by Patrick, Thomas and Bennetts (1986) and Metzger (2006) revealed that the plastic moment capacity of the plate can be used in design.

Assuming no residual stresses, the flexural stiffness is linear up to the yield moment, M_y, and then the curve becomes nonlinear up to a maximum value of $M = M_p = 1.5M_y$, as shown in Figure 3. The inelastic part of the curve, defined by Equation 5, was derived by Nadai (1950) using linear elastic–perfectly plastic material behavior:

$$\frac{M}{M_p} = 1 - \frac{1}{3}\left(\frac{\theta_y}{\theta}\right)^2 \tag{5}$$

where

M_p = plastic bending moment, in.-kips

θ = flexural rotation

θ_y = yield rotation

To develop 96% of the plastic strength, a rotation of three times the yield rotation is required. At four times the yield rotation $M = 0.98M_p$.

Based on 14 splice plates tested in bending, Mohr and Murray (2008) determined that the flexural strength can be calculated based on the gross plastic modulus if deformation of the connection plates is not a consideration. The tests showed that the location of the initial nonlinear part of the moment-rotation curve can be accurately predicted using the first yield moment

$$M_y = \sigma_y S \tag{6}$$

where

S = gross section modulus, in.^{3}

σ_y = tension yield stress, ksi

The nominal plastic moment about the strong and weak axes are calculated with Equations 7a and 7b, respectively:

$$M_{px} = F_y Z_x \tag{7a}$$

$$M_{pz} = F_y Z_z \tag{7b}$$

The plastic moduli about the strong and weak axes are given by Equations 8a and 8b, respectively:

$$Z_x = \frac{td^2}{4} \tag{8a}$$

$$Z_z = \frac{dt^2}{4} \tag{8b}$$

where

d = depth of the member, in.

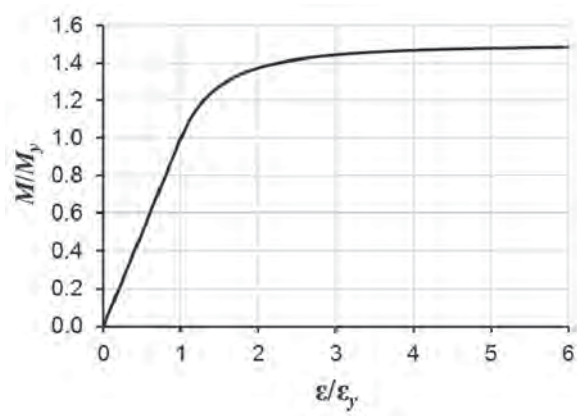

Fig. 3. Normalized moment versus normalized angle of rotation.

AXIAL

It is generally accepted that the compression yield strength is the same as the tension yield strength for ductile steels. This was verified by Seely and Putnam (1919), who showed that the compression yield strengths for mild and medium steels are about 5% greater than the tension yield strengths. The nominal axial yield force for tension or compression loads is

$$P_y = F_y A \tag{9}$$

SHEAR

Using the von Mises criterion, the shear yield stress is

$$\begin{aligned}\tau_y &= \frac{\sigma_y}{\sqrt{3}} \\ &= 0.577\sigma_y\end{aligned} \tag{10}$$

Seely and Putnam (1919) tested 21 solid circular specimens in torsion to determine the tension yield-to-shear yield ratios. The specimens, between ½ in. and ¾ in. in diameter, showed that the shear yield strength for mild and medium steels varied from 0.628 to 0.738 times the tension yield strengths. Therefore, the von Mises criterion appears to be conservative.

Based on three chevron gusset plate tests, Astaneh (1992) recommended that the plastic stress distribution be used to calculate the shear strength of gusset plates. Tests on full-scale truss bridge gusset plates by Ocel (2013) and finite element models by White et al. (2013) confirmed Astaneh's recommendation. The shear strength, based on a plastic stress distribution, is

$$V_p = \tau_y A \tag{11}$$

AISC *Specification* (AISC, 2010) Section J4.2 rounds the 0.577 factor up to 0.60, which results in a nominal shear force of

$$V_p = 0.60 F_y A \tag{12}$$

TORSION

The elastic solution for a uniform member with constant torque was solved by Saint Venant. Saint Venant torsion, also known as *uniform torsion*, assumes the applied torque is resisted by shear stresses distributed over the cross-section. This section addresses uniform torsion only and neglects the effects of warping and the Wagner effect, which causes second-order axial stresses resulting in an increased torsional stiffness (Gregory, 1960).

The rate of twist of an elastic member under uniform torsion is (Cook and Young, 1985)

$$\begin{aligned}\beta &= \frac{d\theta}{dx} \\ &= \frac{T}{GJ}\end{aligned} \tag{13}$$

For uniform members with constant torque along the length of the member, the angle of twist is the rate of twist times the member length.

$$\begin{aligned}\theta &= \beta L \\ &= \frac{TL}{GJ}\end{aligned} \tag{14}$$

where

G = shear modulus of elasticity = 11,200 ksi
J = torsional constant, in.^{4}
L = length of the member, in.
T = torsional moment, in.-kips
x = distance along the length of the member, in.
θ = angle of twist

Generally, the torsional constant for a rectangular member is

$$J = \alpha d t^3 \tag{15}$$

According to Seaburg and Carter (1997), $\alpha = ⅓ - 0.2t/d$ for $d/t < 10$ and $\alpha = ⅓$ for $d/t \geq 10$. The results using these simple equations are almost identical to the slightly more complicated equations developed by Balaz and Kolekova (2002). The torsional first yield moment is

$$T_y = \frac{\tau_y J}{t} \tag{16}$$

For $d/t \geq 10$, which satisfies the geometry for most connection elements,

$$T_y = \frac{\tau_y d t^2}{3} \tag{17}$$

When loaded beyond the yield point, the behavior of rectangular members in uniform torsion is similar to inelastic flexural behavior. Smith and Sidebottom (1965) derived the mathematical description of the inelastic part of the torsion-twist curve:

$$\frac{T}{T_y} = \frac{3}{2}(1-\eta) - \frac{1-\eta}{2\left(\theta/\theta_y\right)^2} + \eta\left(\frac{\theta}{\theta_y}\right) \tag{18}$$

where

η = strain hardening modulus for pure shear

θ_y = yield rotation

The accuracy of Equation 18 has been verified by the inelastic finite element models of Shunsuke and Kajita (1982) and May and Al-Shaarbaf (1989). The yield rotation can be determined by substituting Equation 16 into Equation 14:

$$\theta_y = \frac{\tau_y L}{Gt} \tag{19}$$

Due to the torsional flexibility of rectangular members, it is unlikely that they will strain beyond the yield plateau of mild steel. Therefore, $\eta = 0$ in the range of serviceable rotations, which gives the equation for linear elastic–perfectly plastic material behavior:

$$\frac{T}{T_y} = 1.5 - 0.5\left(\frac{\theta_y}{\theta}\right)^2 \tag{20}$$

The torsional stiffness is linear up to the yield moment, T_y, and then the curve becomes nonlinear up to a maximum value of $T = T_p = 1.5T_y$, as shown in Figure 4. Substituting $T_p = 1.5T_y$ into Equation 20 results in Equation 21, which was derived independently by Billinghurst et al. (1992):

$$\frac{T}{T_p} = 1 - \frac{1}{3}\left(\frac{\theta_y}{\theta}\right)^2 \tag{21}$$

where

T_p = plastic torsional moment, in.-kips

Equation 21 has the identical form of Equation 5, which was derived for flexural rotation. To develop 96% of the plastic strength, a rotation of three times the yield rotation is required. At four times the yield rotation $T = 0.98T_p$.

The plastic torsion strength can also be derived using the stress function. For any stress condition, the torsion strength is twice the volume under the stress function, ϕ (Smith and Sidebottom, 1965). Therefore, the plastic strength can be determined with Equation 22:

$$T_p = 2\int\int \phi \, dx dz \tag{22}$$

where

x, z = cross-sectional coordinates

The absolute value of the slope of ϕ everywhere on the cross-section is τ_y for fully plastic conditions. At the boundaries of the cross-section, ϕ must be zero, and the value of ϕ at any point on the cross-section is τ_y times the perpendicular distance to the boundary. This stress condition, known as the sand heap analogy, is illustrated in Figure 5.

For rectangular members with high aspect (d/t) ratios, the boundary effects parallel to the longest cross-sectional dimension can be neglected. In this case, the stress function is two-dimensional and the plastic strength is

$$\begin{aligned} T_p &= 2d\tau_y \int_{-t/2}^{t/2} x \, dx \\ &= 4d\tau_y \int_{-t/2}^{0} x \, dx \\ &= \frac{\tau_y d t^2}{2} \end{aligned} \tag{23}$$

By comparing Equation 17 to Equation 23, it can be seen that $T_p = 1.5T_y$. The nominal torsion strength is

$$T_p = 0.3F_y dt^2 \tag{24}$$

INTERACTION

A review of the existing research indicated that plastic interaction equations for several loading combinations have been available for decades. This section of the paper documents the available research, compares the different interaction equations, develops new equations where existing research

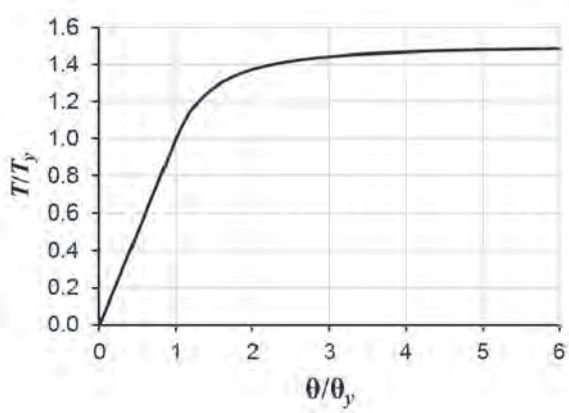

Fig. 4. Normalized torsion versus normalized angle of twist.

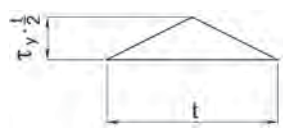

Fig. 5. Stress distribution for plastic torsional strength.

is unavailable and compares the equations to test data where available.

The derivations are based on assumed stress distributions, which complies with the lower-bound theorem of limit analysis. According to the lower-bound theorem, a load calculated with an assumed distribution that satisfies equilibrium, with stresses nowhere exceeding the yield stress, will be less than or equal to the true limit load. Where more than one solution is available, the solution that gives the highest strength is closest to the true strength. All interaction equations discussed in this paper assume perfectly plastic material behavior under plane stress conditions.

Moment-Axial Interaction

Because axial and flexural loads both cause normal stresses in the member, engineers may simply replace the section modulus with the plastic modulus in the beam equation, which results in a linear interaction. This is a conservative assumption because the stresses can be combined using the lower-bound theorem, which allows the axial stresses to be placed at a location that is least detrimental to the flexural strength.

Freudenthal (1950) derived the plastic interaction equation for combined axial and flexural loads. Also see Seely and Smith (1952), Vrouwenvelder (2003), Chen and Han (2007) and Galambos and Surovek (2008) for similar approaches to the derivation with identical results. The derivation is based on the assumed stress blocks in Figure 6, which locates the resistance to axial load at the center of the cross-section because the outer stress blocks are most efficient for flexural resistance.

The reduced axial strength in the presence of an applied moment is defined by the area of the shaded part of Figure 6:

$$P = ht\sigma_y \tag{25}$$

where

h = depth of the central region of the cross-section resisting the axial force, in.

The reduced flexural strength in the presence of an applied axial load is defined by the nonshaded part of Figure 6:

$$M = \frac{td^2}{4}\sigma_y - \frac{th^2}{4}\sigma_y \tag{26}$$

The axial strength ratio is

$$\frac{P}{P_y} = \frac{ht\sigma_y}{dt\sigma_y} = \frac{h}{d} \tag{27}$$

The flexural strength ratio is

$$\frac{M}{M_p} = \frac{\frac{td^2}{4}\sigma_y - \frac{th^2}{4}\sigma_y}{\frac{td^2}{4}\sigma_y} = 1 - \left(\frac{h}{d}\right)^2 \tag{28}$$

Combining Equations 27 and 28 results in Equation 29:

$$\frac{M}{M_p} + \left(\frac{P}{P_y}\right)^2 = 1.0 \tag{29}$$

Equation 29 is plotted in Figure 7 along with the interaction according to beam theory. For comparison, the interaction

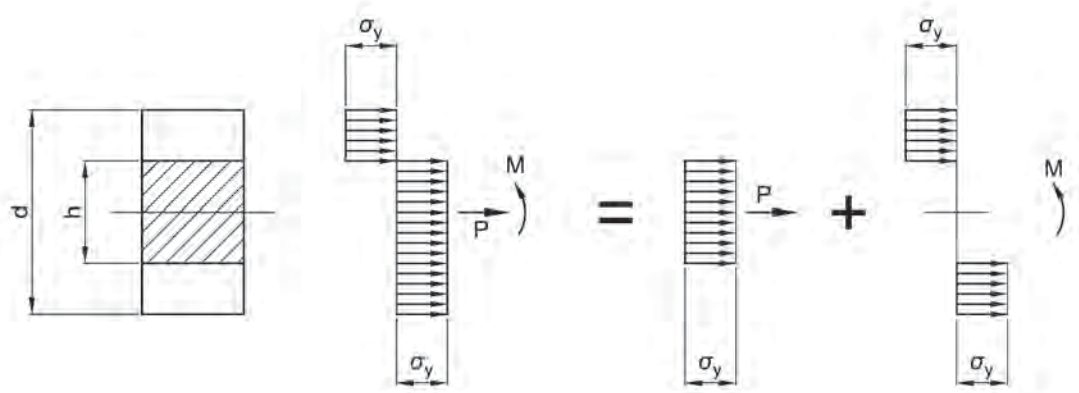

Fig. 6. Stress blocks for moment-axial interaction.

curves of AISC *Specification* Sections H1 and H2 are also plotted in the figure.

The plastic interaction equations were verified by the experiments of Sidebottom and Clark (1958), who tested nine identical, mild steel rectangular members. The specimens had a yield stress of 30 ksi and a modulus of elasticity of 30,000 ksi. The cross-sectional dimensions were 0.900 in. × 1.15 in. An axial compression load was applied with an eccentricity of 0.345 in. causing strong-axis moment. Using Equation 29, the test-to-predicted ratio ranged from 0.926 to 1.12, with an average of 0.990.

Moment-Shear Interaction

Because the maximum shear and normal stresses act at the same location on the cross-section, the flexural strength can be reduced in the presence of shear loading. In contrast to moment-axial interaction, which has a unique solution, several solutions are available for moment-shear interaction. Derivations and assumed stress distributions are provided only where they relate to later parts of this paper.

An elliptical interaction equation can be derived, based on von Mises' criterion with a constant shear stress assumed over the cross-section. For normal stress in one direction combined with shear, von Mises' criterion reduces to

$$\sigma_y = \sqrt{\sigma^2 + 3\tau^2} \tag{30}$$

where

σ = normal stress, ksi

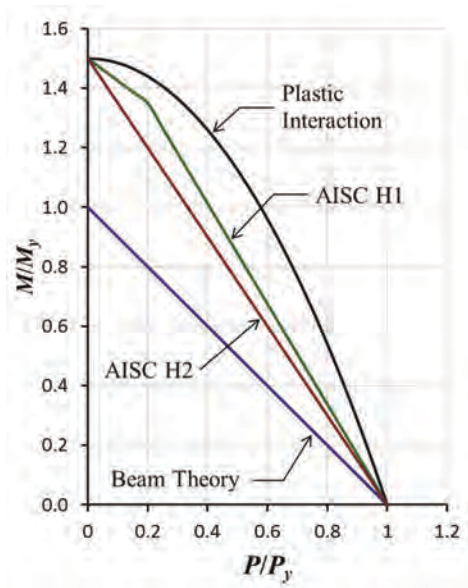

Fig. 7. Interaction of flexural and axial loads.

The moment and shear loads acting on the cross-section are given by Equations 31 and 32, respectively:

$$M = \frac{\sigma t d^2}{4} \tag{31}$$

$$V = \tau t d \tag{32}$$

The plastic flexural strength with no shear is

$$M_p = \sigma_y \frac{t d^2}{4} \tag{33}$$

The plastic shear strength with no moment is

$$V_p = \frac{\sigma_y}{\sqrt{3}} t d \tag{34}$$

Solving Equations 31 and 32 for σ and τ, respectively, substituting into Equation 30 and combining with Equations 33 and 34 results in Equation 35:

$$\left(\frac{M}{M}\right)^2 + \left(\frac{V}{V}\right)^2 = 1.0 \tag{35}$$

Paltchevskiy (1948) (see translation in Mrazik, Skaloud and Tochacek, 1987) assumed rectangular stress blocks for shear and flexural stresses as shown in Figure 8a. Based on this, the flexural strength is

$$M = M_p \left[1 - \left(\frac{h}{d}\right)^2\right] \tag{36}$$

where

h = depth of the central region of the cross-section resisting the shear force, in.

The shear strength is

$$V = V_p \left(\frac{h}{d}\right) \tag{37}$$

Solving Equation 37 for h/d and substituting into Equation 36 results in Equation 38:

$$\frac{M}{M_p} + \left(\frac{V}{V_p}\right)^2 = 1.0 \tag{38}$$

By considering equilibrium of the shear and flexural loads in the plastic zone of a rectangular beam, Horne (1951) derived Equation 39, which is valid for $V/V_p \le 0.792$. The shear yield strength was based on the Tresca criterion, which results in a shear yield stress of $\sigma_y/2$:

$$\frac{M}{M_p} + 0.444\left(\frac{V}{V_p}\right)^2 = 1.0 \tag{39}$$

Substituting a shear yield stress of $0.6\alpha_y$ changes the constant to 0.592 and the range of validity to $V/V_p \le 0.686$:

$$\frac{M}{M_p} + 0.592\left(\frac{V}{V_p}\right)^2 = 1.0 \tag{40}$$

Broude (1953) (see translation in Mrazik et al., 1987) developed a solution, based on the differential equations of equilibrium, that he solved for several discrete values. He determined a close curve fit to the discrete values, which is almost identical to the elliptical equation derived from the von Mises' criterion:

$$\left(\frac{M}{M_p}\right)^2 + \left(\frac{V}{V_p}\right)^2 - 0.0074\left(\frac{M}{M_p}\right)^2\left(\frac{V}{V_p}\right)^2 = 1.0 \tag{41}$$

Based on equilibrium of rectangular and triangular blocks for flexural stresses and a parabolic block for shear stresses, Neal (1963) (also see Chakrabarty, 2006) derived Equation 44. The assumed cross-sectional stresses are shown in Figure 8b. Based on equilibrium of the stress blocks, the flexural and shear strengths are given by Equations 42 and 43, respectively:

$$M = \frac{\sigma_y t}{4}\left(d^2 - \frac{h^2}{3}\right) \tag{42}$$

$$V = \frac{2}{3}\tau_y t h \tag{43}$$

Solving Equation 43 for y, substituting into Equation 42 and combining with Equations 33 and 34 results in Equation 44:

$$\frac{M}{M_p} + \frac{3}{4}\left(\frac{V}{V_p}\right)^2 = 1.0 \tag{44}$$

Because $h \le d$, Equation 44 is valid for the range $V/V_p \le 2/3$.

Drucker (1956) derived upper- and lower-bound solutions based on limit analysis theorems. Equation 45 was proposed as an approximation that "nearly coincides with a lower bound and is not too far from possible upper bounds":

$$\frac{M}{M_p} + \left(\frac{V}{V_p}\right)^4 = 1.0 \tag{45}$$

Johnson, Chitkara and Ranshi (1974) derived the plastic collapse strength using slip line fields. Their derivation was based on plane stress conditions using the von Mises yield criterion. Due to the complicated nature of the solution, it cannot be expressed as an interaction equation. Figure 9 shows the available solutions for moment-shear interaction. Because the curve defined by the slip line solution of Johnson et al. (1974) is the least conservative, it is closest to the true solution. Observation of the interaction equations reveals that the elliptical interaction defined by Equation 35 is more accurate at low values of M/M_p and Equation 45, developed by Drucker (1956), is more accurate at high values of M/M_p. Equations 35 and 45 are equal at $M/M_p = 0.618$ and $V/V_p = 0.786$. The solid data points are from tests on full-size gusset plates by Ocel (2013) and the hollow data points are from inelastic finite element models by White et al. (2013).

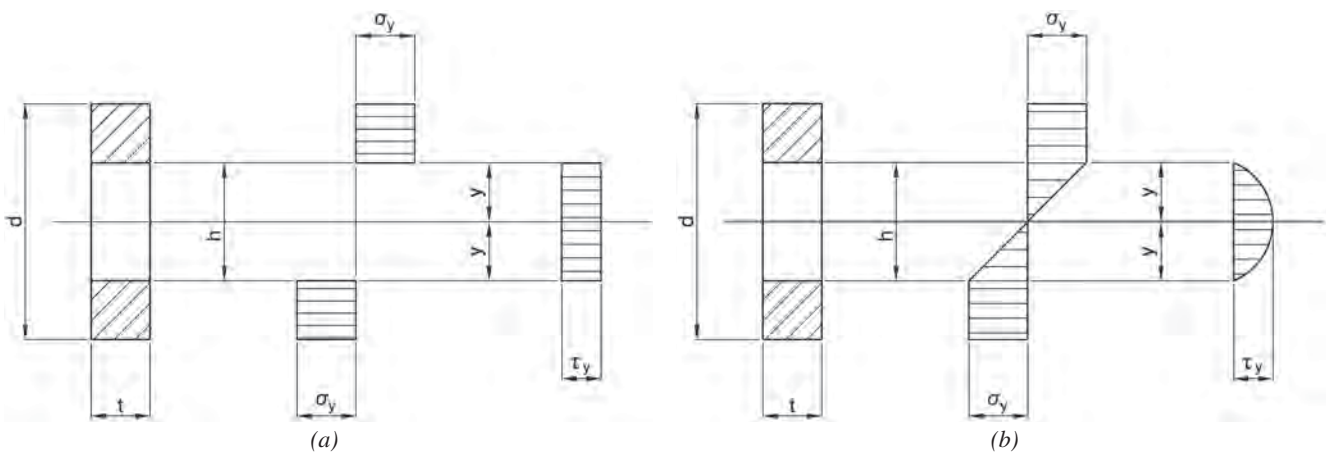

Fig. 8. Assumed stress blocks for moment-shear interaction: (a) Paltchevskiy (1948); (b) Neal (1963).

Moment-Shear-Axial Interaction

Neal (1961) derived upper- and lower-bound solutions for rectangular beams subjected to combined moment, shear and axial loads based on limit analysis theorems. Equation 46 was proposed as a "good approximation to the lower-bound interaction relation." He noted that the equation is exact for $V/V_p = 0$ and the discrepancy from the lower-bound solution never exceeds 5% for the full range of values:

$$\frac{M}{M_p}+\left(\frac{P}{P_y}\right)^2+\frac{\left(\frac{V}{V_p}\right)^4}{1-\left(\frac{P}{P_y}\right)^2}=1.0 \tag{46}$$

Astaneh (1998) summarized the previous research and relevant code provisions for the seismic design of gusset plates. He removed second-order interaction on the shear term of Equation 46 and recommended Equation 47 for design:

$$\frac{M}{M_p}+\left(\frac{P}{P_y}\right)^2+\left(\frac{V}{V_p}\right)^4\le 1.0 \tag{47}$$

Biaxial Bending

Using the lower-bound theorem of limit analysis, Harrison (1963) derived Equations 48a and b, which define a two-part interaction curve for biaxial bending.

When $M_x/M_{px} \ge 2/3$ and $M_z/M_{pz} < 2/3$,

$$\frac{M_x}{M_{px}}+\frac{3}{4}\left(\frac{M_z}{M_{pz}}\right)^2=1.0 \tag{48a}$$

When $M_x/M_{px} < 2/3$ and $M_z/M_{pz} \ge 2/3$,

$$\frac{3}{4}\left(\frac{M_x}{M_{px}}\right)^2+\frac{M_z}{M_{pz}}=1.0 \tag{48b}$$

where

M_{px} = plastic bending moment about the x-axis, in.-kips
M_{pz} = plastic bending moment about the z-axis, in.-kips
M_x = bending moment about the x-axis, in.-kips
M_z = bending moment about the z-axis, in.-kips

Harrison (1963) tested six mild steel rectangular members in biaxial bending. The cross-sectional dimensions were 0.300 in. × 0.500 in., and the yield strength was 36.6 ksi. The

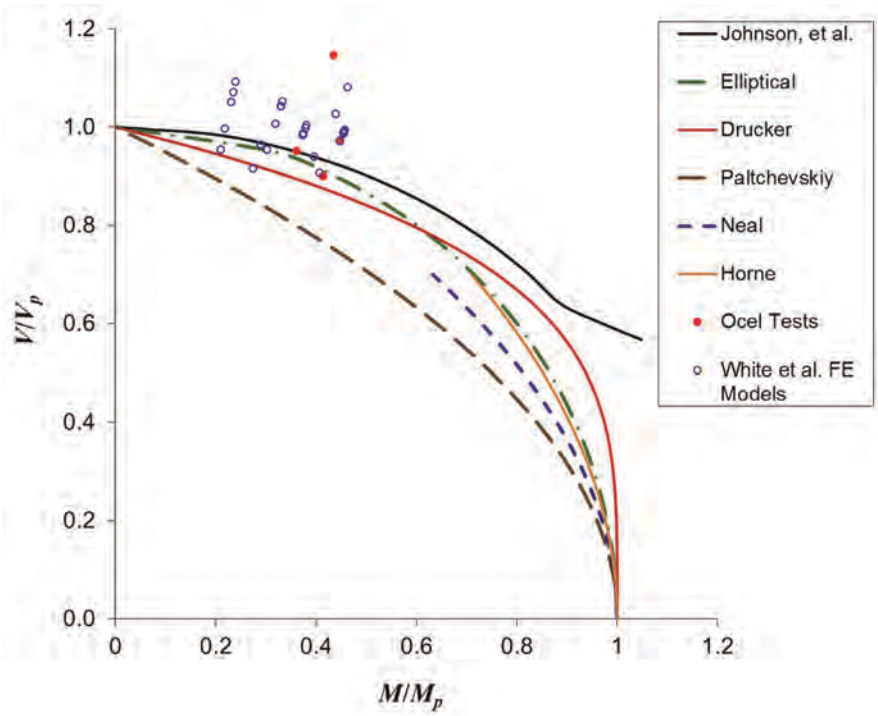

Fig. 9. Moment-shear interaction curves.

span was 18 in. with concentrated loads at ⅓ points, loading each principal axis. The ends were fixed against rotation in both directions. The interaction curve is in good agreement with the experimental results, with the greatest discrepancy being 4%. Figure 10 shows the experimental results plotted with the interaction curve defined by Equations 48a and b.

Axial Load Combined with Biaxial Bending

Santathadaporn and Chen (1970) (also see Chen and Atsuta, 1977) extended Equations 48a and b to include the effect of axial load. They presented the solution as a three-part interaction curve, defined by Equations 49a, b and c:

When $M_x/M_{px} \geq (⅔)(1 - P/P_y)$ and $M_z/M_{pz} < (⅔)(1 - P/P_y)$

$$\left(\frac{P}{P_y}\right)^2 + \frac{M_x}{M_{px}} + \frac{3}{4}\left(\frac{M_z}{M_{pz}}\right)^2 = 1.0 \qquad (49a)$$

When $M_x/M_{px} < (⅔)(1 - P/P_y)$ and $M_z/M_{pz} \geq (⅔)(1 - P/P_y)$

$$\left(\frac{P}{P_y}\right)^2 + \frac{3}{4}\left(\frac{M_x}{M_{px}}\right)^2 + \frac{M_z}{M_{pz}} = 1.0 \qquad (49b)$$

When $M_x/M_{px} \geq (⅔)(1 - P/P_y)$ and $M_z/M_{pz} \geq (⅔)(1 - P/P_y)$

$$\left(\frac{P}{P_y}\right)^2 + \frac{9}{4}\left[1 - \frac{M_x}{2\left(1 - P/P_y\right)}\right]\left[1 - \frac{M_z}{2\left(1 - P/P_y\right)}\right] = 1.0 \qquad (49c)$$

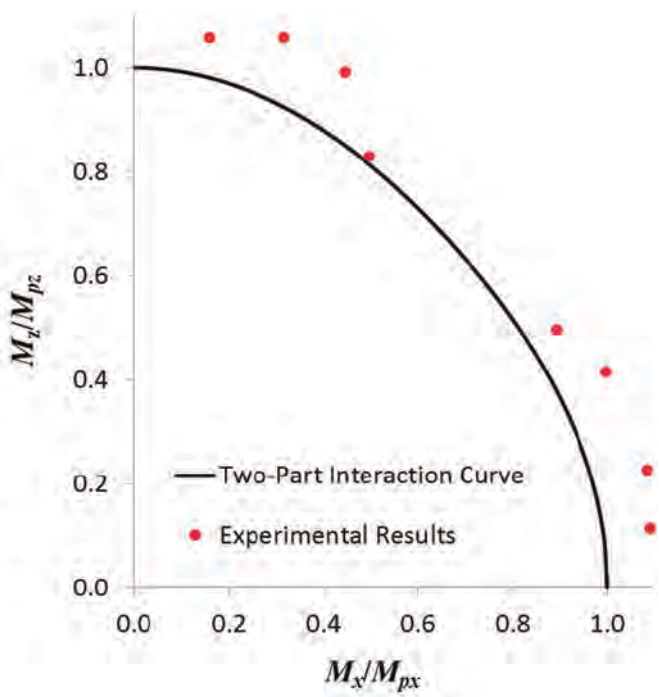

Fig. 10. Interaction curve for biaxial bending.

Because these equations are cumbersome for design use, a single interaction equation can be developed as a best fit to the three-part curve. The continuous interaction curve developed by Duan and Chen (1989) for wide flange members is

$$\left(\frac{P}{P_y}\right)^2 + \left[\left(\frac{M_x}{M_{px}}\right)^\alpha + \left(\frac{M_z}{M_{pz}}\right)^\alpha\right]^{1/\alpha} = 1.0 \qquad (50)$$

Because the exponent, α, is not necessarily accurate for rectangular members, a new equation was developed by curve fitting the three-part curve. A numerical value of α was determined for each increment of P/P_y, which gave the best fit for that value of P/P_y. Equation 51 was determined by curve fitting all values of α:

$$\alpha = 1.7\left[1 - \frac{1}{4}\left(\frac{P}{P_y}\right) + \left(\frac{P}{P_y}\right)^2\right] \qquad (51)$$

The family of curves defined by Equations 50 and 51 are shown in Figure 11a. To simplify the equations, it may be beneficial to use a constant value of α. Figure 11b shows the family of curves defined by Equation 50 with α = 1.7. This solution appears to be adequate for design use, with the greatest discrepancies being conservative, at high P/P_y ratios.

Torsion-Shear Interaction

The interaction between torsion and shear loads is analogous to moment-axial interaction. The stresses in the central region of the cross-section are assigned to resist the shear force, and the torsional moment is resisted by the areas on the cross-section farthest from the shear center. The reduced shear strength in the presence of an applied torsional moment is defined by the area of the shaded part of Figure 12a:

$$V = bd\tau_y \qquad (52)$$

where

b = width of the central region of the cross-section resisting the shear force, in.

The reduced torsional strength in the presence of an applied shear load is defined by the nonshaded part of Figure 12a. From the diagram in Figure 12b,

$$T = 2\int\int \phi \, dx dz \tag{53}$$
$$= 4d\tau_y \int_{-t/2}^{-b/2} x \, dx$$
$$= \frac{\tau_y d}{2}\left(t^2 - b^2\right)$$

The shear strength ratio is

$$\frac{V}{V_p} = \frac{bd\tau_y}{td\tau_y} \tag{54}$$
$$= \frac{b}{t}$$

The torsional strength ratio is

$$\frac{T}{T_p} = \frac{\frac{\tau_y d}{2}\left(t^2 - b^2\right)}{\frac{\tau_y d t^2}{2}} \tag{55}$$
$$= 1 - \left(\frac{b}{t}\right)^2$$

Combining Equations 54 and 55 results in Equation 56.

$$\frac{T}{T_p} + \left(\frac{V}{V_p}\right)^2 = 1 \tag{56}$$

Equation 56 is plotted in Figure 13 along with the interaction according to elastic theory.

Moment-Axial-Torsion Interaction

Hill and Siebel (1953) (also see Chakrabarty, 2006) derived a lower-bound approximation for the interaction of axial, flexure and torsional loads:

$$\left(\frac{P}{P_y}\right)^2 + \left(\frac{T}{T_p}\right)^2 + \frac{M}{M_p}\sqrt{1 - \left(\frac{T}{T_p}\right)^2} = 1.0 \tag{57}$$

Calladine (1969) (also see Mrazik et al., 1987) recommended the following lower-bound interaction equations for use with all cross-sectional shapes. Calladine (1969) noted that with information on the cross-sectional shape, the equations could be refined and become less conservative:

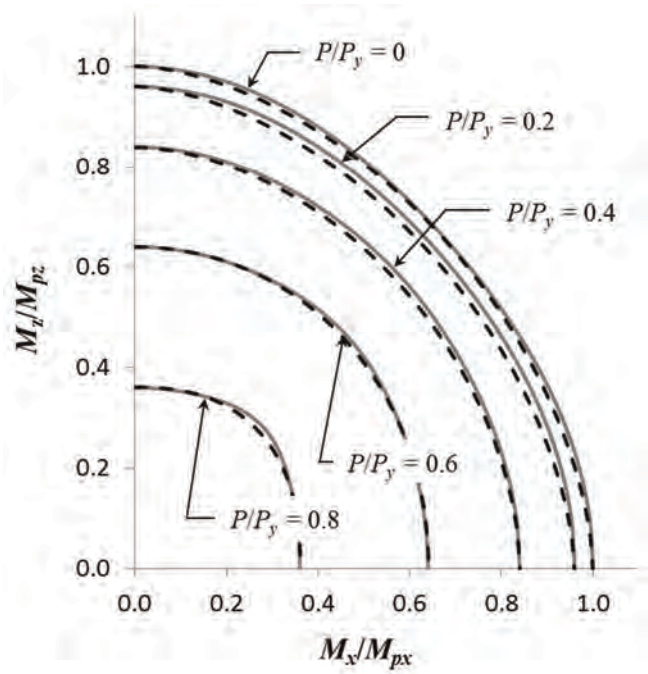

Solid lines defined by Equations 1
Dashed lines defined by Equations 49 and 50
(a)

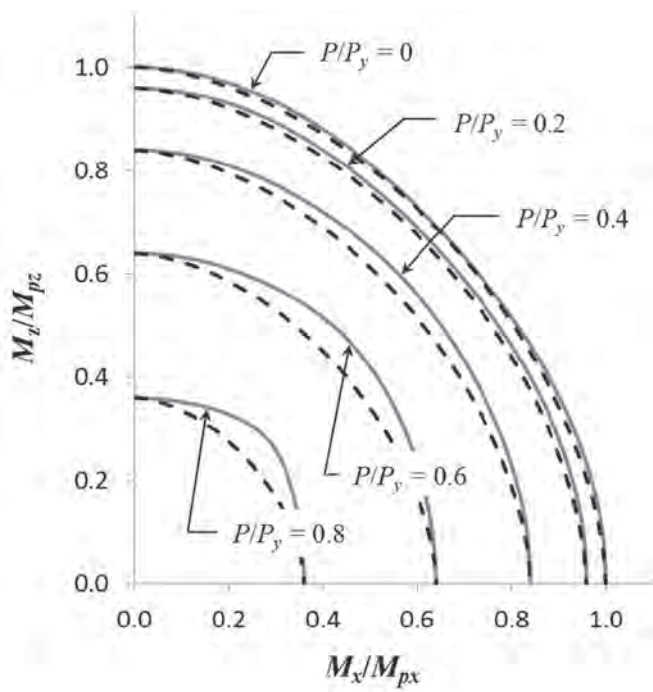

Solid lines defined by Equations 1
Dashed defined by Equation 49 with $\alpha = 1.7$
(b)

Fig. 11. Interaction curves for axial load and biaxial bending: (a) variable α; (b) constant α.

$$\left(\frac{T}{T_p}\right)^2+\left(\frac{P}{P_y}\right)^2=1.0 \tag{58}$$

$$\left(\frac{T}{T_p}\right)^2+\left(\frac{M}{M_p}\right)^2=1.0 \tag{59}$$

Equation 58 is equal to Equation 57 when $M = 0$, and Equation 59 is equal to Equation 57 when $P = 0$. Steele (1954) used the finite difference method to verify the accuracy of Equation 59. The equation was shown to give accurate lower-bound estimates of the interaction. Gill and Boucher (1964) tested 18 square and rectangular specimens in combined bending and torsion. The specimens were ⅝-in. × ⅝-in. and ⅜-in. × ⅝-in. cross-sections with a 12¾-in. span. The results are shown in Figure 14 along with Equation 59, which is clearly a lower bound to the test data.

Morris and Fenves (1969) derived a lower-bound solution for rectangular members under axial load, biaxial bending and torsion. The von Mises yield criterion was used to show that the reduced effective yield strength is

$$F_y'=\rho F_y \tag{60}$$

The yield strength reduction factor is

$$\rho=\sqrt{1-\left(\frac{T}{T_p}\right)^2} \tag{61}$$

As a general rule, interaction equations can be developed by multiplying any resisting load that produces a normal stress on the cross-section by ρ. For moment-axial-torsion interaction, this gives

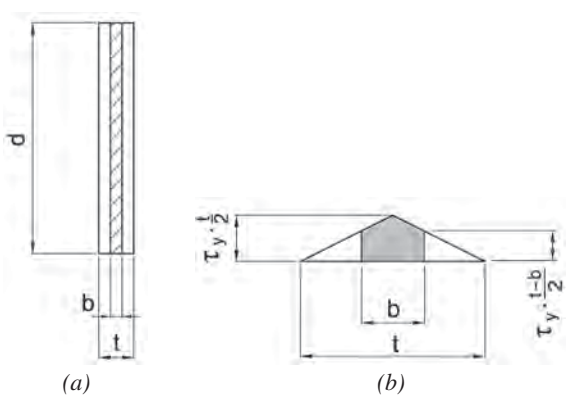

Fig. 12. Torsion-shear interaction: (a) cross-section; (b) torsion diagram.

$$\frac{\left(P/P_y\right)^2}{1-\left(T/T_p\right)^2}+\frac{M/M_p}{\sqrt{1-\left(T/T_p\right)^2}}=1.0 \tag{62}$$

If each side of the equation is multiplied by $1 - (T/T_p)^2$, it can be seen that Equation 62 is identical to Equation 57; therefore, the equations by Hill and Siebel (1952), Calladine (1969) and Morris and Fenves (1969) give identical results. Using the theory of Morris and Fenves, the interaction equation can be expanded to cover biaxial moments:

$$\left(\frac{P}{P_y}\right)^2+\left(\frac{T}{T_p}\right)^2+\left[\left(\frac{M_x}{M_{px}}\right)^\alpha+\left(\frac{M_z}{M_{pz}}\right)^\alpha\right]^{1/\alpha}\sqrt{1-\left(\frac{T}{T_p}\right)^2}=1.0 \tag{63}$$

DESIGN

To develop a single interaction equation that accounts for all loading possibilities, Equation 63 can be combined with Equation 45. This will account for all load interactions except torsion-shear. The reduction in shear strength due to torsional loading can be determined by rearranging Equation 56, which results in Equation 64:

$$\frac{\left(\frac{V}{V_p}\right)^2}{1-\frac{T}{T_p}}=1.0 \tag{64}$$

Combining Equations 63, 45 and 64 results in Equation 65.

$$\left(\frac{P_r}{P_y}\right)^2+\left(\frac{T_r}{T_p}\right)^2+\frac{\left(\frac{V_r}{V_p}\right)^4}{\left[1-\left(\frac{P_r}{P_y}\right)^2\right]\left(1-\frac{T_r}{T_p}\right)^2}$$
$$+\left[\left(\frac{M_{rx}}{M_{px}}\right)^\alpha+\left(\frac{M_{rz}}{M_{pz}}\right)^\alpha\right]^{1/\alpha}\sqrt{1-\left(\frac{T_r}{T_p}\right)^2}=1.0 \tag{65}$$

where

M_{rx} = required x-axis bending moment, in.-kips
M_{rz} = required z-axis bending moment, in.-kips
P_r = required axial force, kips
T_r = required torsional moment, in.-kips
V_r = required shear force, kips

For biaxial shear, the transverse forces are combined vectorially, according to Equation 66:

$$V_r = \sqrt{V_{rx}^2 + V_{rz}^2} \tag{66}$$

where

V_{rx} = required x-axis shear force, in.-kips
V_{rz} = required z-axis shear force, in.-kips

Because the torsion strength can be greatly underestimated by neglecting the effects of warping and the Wagner effect, the detrimental effect of the second-order shear-torsion interaction term and the beneficial effect of the second-order moment-torsion interaction term can be neglected. Because the shear interaction term is conservative, based on the true limit load defined by Johnson et al. (1974), the second-order shear-axial interaction term can be neglected. Substituting a constant value of 1.7 for α and neglecting the second-order interaction terms for each independent load ratio results in Equation 67, which is proposed for design:

$$\left(\frac{P_r}{P_y}\right)^2 + \left(\frac{T_r}{T_p}\right)^2 + \left(\frac{V_r}{V_p}\right)^4 + \left[\left(\frac{M_{rx}}{M_{px}}\right)^{1.7} + \left(\frac{M_{rz}}{M_{pz}}\right)^{1.7}\right]^{0.59} = 1.0 \tag{67}$$

CONCLUSIONS

In design, many connection elements are modeled as rectangular members under various combinations of shear, flexural, torsional and axial loads. This paper shows that beam theory, and other design models using a first-yield criterion, severely underestimates the strength of rectangular connection elements. Existing research and new derivations were used to develop a plastic interaction equation, which has been proposed for design of rectangular elements subjected to any possible combination of loads. Experimental results are available for four load interaction cases: axial-flexure, shear-flexure, torsion-flexure and biaxial flexure. For these cases, the proposed interaction equation compares well with the experimental results. However, future testing may be needed to validate the equation for other load interaction cases.

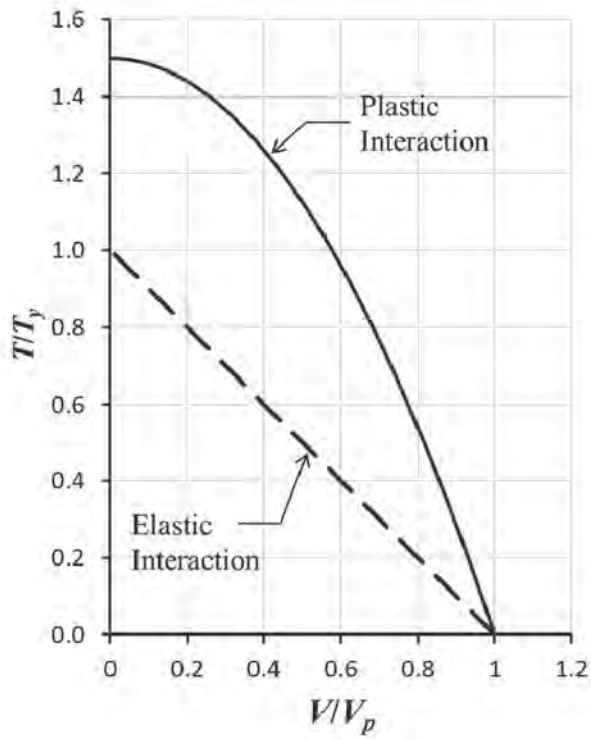

Fig. 13. Interaction of torsion and shear loads.

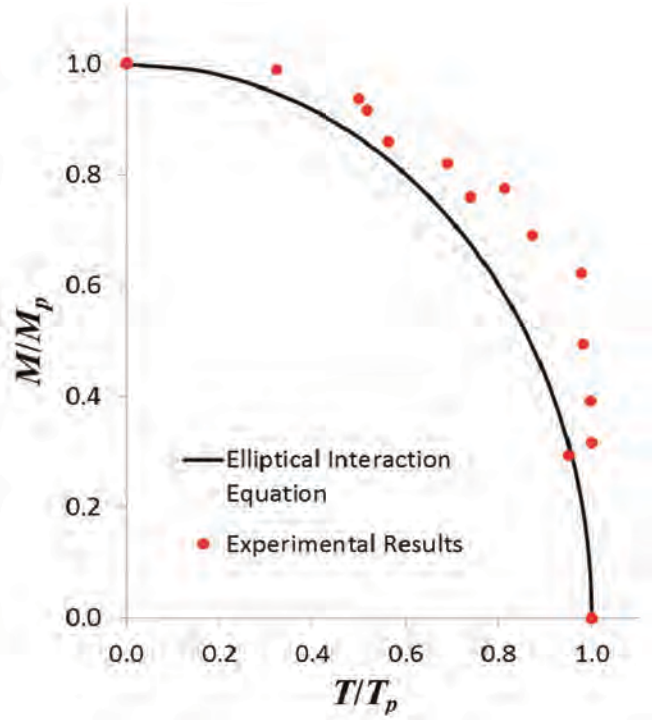

Fig. 14. Combined bending and torsion.

DESIGN EXAMPLE

In the vertical brace connection shown in Figure 15, the gusset yielding strength at the gusset-to-beam interface will be checked against the following loads, which were calculated with the uniform force method. The plate is ¾ in. thick and the material is ASTM A36.

LRFD	ASD
$H_b = 562$ kips $V_b = 64.0$ kips $M_b = 4{,}590$ kip-in.	$H_b = 375$ kips $V_b = 42.7$ kips $M_b = 3{,}060$ kip-in.

Because only shear, moment and axial loads are present, Equation 67 reduces to

$$\frac{M_r}{M_p}+\left(\frac{P_r}{P_y}\right)^2+\left(\frac{V_r}{V_p}\right)^4=1.0$$

For design, the interaction equations are

LRFD	ASD
$\frac{M_r}{\phi_b M_n}+\left(\frac{P_r}{\phi_t P_n}\right)^2+\left(\frac{V_r}{\phi_v V_n}\right)^4 \le 1.0$	$\frac{\Omega_b M_r}{M_n}+\left(\frac{\Omega_t P_r}{P_n}\right)^2+\left(\frac{\Omega_v V_r}{V_n}\right)^4 \le 1.0$

The flexural strength is calculated with AISC *Specification* Equation F11-1:

$$Z=\frac{(0.75\text{ in.})(47\text{ in.})^2}{4}$$
$$=414\text{ in.}^3$$

$$M_n = F_y Z$$
$$=(36\text{ ksi})(414\text{ in.}^3)$$
$$=14{,}900\text{ kip-in.}$$

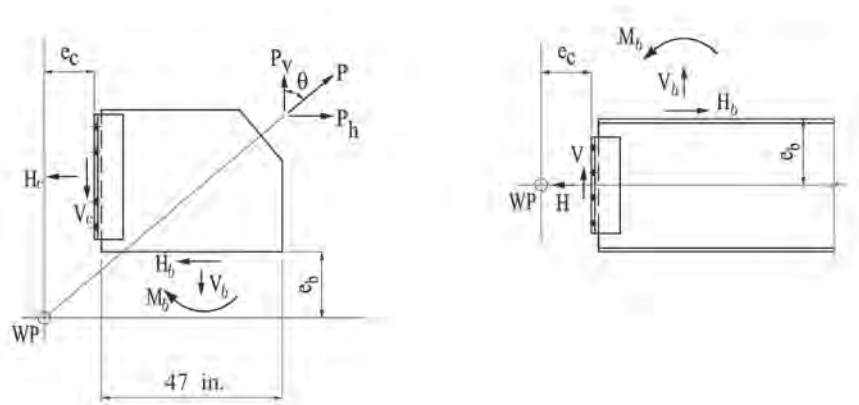

Fig. 15. Vertical brace connection.

LRFD	ASD
$\phi_t P_n = (0.9)(14{,}900 \text{ kip-in.})$ $= 13{,}400 \text{ kip-in.}$	$\frac{P_n}{\Omega_t} = \frac{14{,}900 \text{ kip-in.}}{1.67}$ $= 8{,}920 \text{ kip-in.}$

The tension yielding strength per AISC *Specification* Equation J4-1 is

$$P_n = F_y A_g$$
$$= (36 \text{ ksi})(0.75 \text{ in.})(47 \text{ in.})$$
$$= 1{,}270 \text{ kips}$$

LRFD	ASD
$\phi_t P_n = (0.9)(1{,}270 \text{ kips})$ $= 1{,}140 \text{ kips}$	$\frac{P_n}{t} = \frac{1{,}270 \text{ kips}}{1.67}$ $= 760 \text{ kips}$

The shear strength per AISC *Specification* Equation J4-3 is

$$V_n = 0.60 F_y A_{gv}$$
$$= (0.6)(36 \text{ ksi})(0.75 \text{ in.})(47 \text{ in.})$$
$$= 761 \text{ kips}$$

LRFD	ASD
$\phi_v V_n = (1.0)(761 \text{ kips})$ $= 761 \text{ kips}$	$\frac{V_n}{\Omega_v} = \frac{761 \text{ kips}}{1.50}$ $= 507 \text{ kips}$

Using the interaction equations,

LRFD	ASD
$\frac{4{,}590 \text{ kip-in.}}{13{,}400 \text{ kip-in.}} + \left(\frac{64.0 \text{ kips}}{1{,}140 \text{ kips}}\right)^2 + \left(\frac{562 \text{ kips}}{761 \text{ kips}}\right)^4$ $= 0.643 < 1.0$ **o.k.**	$\frac{3{,}060 \text{ kip-in.}}{8{,}920 \text{ kip-in.}} + \left(\frac{42.7 \text{ kips}}{760 \text{ kips}}\right)^2 + \left(\frac{375 \text{ kips}}{507 \text{ kips}}\right)^4$ $= 0.646 < 1.0$ **o.k.**

Therefore, the gusset-to-beam interface is adequate for the limit state of gusset plate yielding.

SYMBOLS

A = cross-sectional area, in.^{2}

F_y = specified minimum yield strength, ksi

G = shear modulus of elasticity = 11,200 ksi

I = moment of inertia, in.^{4}

J = torsional constant, in^4

L = length of the member, in.

M = bending moment, in.-kips

M_p = plastic bending moment, in.-kips

M_{px} = plastic bending moment about the x-axis, in.-kips

M_{pz} = plastic bending moment about the z-axis, in.-kips

M_{rx} = required x-axis bending moment, in.-kips

M_{rz} = required z-axis bending moment, in.-kips

M_x = bending moment about the x-axis, in.-kips

M_z = bending moment about the z-axis, in.-kips

P = axial force, kips

P_n = nominal axial strength, kips

P_r = required axial force, kips

Q = first moment of area, in.^{3}

S = gross section modulus, in.^{3}

T = torsional moment, in-kips

T_p = plastic torsional moment, in.-kips

T_r = required torsional moment, in.-kips

V = shear force, kips

V_r = required shear force, kips

V_{rx} = required x-axis shear force, in.-kips

V_{rz} = required z-axis shear force, in.-kips

a = plate dimension as shown in Figure 2a, in.

b = width of the central region of the cross-section resisting the shear force, in.

c = distance to outermost fiber, in.

d = depth of the member, in.

h = depth of the central region of the cross-section resisting the shear force, in.

h = depth of the central region of the cross-section resisting the axial force, in.

t = thickness of the member, in.

x = distance along the length of the member, in.

η = strain hardening modulus for pure shear

τ = shear stress, ksi

θ = angle of twist

θ = flexural rotation

θ_y = yield rotation

σ = normal stress, ksi

σ_e = effective stress, ksi

σ_x = normal stress in the x-direction, ksi

σ_y = tension yield stress, ksi

σ_z = normal stress in the z-direction, ksi

REFERENCES

AISC (2010), *Specification for Structural Steel Buildings*, American Institute of Steel Construction, Chicago, IL.

Ahmed, S.R., Idris, A.B.M. and Uddin, M.W. (1996), "Numerical Solution of Both Ends Fixed Deep Beams," *Computers and Structures*, Vol. 61, No. 1, pp. 21–29.

Astaneh, A. (1992), "Cyclic Behavior of Gusset Plate Connections in V-Braced Steel Frames," *Stability and Ductility of Steel Structures under Cyclic Loading*, Fukomoto, Y. and Lee, G. C., eds., CRC Press, Ann Arbor, MI, pp. 63–84.

Astaneh, A. (1998), "Seismic Behavior and Design of Gusset Plates," *Steel Tips*, Structural Steel Educational Council, December.

Balaz, I. and Kolekova, Y. (2002), "Warping," *Stability and Ductility of Steel Structures*, *Proceedings*, Otto Halasz Memorial Session, Ivanyi, M. and Akademiai Kiado, eds., Budapest.

Barry, J.E. and Ainso, H. (1983), "Single-Span Deep Beams," *Journal of Structural Engineering*, ASCE, Vol. 109, No. 3, pp. 646–663.

Billinghurst, A., Williams, J.R.L., Chen, G. and Trahair, N.S. (1992), "Inelastic Torsion of Steel Members," *Computers and Structures*, Vol. 42, No. 6, pp. 887–894.

Broude, B.M. (1953), *The Limit States of Steel Girders*, Moscow/Leningrad (in Russian).

Calladine, C.R. (1969), *Engineering Plasticity*, Pergamon Press, Oxford, United Kingdom.

Chakrabarty, J. (2006), *Theory of Plasticity*, 3rd ed., Elsevier.

Chen, W.F. and Atsuta, T. (1977), *Theory of Beam-Columns, Volume 2, Space Behavior and Design*, McGraw-Hill, New York, NY.

Chen, W.F. and Han, D.J. (2007), *Plasticity for Structural Engineers*, J. Ross Publishing, Plantation, FL.

Cook, R.D. and Young, W.C. (1985), *Advanced Mechanics of Materials*, Macmillan Publishing Company, New York, NY.

Drucker, D.C. (1956), "The Effect of Shear on the Plastic Bending of Beams," *Journal of Applied Mechanics*, December, pp. 509–514.

Duan, L. and Chen, W.F. (1989), "Design Interaction Equation for Steel Beam-Columns," *Journal of Structural Engineering*, ASCE, Vol. 115, No. 5, pp. 1225–1243.

Freudenthal, A.M. (1950), *The Inelastic Behavior of Engineering Materials and Structures*, John Wiley and Sons, New York, NY.

Galambos, T.V. and Surovek, A.E. (2008), *Structural Stability of Steel*, John Wiley and Sons, New York, NY.

Gill, S.S. and Boucher, J.K.G. (1964), "An Experimental Investigation of Plastic Collapse of Structural Members under Combined Bending and Torsion," *The Structural Engineer*, Vol. 42, No. 12, pp. 423–428.

Goodrich, W. (2005), *Behavior of Extended Shear Tabs in Stiffened Beam-to-Column Connections*, Master's Thesis, Vanderbilt University.

Gregory, M. (1960), "The Bending and Shortening Effect of Pure Torque," *Australian Journal of Applied Science*, March, pp. 209–216.

Hardin, B.O. (1958), "Experimental Investigation of the Primary Stress Distribution in the Gusset Plates of a Double Plane Pratt Truss Joint with Chord Splice at the Joint," University of Kentucky Engineering Experiment Station, Bulletin No. 49, September.

Harrison, H.B. (1963), "The Plastic Behavior of Mild Steel Beams of Rectangular Section Bent About Both Principal Axes," *The Structural Engineer*, Vol. 41, No. 7, pp. 231–237.

Hill, R. and Siebel, M.P.L. (1953), "On the Plastic Distortion of Solid Bars by Combined Bending and Twisting," *Journal of the Mechanics and Physics of Solids*, Vol. 1, pp. 207–214.

Horne, M.R. (1951), "The Plastic Theory of Bending of Mild Steel Beams with Particular Reference to the Effect of Shear Forces," *Proceedings of the Royal Society of London, Series A, Mathematical and Physical Sciences*, Vol. 207, No. 1089, pp. 216–228.

Irvan, W.G. (1957), "Experimental Study of Primary Stresses in Gusset Plates of a Double Plane Pratt Truss," University of Kentucky Engineering Research Station, Bulletin No. 46, December.

Jensen, C.D. and Crispen, R.E. (1938), "Stress Distribution in Welds Subject to Bending," *Welding Research Supplement*, American Welding Society, October.

Johnson, W., Chitkara, N.R. and Ranshi, A.S. (1974), "Plane-Stress Yielding of Cantilevers in Bending Due to Combined Shear and Axial Load," *Journal of Strain Analysis*, Vol. 9, No. 2, pp. 67–77.

Karr, P.H. (1956), "Stresses in Centrally Loaded Deep Beams," *SESA Proceedings*, Vol. XV, No. 1, Society for Experimental Stress Analysis, pp. 77–84.

Lavis, C.S. (1967), *Computer Analysis of the Stresses in a Gusset Plate*, Master's Thesis, University of Washington.

May, I.M. and Al-Shaarbaf, I.A.S. (1989), "Elasto-Plastic Analysis of Torsion Using a Three-Dimensional Finite Element Model," *Computers and Structures*, Vol. 33, No. 3, pp. 667-678.

Metzger, K.A.B. (2006), "Experimental Verification of a New Single Plate Shear Connection Design Model," Master's Thesis, Virginia Polytechnic Institute, May 4.

Mohr, B.A. and Murray, T.M. (2008), "Bending Strength of Steel Bracket and Splice Plates," *Engineering Journal*, AISC, Vol. 45, No. 2, pp. 97–106.

Moore, D.B. and Owens, G.W. (1992), "Verification of Design Methods for Finplate Connections," *The Structural Engineer,* Vol. 70, No. 3/4, February.

Morris, G.A. and Fenves, S.J. (1969), "Approximate Yield Surface Equations," *Journal of the Engineering Mechanics Division*, ASCE, Vol. 95, No. EM4, pp. 937–954.

Mrazik, A., Skaloud, M. and Tochacek, M. (1987), *Plastic Design of Steel Structures*, Ellis Horwood Series, Engineering Science, Halsted Press, New York, NY.

Nadai, A. (1950), *Theory of Flow and Fracture of Solids*, McGraw-Hill, New York, NY.

Neal, B. G. (1961), "The Effect of Shear and Normal Forces on the Fully Plastic Moment of a Beam of Rectangular Cross Section," *Journal of Applied Mechanics*, Vol. 28, pp. 269–274.

Neal, B.G. (1963), *The Plastic Methods of Structural Analysis*, 2nd ed., John Wiley and Sons, New York, NY.

Ocel, J.M. (2013), "Guidelines for the Load and Resistance Factor Design and Rating of Riveted and Bolted Gusset-Plate Connections for Steel Bridges," Contractor's Final Report for NCHRP Project 12-84, National Cooperative Highway Research Program, February.

Paltchevskiy, S.A. (1948), *Determination of Load-Carrying Capacity of Steel Bars for Some Cases of Complex State of Stress* (in Russian).

Patrick, M., Thomas, I.R. and Bennets, I.D. (1986), "Testing of Web Side Plate Connection," *Proceedings of the Pacific Structural Steel Conference*, Vol. 2, New Zealand Heavy Engineering Research Association, pp. 95–116.

Perna, F.J. (1941), "Photoelastic Stress Analysis, with Special Reference to Stresses in Gusset Plates," Master's Thesis, University of Tennessee.

Rust, T.H. (1938), "Specification and Design of Steel Gussett-Plates," *Proceedings,* ASCE, November, pp. 142–167.

Sanatthadaporn, S. and Chen, W.F. (1970), "Interaction Curves for Sections Under Combined Biaxial Bending and Axial Force," WRC Bulletin No. 148, Welding Research Council, New York, pp. 1–11.

Sandel, J.A. (1950), *Photoelastic Analysis of Gusset Plates*, Masters Thesis, University of Tennessee, December.

Schreiner, N.G. (1935), "Behavior of Fillet Welds When Subjected to Bending Stresses," *Welding Journal*, American Welding Society, September.

Seaburg, P.A. and Carter, C.J. (1997), *Torsional Analysis of Structural Steel Members*, Design Guide 9, American Institute of Steel Construction, Chicago, IL.

Seely, F.B. and Putnam, W.K. (1919), "The Relation Between the Elastic Strengths of Steel in Tension, Compression and Shear," Bulletin No. 115, Engineering Experiment Station, Vol. 17, No. 11, University of Illinois, November 10.

Seely, F.B. and Smith, J.O. (1952), *Advanced Mechanics of Materials*, John Wiley and Sons, New York, NY.

Shawki, S. and Hendry, A.W. (1961), "Stresses in a Deep Beam with a Central Concentrated Load," *Experimental Mechanics*, June, pp. 192–198.

Sheridan, M.L. (1953), "An Experimental Study of the Stress and Strain Distribution in Steel Gusset Plates," Ph.D. Dissertation, University of Michigan, Ann Arbor, MI.

Sherman, D.R. and Ghorbanpoor, A. (2002), "Design of Extended Shear Tabs," Final Report, American Institute of Steel Construction, Chicago, IL, October.

Shunsuke, B. and Kajita, T. (1982), "Plastic Analysis of Torsion of a Prismatic Beam," *International Journal for Numerical Methods in Engineering*, Vol. 18, pp. 927–944.

Sidebottom, O.M. and Clark, M.E. (1958), "Theoretical and Experimental Analysis of Members Loaded Eccentrically and Inelastically," Engineering Experiment Station, Bulletin No. 447, University of Illinois, March.

Smith, J.O. and Sidebottom, O.M. (1965), *Inelastic Behavior of Load-Carrying Members*, John Wiley and Sons, New York, NY.

Steele, M.C. (1954), "The Plastic Bending and Twisting of Square Section Members," *Journal of the Mechanics and Physics of Solids*, Vol. 3, pp. 156–166.

Struik, J.H.A. (1972), "Applications of Finite Element Analysis to Non-linear Plane Stress Problems, Ph.D. Dissertation, Lehigh University.

Vasarhelyi, D.D. (1971), "Tests of Gusset Plate Models." *Journal of the Structural Division,* ASCE Vol. 97, No. fST2, pp. 665–679.

Vrouwenvelder, A.C.W.M. (2003), *The Plastic Behavior and the Calculation of Beams and Frames Subjected to Bending*, Technical University Delft, March.

White, D.W., Leon, R.T., Kim, Y.D., Mentes, Y. and Bhuiyan, M.T.R. (2013), "Finite Element Simulation and Assessment of the Strength Behavior of Rivited and Bolted Gusset-Plate Connections in Steel Truss Bridges," Final Report Prepared for Federal Highway Administration and NCHRP Transportation Research Board of the National Academies, March.

Whitmore, R.E. (1952), "Experimental Investigation of Stresses in Gusset Plates," University of Tennessee Engineering Experiment Station, Bulletin No. 16, May.

Wyss, T. (1923), "Die Kraftfelder in Festen Elastischen Korpern und ihre Praktischen Anwendungen," Berlin, Germany.

Behavior and Response of Headed Stud Connectors in Composite Steel Plate Girder Bridges under Cyclic Lateral Deformations

HAMID BAHRAMI, ERIC V. MONZON, AHMAD M. ITANI and IAN G. BUCKLE

ABSTRACT

Most of the mass of steel plate girder bridge superstructures is concentrated in the reinforced concrete deck. During a seismic event, the inertia force that is generated in the reinforced concrete deck is transferred to the support cross frames through the headed stud connectors. Seismic analyses showed that these connectors are subjected to combined axial tension and shear forces. If not designed properly, these connectors may fail prematurely during an earthquake, altering the load path and subjecting other bridge components to forces they are not designed for. To verify these observations, two half-scale models of plate girder bridge subassembly were constructed and subjected to cyclic testing. The two specimens represented two different configurations of headed stud connectors in transferring the deck seismic forces. The connectors in the first specimen connected the girder top flange to the reinforced concrete deck, while the connectors in the second specimen connected the cross-frame top chord to the deck. These experiments showed that the connectors were indeed vulnerable under transverse lateral loading. The failure mode of these connectors is a combination between shear and tensile forces or concrete breakout. Based on this investigation, design equations were proposed and adopted in the AASHTO LRFD Bridge Design Specifications to evaluate the resistance of such connectors under shear and tensile forces.

Keywords: stud connectors, seismic design, steel plate girders, reinforced concrete deck, steel girder bridge.

INTRODUCTION

Composite steel plate girder bridge superstructures have experienced various degrees of damage during recent earthquakes. This damage has occurred in plate girders, reinforced concrete decks, stud connectors, bearings, cross frames and their connections. In 1992, a series of three earthquakes with a maximum magnitude of 7.0 occurred near the town of Petrolia in northern California (Caltrans, 1992). Some notable damage was reported to the Van Duzen River Bridge, which has a steel plate girder superstructure. The support cross frames and the lateral bracing of the southbound bridge experienced buckling and yielding. In addition, the reinforced concrete deck experienced damage to the stud connectors at one of the abutments. This damage showed that the stud connectors, used to achieve a composite action between the steel plate girders and the concrete deck, were subjected to seismic forces for which they were not designed.

Earthquake loading in the lateral direction of the bridge causes transverse bending of the superstructure, resulting in seismic reactions at abutments and piers. The majority of the seismic inertia loads in steel plate girder bridges are generated in the reinforced concrete deck because it accounts for almost 80% of the superstructure weight. Carden, Itani and Buckle (2005) showed that the stud connectors between the deck and girders are among the critical components in the seismic transverse load path. However, very limited research is available on the response and the resistance of these connectors in transferring these seismic forces. With the absence of such critical information, it is commonly assumed that the stud connectors, designed for strength and fatigue, are adequate for seismic forces. The observed damage, however, raised concerns about the adequacy of these connectors in transferring the seismic forces to the supports and showed the need to better understand their response under seismic loading.

Most of the research conducted on stud connectors was to investigate the composite action between steel girders and reinforced concrete deck. Ollgaard, Slutter and Fisher (1971), Oehlers and Johnson (1987), Lloyd and Wright (1990) and Oehlers (1995) have studied the shear resistance of connectors in composite beams. Hawkins and Mitchell (1984), Gattesco and Giuriani (1996), and Seracino, Oehlers

Hamid Bahrami, Former Doctoral Student, Department of Civil and Environmental Engineering, University of Nevada, Reno, NV 89557

Eric V. Monzon, Assistant Professor, Department of Civil Engineering, West Virginia University—Institute of Technology, Montgomery, WV (corresponding author). Email: evmonzon@gmail.com

Ahmad M. Itani, Professor, Department of Civil and Environmental Engineering, University of Nevada, Reno, NV. Email: itani@unr.edu

Ian G. Buckle, Professor, Department of Civil and Environmental Engineering, University of Nevada, Reno, NV. Email: igbuckle@unr.edu

Paper No. 2013-28

and Yeo (2003) reported strength and stiffness degradation in the concrete around the connectors due to unidirectional cyclic loadings. McMullin and Astaneh-Asl (1994) recommended a cone be placed around connectors to create ductile response and to avoid brittle fracture. Mouras et al. (2008) investigated the axial resistance of the stud connector under static and dynamic loading. They showed experimentally that the limiting factor in transferring the in-plane moment capacity of a reinforced concrete deck is the axial resistance of connectors. They have also shown that the standard haunch detail in steel plate girders lowers the tensile resistance of stud connector and offers limited ductility because that zone is not adequately reinforced.

SEISMIC DEMAND ON STUD CONNECTORS IN A COMPOSITE-PLATE GIRDER BRIDGE

A 3D finite element model of a steel plate girder superstructure was developed to determine the forces on stud connectors under seismic loading. The geometry of this superstructure was taken from a bridge designed by Caltrans engineers and used in their Bridge Design Practice for training purposes (Caltrans, 2007). The composite steel plate girder bridge consists of three continuous spans. The total length of the bridge is 385 ft, with span lengths of 110, 165 and 110 ft. The total width of the bridge is 58 ft, which consists of five steel plate girders spaced at 12 ft. The reinforced concrete deck is 9⅛ in. thick. All intermediate cross frames are spaced at 27.5 ft and consist of chevron-bracing members with single L4×4×5⁄16 sections connected to the bottom chord of double L6×6×½. The support cross frames have an X-pattern using single L4×4×½ sections that are interconnected at their midlength where the diagonals cross. Stud connectors were used throughout the length of the bridge. These connectors were designed for strength and fatigue according to the AASHTO LRFD Bridge Design Specifications (AASHTO, 2008). At the positive moment regions, three ⅞-in.-diameter, single-headed stud connectors spaced at 15 in. were used on top of each girder. In the negative moment region, the connectors were spaced at 24 in. The transverse spacing between the connectors is 3 in. Elastomeric bearings with transverse shear keys were used at the abutment and at the piers.

The SAP2000 computer program was used in the analytical investigation (CSI, 2010). The steel girders, stiffeners and decks were modeled using shell elements, while the intermediate and support cross frames were modeled using frame elements. The support cross frames were modeled using nonlinear link elements with multilinear plastic Takeda hysteretic properties. Vertical and rotational springs were used at the supports to model the vertical and rotational stiffness of the elastomeric bearings. The elastomeric bearing stiffness properties that were included in the analytical model are shown in Table 1. The stud connectors were modeled using linear link elements. Their stiffnesses were calculated based on the equations proposed by Carden et al. (2005). For each stud connector, the lateral and axial stiffnesses are equal to 500 kip/in. and 1000 kip/in., respectively. The overall view of the SAP2000 model is shown in Figure 1. It is assumed in the model that the substructure is rigid because the purpose of this analysis is to determine the distribution of seismic forces among the shear connectors. Although the substructure flexibility affects the global seismic response, it does not affect the lateral load path in the superstructure.

The total seismic weight of the superstructure is 3407 kips. Dead load analysis showed that each abutments carries 331 kips, while the intermediate supports carry 1372 kips each. Table 2 shows the periods and modal participating mass ratios of the first nine modes from modal. The longitudinal and transverse directions correspond to the global *x*- and global *y*-direction in the model.

The seismic demands on the reinforced concrete deck and the stud connectors were determined using nonlinear pushover analysis.

The pushover analysis was performed using a mode 5 load pattern because it was the dominant transverse mode, with 79% mass participation in that direction, as shown in Table 2. The deformed shape of the girders is shown in Figure 2. Figure 3 shows the vertical deformation contours of the reinforced concrete deck, which clearly indicates a torsional rotation of the superstructure about its longitudinal axis. This implies that the stud connectors are subjected to axial forces in addition to shear forces in order to maintain deformation compatibility between the reinforced concrete deck and the steel plate girders.

Figure 4 shows the schematic view of the stud connectors on the top flange of the plate girders. Connector 2 is the middle connector and is located along the plane of girder web while connectors 1 and 3 are the exterior connectors. The seismic force demands on the stud connectors from the nonlinear response history analysis are shown in Figure 5. In this figure, *P* represents axial force in the connectors, *VL* is the shear force in longitudinal direction and *VT* is the shear force in transverse direction. The numbers that follow the aforementioned letters refer to the connector number. Figure 5a shows the axial force distribution in each of the connectors on girder 1 along the length of the bridge superstructure at 5% drift (drift is ratio of relative girder displacement to the girder height). This plot shows that the transverse seismic force creates large axial force demands on the connectors directly over the supports (abutments and bents). The middle connector shows minimal axial force while the connectors on either side are subject to equal and opposing axial forces. Figure 5b shows the longitudinal shear force distribution in the connectors in girder 1. The distribution indicates force transfer between the reinforced concrete deck and steel girders as the composite section resists the

Table 1. Elastomeric Bearing Properties		
Location	Vertical Stiffness (kips/in.)	Rotational Stiffness (kips-in./rad)
Abutments	3,284	64,650
Piers	6,829	225,000

Table 2. Modal Periods and Mass Participation Ratios			
Mode No.	Period (sec)	Mass Participating Ratio	
		UX (%)	UY (%)
1	4.176	100	0
2	0.384	0	0
3	0.380	0	0
4	0.208	0	0
5	0.202	0	79
6	0.186	0	3
7	0.143	0	0
8	0.113	0	15
9	0.084	0	0

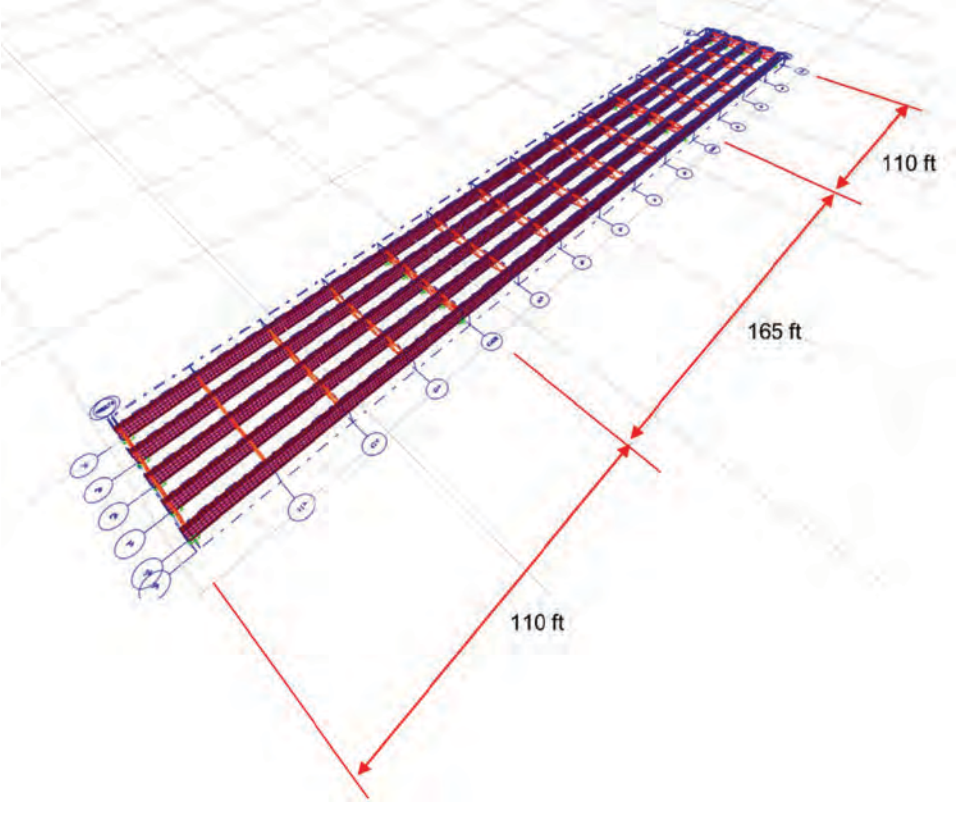

Fig. 1. Finite element model of three-span five-girder bridge (deck is not shown for clarity).

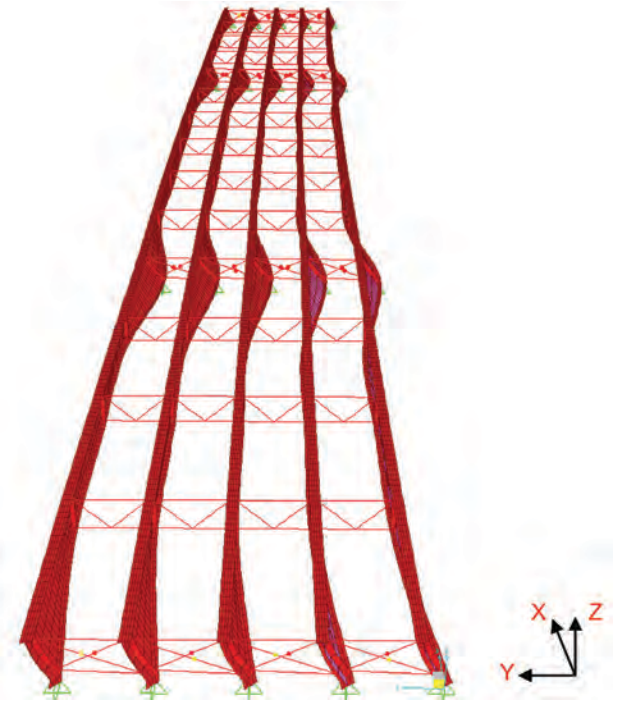

Fig. 2. Deformed shape of the superstructure (deck not shown for clarity).

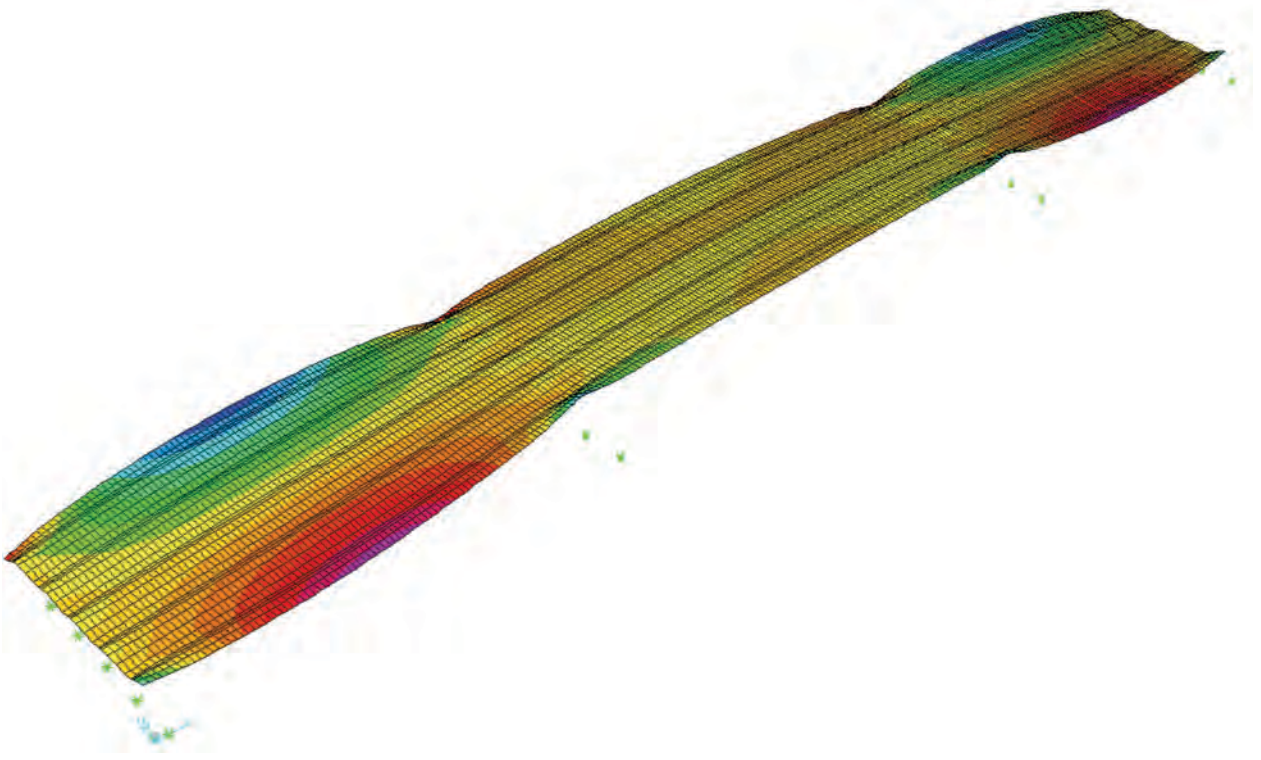

Fig. 3. Contour of deck vertical deformation during the pushover analysis.

transverse seismic forces through bending in the plane of the deck. Figure 5c shows the transverse shear force distribution in the connectors in girder 1. This distribution is the result of combined transverse shear force transfer between the reinforced concrete deck and steel girders and torsional moment on the superstructure. The torsional moment causes out-of-plane bending in deck. The bending moment results in equal and opposite transverse shear forces in the connectors on either side of the girder. These opposing forces cancel out once all the forces in a row of connectors are summed up, as shown in Figure 5d. The high peaks near the supports indicate significant force transfer between the reinforced concrete deck and steel girders. The other small peaks seen in this plot are at the location of intermediate cross frames. This shows that the intermediate cross frames attract only a small amount of the transverse seismic forces.

The significant observation from this analysis is that the stud connectors in a composite steel plate girder superstructure not only resist shear in the longitudinal direction, but also experience significant axial and transverse shear forces during a seismic event. With peaks occurring near the supports, the connection of the reinforced concrete deck via a stud connector to the top flange of the girder may be vulnerable in these regions and should be designed for the seismic forces. The large peaks in the plots for the connector forces clearly surpass the elastic range for these connectors, which indicate damage to the connection between the reinforced concrete deck and the steel plate top flange. Any nonlinearity in the connectors near the supports will lead to redistribution of the forces in the connectors in their vicinity, which in turn will translate into a damaged zone (over a certain distance) near the supports. Failure of the stud connectors at and near the supports will alter the lateral load path. The deck seismic forces will be transmitted to the stud connectors that are located at some distance from the support, which are then transferred to the girders and then to the bearings and substructure. The girders, in this situation, are subjected to bending about their weak axis, which could damage the girders.

The seismic force demands on the connectors at support locations is illustrated in Figure 6a. The axial tensile force in the connector is transferred from the reinforced concrete deck through a cone, as illustrated in Figure 6b. Based on these observations, experimental investigation was performed to better understand and verify the response of stud connectors under this complex loading.

EXPERIMENTAL INVESTIGATION

Two half-scale test specimens representing the subassembly system of reinforced concrete deck, top and bottom chords and steel girders were constructed and subjected to cyclic lateral loading. The test specimens used in the experimental program represented a 3-ft-long slice of a three-girder

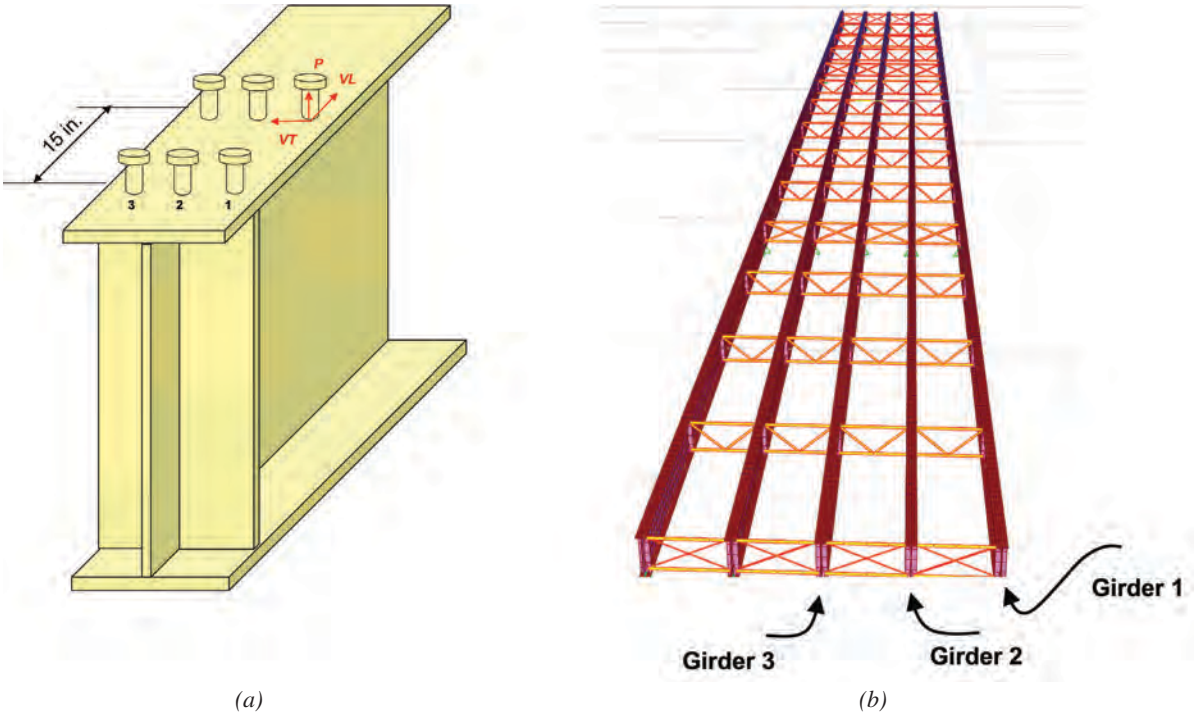

(a) *(b)*

Fig. 4. (a) Schematic view of stud connectors; (b) location of girders.

(a)

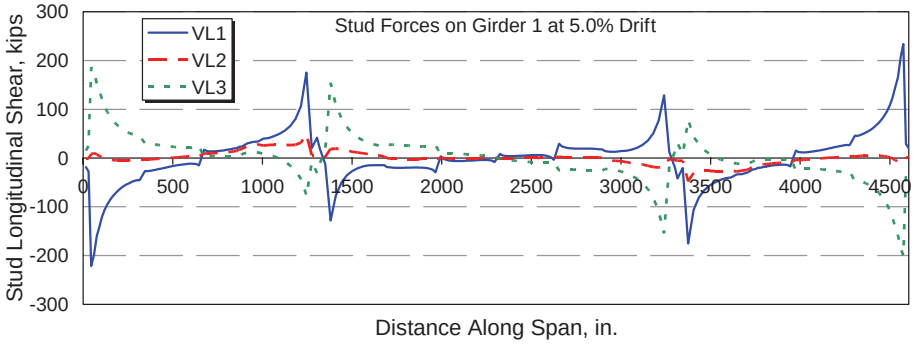

(b)

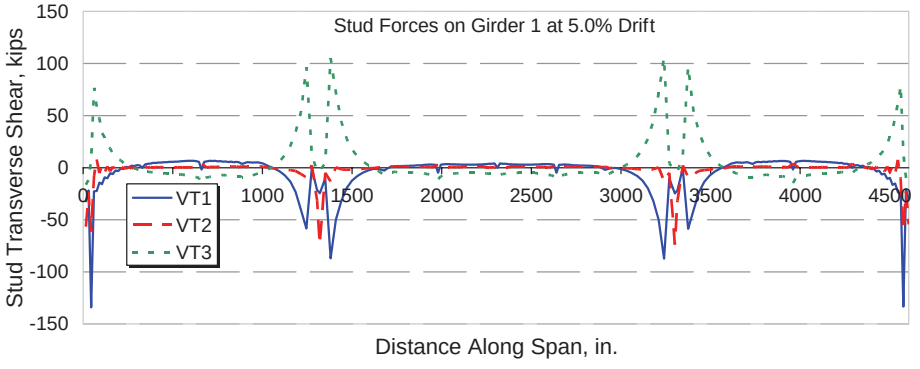

(c)

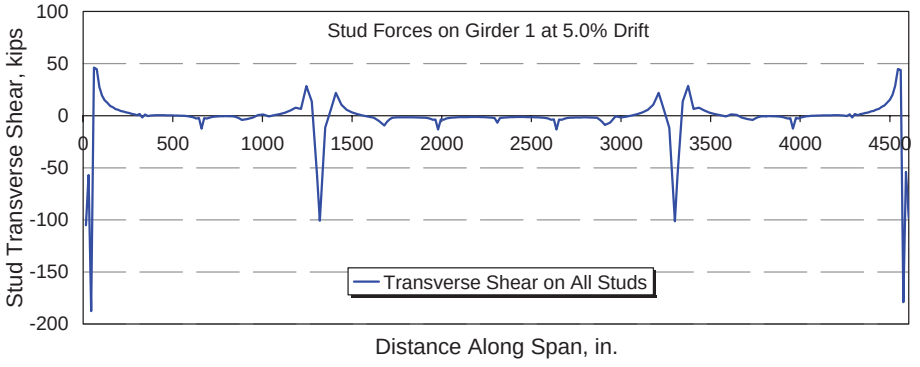

(d)

Fig. 5. Stud connector force distribution in girder 1 at 5% superstructure drift.

bridge superstructure over an intermediate bent. The overall dimensions of the specimens were scaled down to 50% from the prototype bridge cross-section discussed in the analytical program.

The test specimens represented two different configurations of transferring the deck seismic forces to the bearings and the substructures. Neither specimen had any diagonal cross frames to limit the lateral resistance to the framing action provided by the reinforced concrete deck, girders and chord members of the cross frames. Specimen F0A had the reinforced concrete deck connected to the top flanges of steel girders through headed stud connectors. Specimen F0B had the R/C deck connected to the top chord through headed stud connectors. These are the details recommended by the AASHTO Specifications to transfer the deck seismic forces to the bearings and substructures.

Test Setup

Figure 7 shows the elevation of the test setup that was designed to allow specimens to undergo lateral cyclic deformations. A hydraulic push–pull displacement-controlled actuator attached to the deck was used to apply the horizontal displacement. Both specimens were supported on ideal steel pins that allowed in-plane rotation and prevented any uplift.

Figure 8 is a photo of the test setup with specimen F0A where the test specimen, load cells, lateral support frames, actuator and the reaction blocks are shown. Lateral support frames were constructed around the specimens to prevent out-of-plane movement. Figure 9 shows the kinematic of the test setup for specimen F0A. As shown in this figure, the lateral displacement on the specimen produces double-curvature behavior in the top and bottom chords as well as rotational displacement demand at the studded joints over the girders top flanges.

Test Specimens

The width of the subassembly was 3 ft. The girders were spaced at 6 ft on centers, and the deck overhangs were 2.5 ft. The reinforced concrete deck was 4.5 in. thick with a haunch

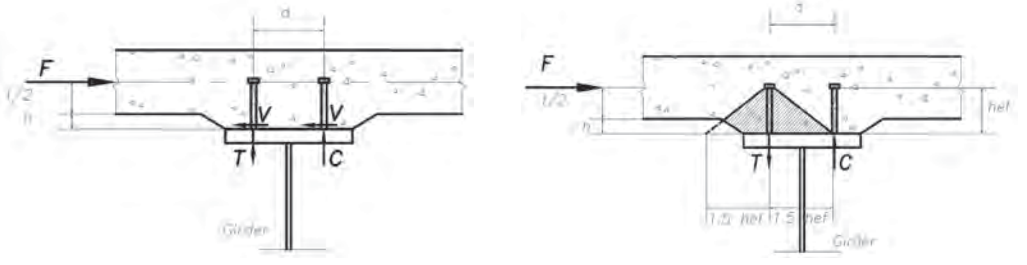

(a) (b)

Fig. 6. (a) Seismic demands on stud connectors at supports; (b) concrete pull-out zone on the connector.

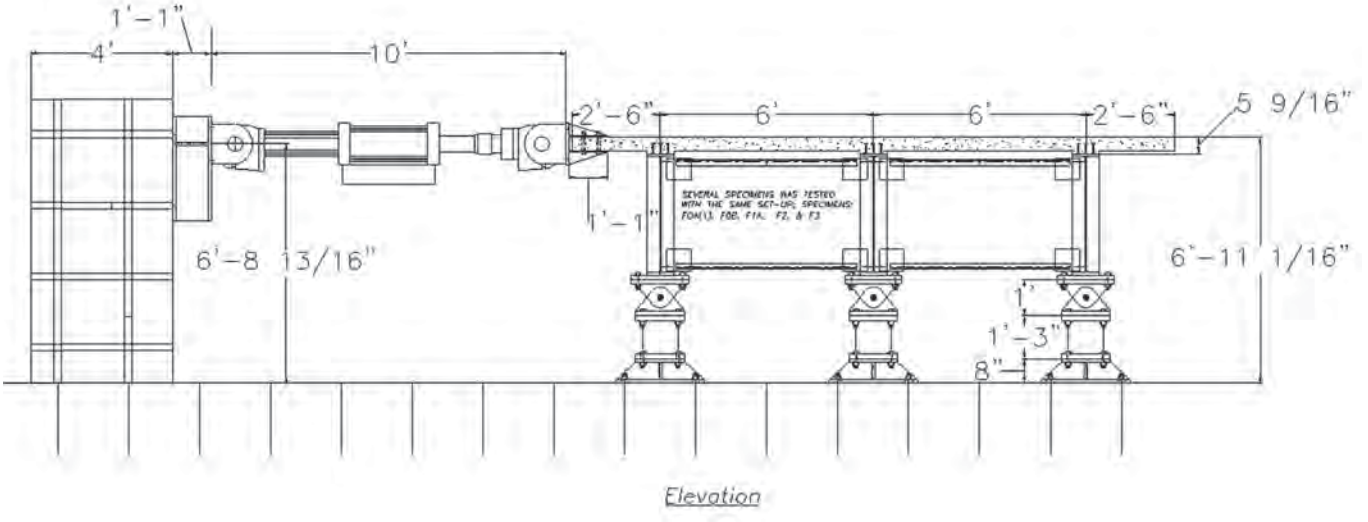

Fig. 7. Elevation and dimensions of test setup of specimen F0A.

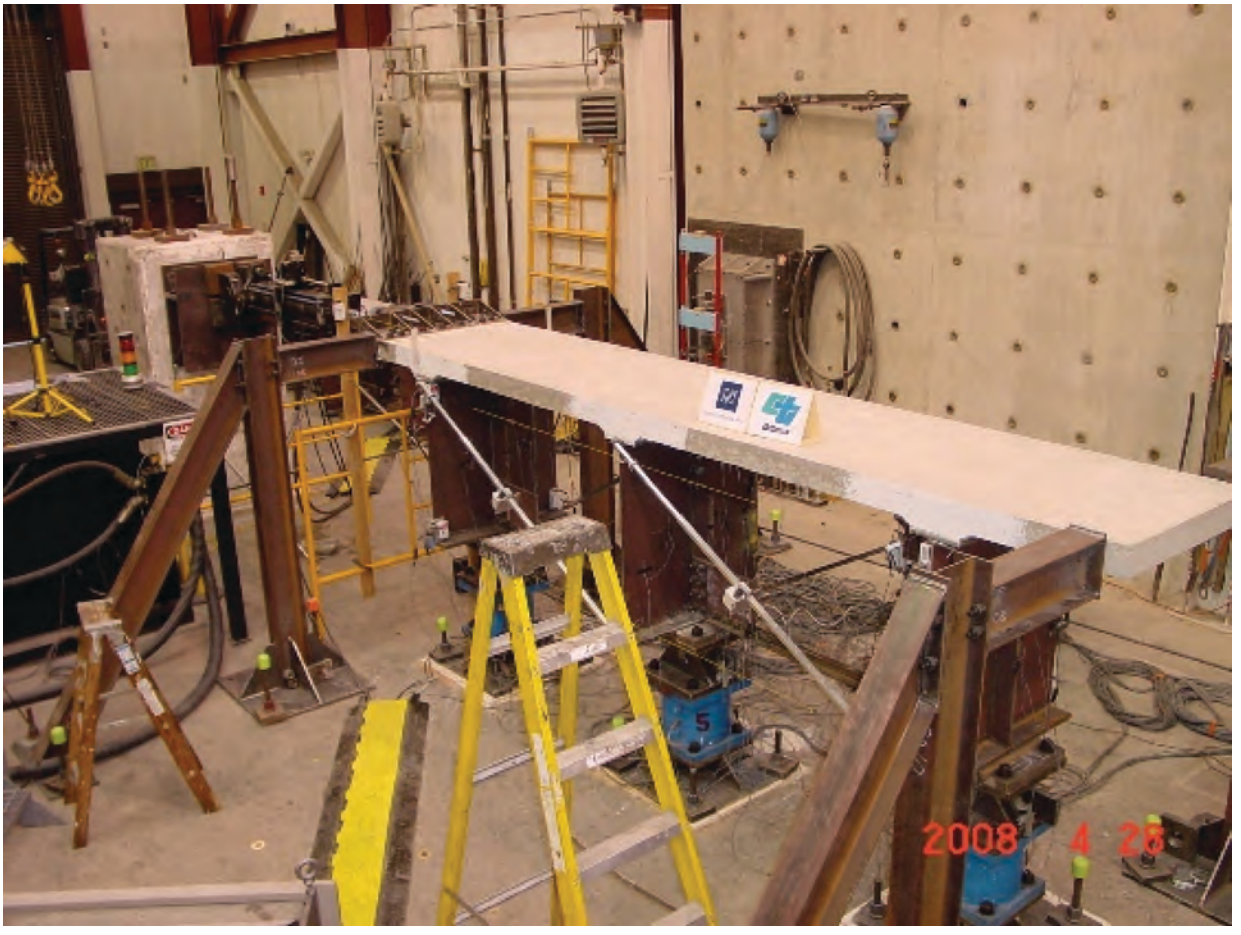

Fig. 8. Test setup inside the laboratory.

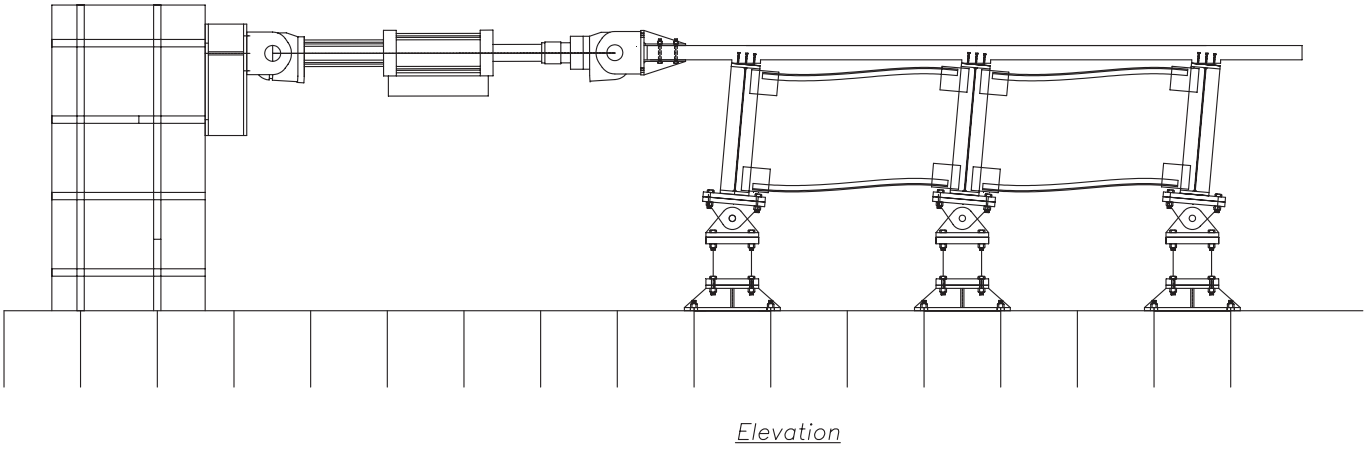

Fig. 9. Kinematics of the test setup for specimen F0A.

of 1.06 in. The deck longitudinal reinforcements were #3 at 8 in. and the transverse reinforcements were #3 at 5.5 in. The measured concrete strength was 4.0 ksi. The plate girders were built-up sections of 1-in.-thick by 9-in. flange plates and 5⁄16-in.-thick by 39-in. web plates. The bearing stiffener plates were 7⁄8 in. thick and 5 5⁄8 in. wide. The north, middle, and south girders of specimens and their corresponding reactions in the subassembly specimens are called girder 1, girder 2, and girder 3, respectively.

Specimen F0A

Figure 10 shows the dimensions and details of specimen F0A. The required number of stud connectors was calculated based on the AASHTO LRFD Bridge Design Specifications (AASHTO, 2008) using the shear capacity equations. The connectors used in the specimen were single-headed studs with a diameter of 3⁄8 in. and a total length of 3 3⁄16 in. The measured ultimate strength of the connectors was 80 ksi. The shear capacity of each connector was 6.6 kips, based on the AASHTO Specifications, using the actual strength of concrete and stud connectors. On each girder flange, over the bearing stiffeners or along the specimen centerline, three connectors spaced at 2¾ in. were provided. There were three connectors each row, and the spacing between each connector was 2½ in. Additional rows of connectors were also provided at a distance 12 in. from the specimen centerline. Thus, the total shear resistance of the stud connectors was equal to 297 kips.

Specimen F0B

Figure 11 shows the details and dimensions of specimen F0B. As shown in Figure 11, the reinforced concrete deck dropped to the elevation of the top chords. The thickness of the deck in this region was 7 7⁄16 in. with a width of 12 in. The longitudinal reinforcements in this region were #3 bars spaced at 8 in., while the transverse reinforcements were #3 spaced at 5.5 in. In this specimen, no stud connectors were provided on the top flanges near the specimen centerline. The connectors were placed on the double-angle top chord, as shown in Figure 11. On each angle, 7 connectors spaced at 6 in. were provided; thus a total of 14 connectors connect the top chord to the reinforced concrete deck. Additional rows of connectors were also provided on the girder top flange at a distance 12 in. from the specimen centerline. Thus, the lateral resistance of the stud connectors was equal to 304 kips, based on the AASHTO Specifications and using the actual strength of concrete and connectors.

Loading Sequence

A displacement-controlled loading sequence was used for all experiments. This loading was adapted from the loading history for qualifying cyclic tests of buckling restrained braces as specified in Appendix T of the AISC *Seismic Provisions* (AISC, 2005). The specimen was subjected to two cycles at every specified drift level, as shown in Figure 12. The drift level was calculated based on the differential lateral displacement between the top and bottom flanges of the steel plate girders. Because the actuator force was applied at

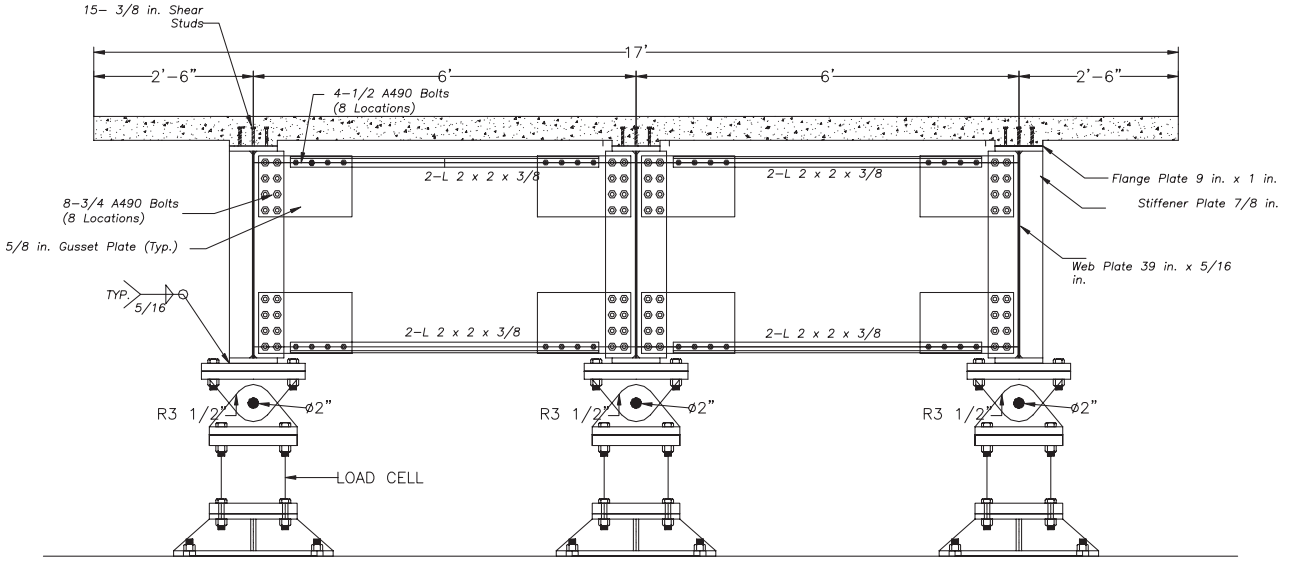

Fig. 10. Details of specimen F0A.

the deck level, the displacements that were measured from one of the diagonal displacement transducers were used to calculate the drift levels and fed into the actuator control program.

Cyclic Response of Specimen F0A

Figure 13 shows the lateral cyclic load-displacement response of the specimen in terms of total force versus the differential transverse displacement between the top and bottom flanges of the plate girders. The test showed that the ultimate, lateral load-carrying capacity of the specimen was 30 kips, and the lateral drift capacity was 6%. The elastic lateral stiffness of the specimens was 74 kips/in. The hysteresis loops show good energy dissipation capability. This is the result of the formation of plastic moment hinges at the ends of the top and bottom chords, which in turn was due to the framing action among the girders, reinforced concrete deck and chord members.

Experimental Observations

Flexural transverse cracks were developed across the deck near the girders at 1.5% drift. At 2% drift, a diagonal crack developed across the thickness of the concrete over girder 2, and the deck started to lift off from the top of the flange in this region. Further examination of the specimen after the test indicated that the concrete had failed in tension

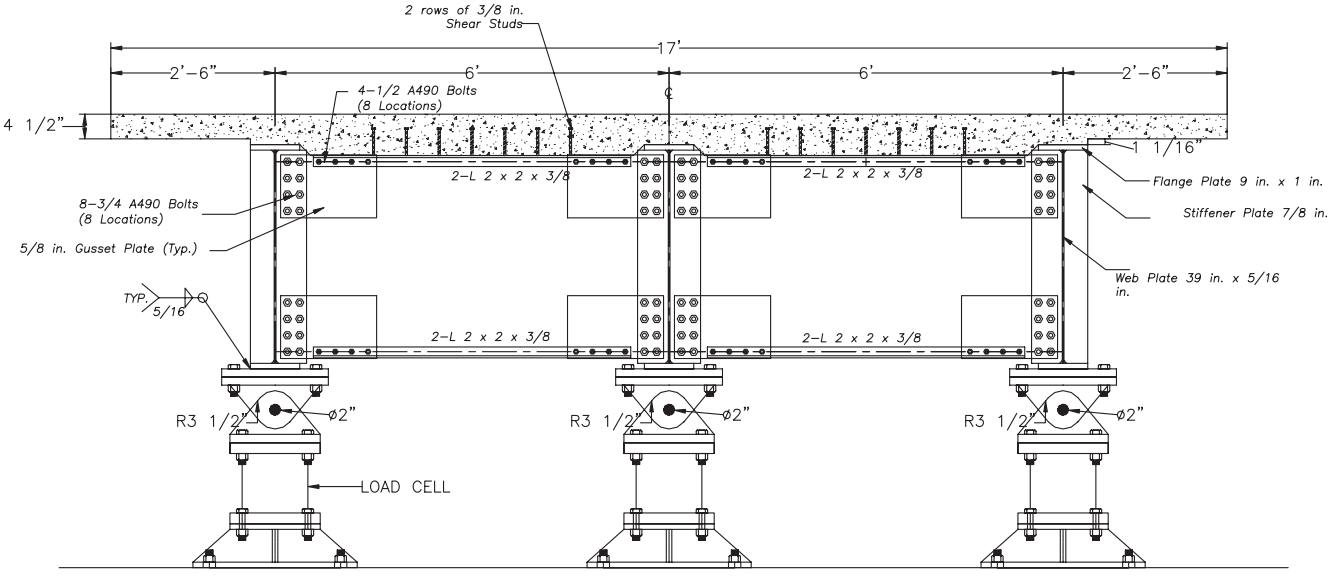

Fig. 11. Details of specimen F0B.

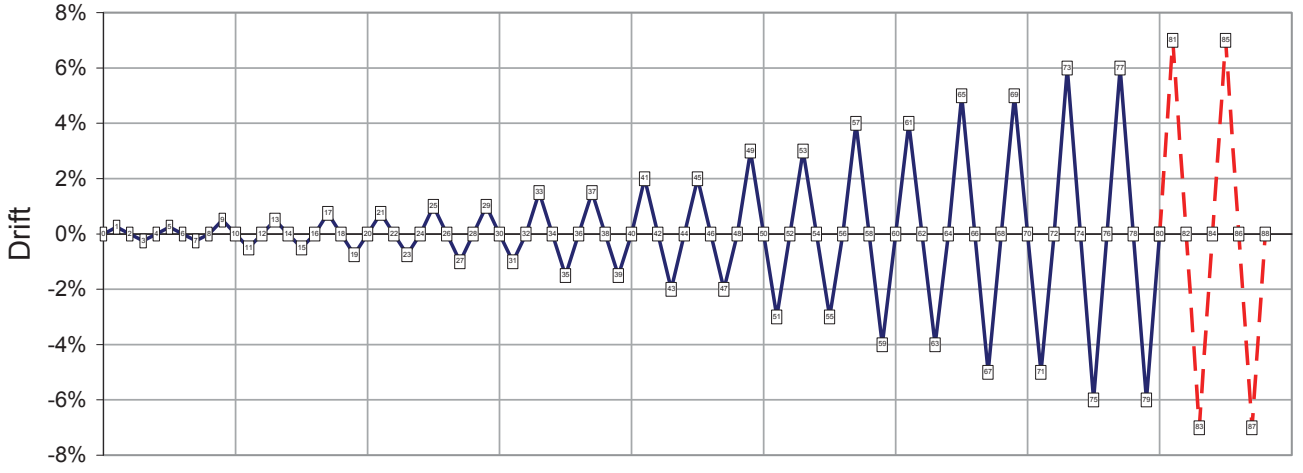

Fig. 12. Displacement-controlled loading sequence.

before the ultimate tensile strength of the stud connectors was reached. None of the connectors ruptured, but there was permanent axial deformation due to their yielding.

At 3% drift, diagonal cracks and uplift of the deck occurred over the flange of girder 1, while only slight deck separation was observed over girder 3. This indicated that at this drift level, the deck-girder joint connections over girders 1 and 2 had reached their ultimate capacity, while the full connection capacity was not yet developed over girder 3. This is evident in Figure 14, where the deformation and damage in Specimen F0A at 5% drift is shown.

Figure 15 shows the middle girder before and after the test. In addition to the diagonal cracks at the deck-girder joint connection, there was significant plastic deformation at the connections of the top and bottom chords to the gusset plates. The concrete breakout cones around the connector groups were visible during the deck demolition. At the end of the experiment, fractures were observed on the bottom chord at the first bolt-hole connection to the gusset plate. This is attributed to the low cycle fatigue due to high plastic strains in the angles near the connections.

Sequence of Yielding and Failure Modes

Figure 16 shows the envelope of base shear versus girder differential displacement. Examination of the strain gage data indicate that the ends of the chord members started to yield early on into the experiment at about 0.5% drift. The strains in the chords started to plateau between 1% to 1.5% drift. At this instance, the deck started to resist the lateral force through bending due to framing action with the girders, which led to the formation of visible flexural cracks in the deck. The strains in the chord increased at 1.5% to 2% drift as the connection between the deck and girder 2 fails. This caused redistribution of forces to girders 1 and 3.

Figure 17 shows the base shear plotted against the peak rotation of the deck-girder joints. This shows that the joint over girder 3 remained elastic up to 2% drift and experienced little nonlinearity before overall failure of the specimen occurred. The figure also shows that concrete joint over girders 1 and 2 underwent large rotations (0.05 rad.) before failure. Despite the failure of the concrete joint over girder 2 and its inability to transfer bending moments, the deck remained attached to the top flange of the girder 2 through the continuous bottom rebar mesh.

Cyclic Response of Specimen F0B

Figure 18 shows the lateral cyclic load-displacement response of specimen F0B in terms of total force versus the differential transverse displacement between the top and bottom flanges of the plate girders. The test showed that the ultimate, lateral load-carrying capacity of the specimen was 65 kips, the lateral drift capacity was 7% and the initial lateral stiffness of the specimens was 255 kips/in.

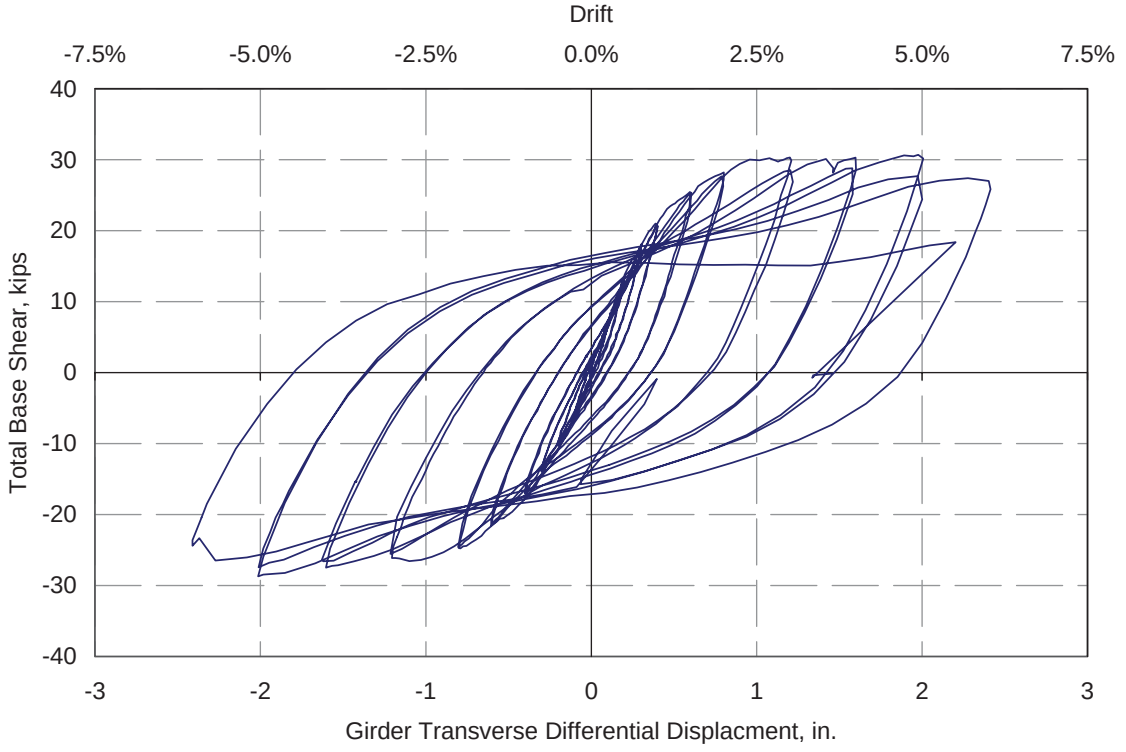

Fig. 13. Specimen F0A: actuator force versus girder differential displacement.

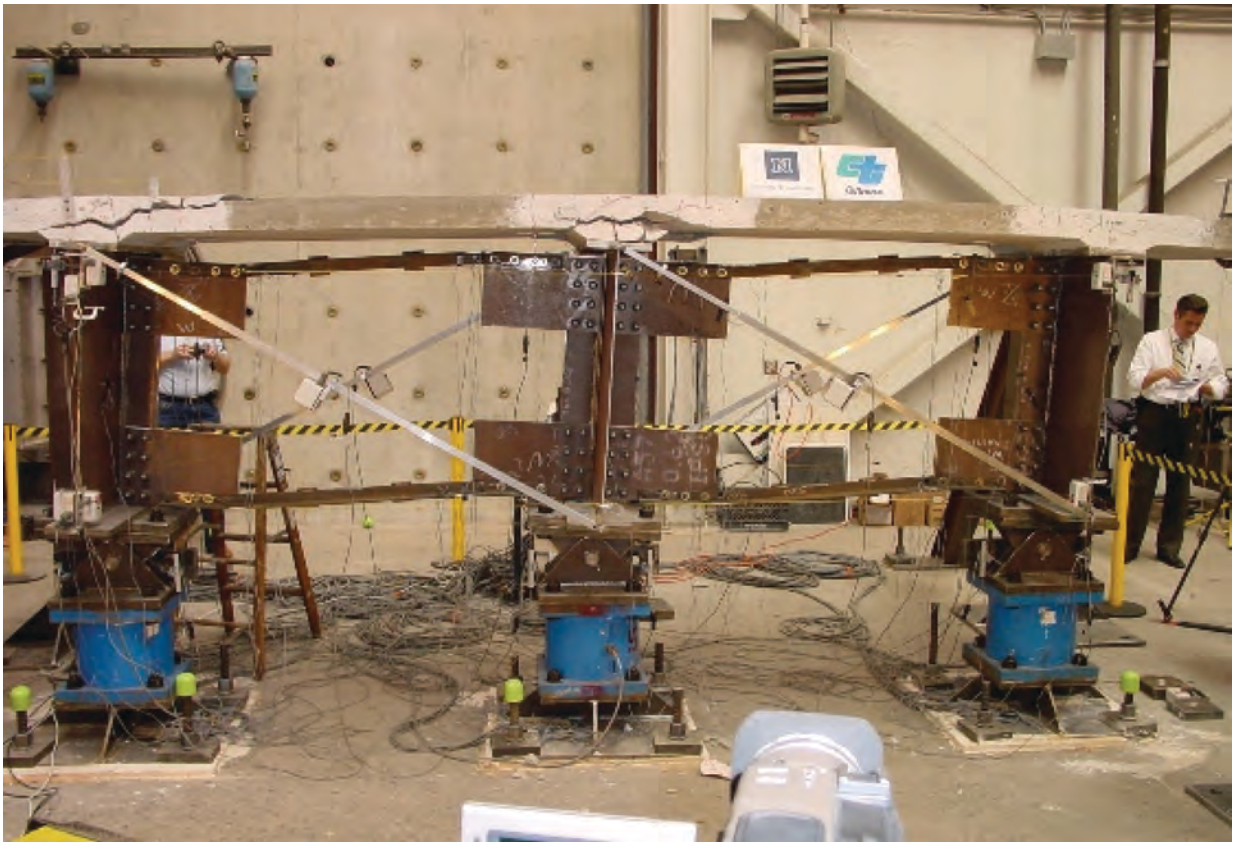

Fig. 14. Specimen F0A: deformation and damage at 5% drift.

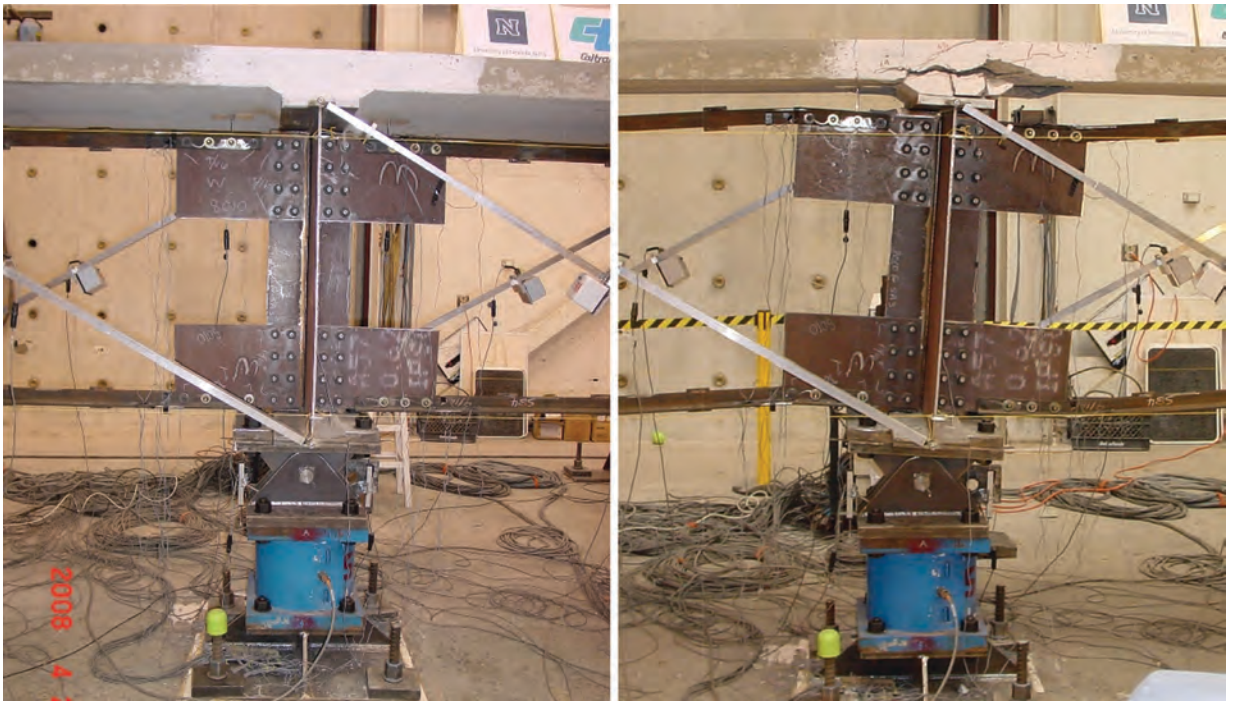

Fig. 15. Specimen F0A: comparison of deformed and undeformed shape of middle girder (girder 2).

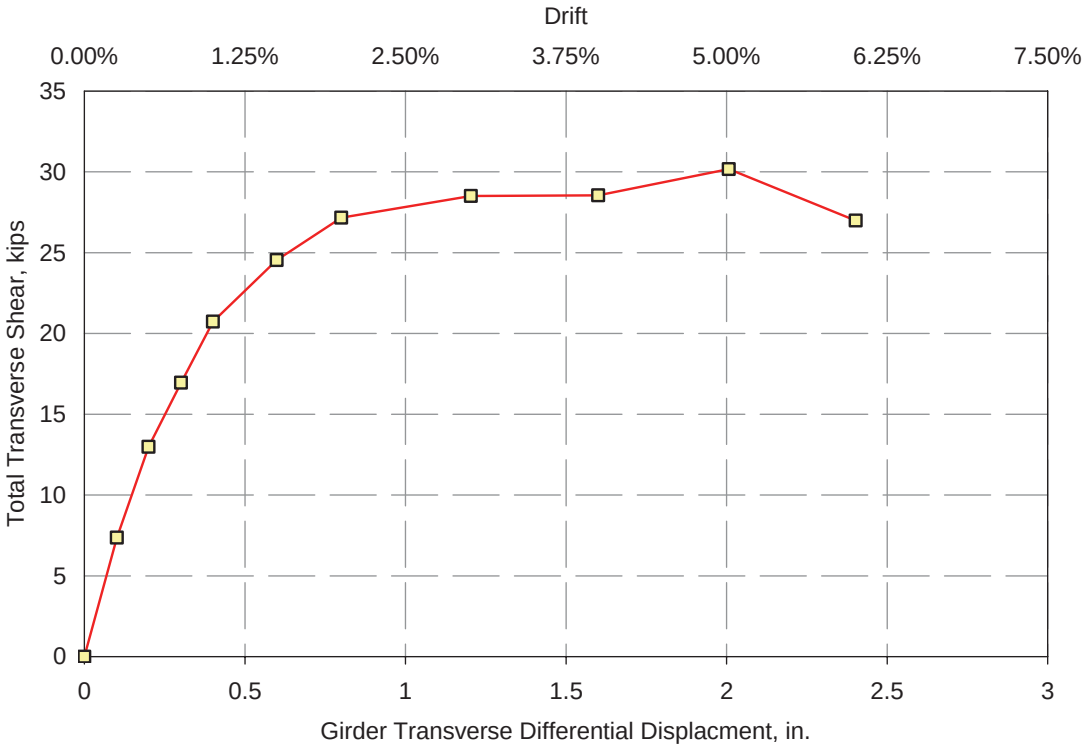

Fig. 16. Specimen F0A: base shear force-displacement plot.

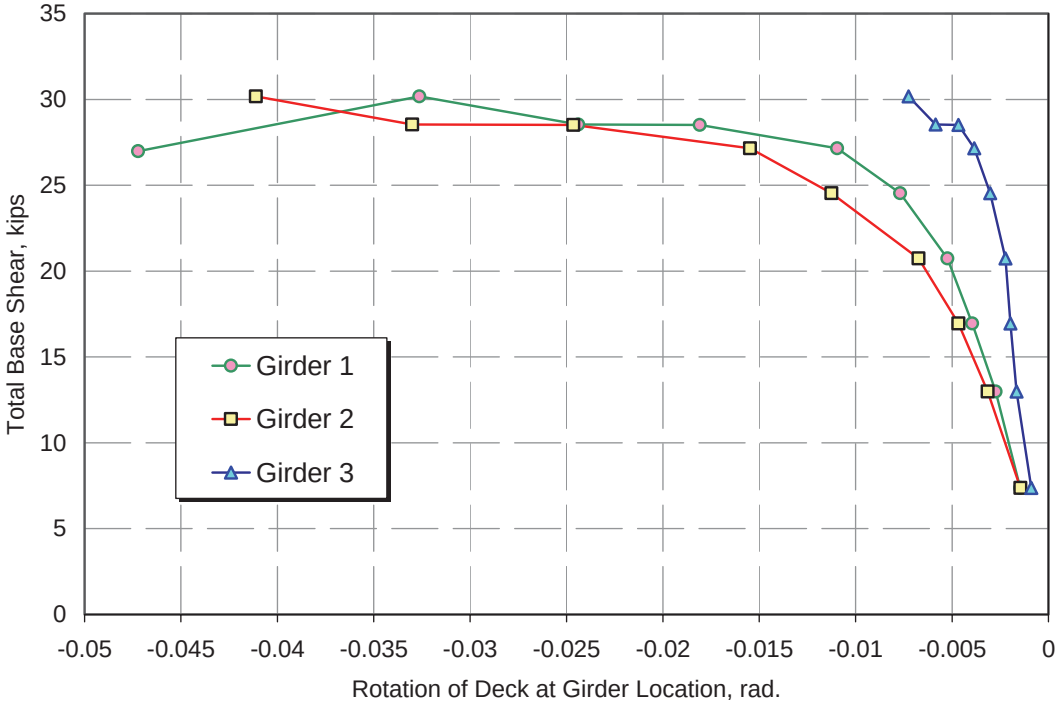

Fig. 17. Specimen F0A: base shear versus rotation of deck-girder joints.

Experimental Observations

Up to 0.75% drift, transverse cracks were developed across the deck. These cracks were due to flexural deformation of the deck. At 1% drift, cracks running north–south (i.e., in the direction of girder 1 to girder 3) on the deck surface were observed. At 1.5% drift, the ends of the chords showed separation from the concrete deck, indicating yielding of stud connectors in this area. At 2% drift, the deck-girder joint started to fail, and the deck started to separate (lift up) from the flanges of girders 2 and 3.

At 3% drift, the stud connectors close to the ends of the top chords ruptured due to high tension forces. Also, at this drift level, concrete breakout mode of failure started to occur in the deck-girder joint. High plastic rotation occurred at the ends of the chord members.

Figure 19 shows the deformation of specimen F0B at 6% drift. Vertical gaps (separations) and horizontal offsets between the underside of the deck and top flanges of the steel girders can be observed. Several factors contributed to this separation of the concrete deck and steel girder. This is attributed to the failure of stud connectors over girder 2, which caused the entire deck to bend in a single curvature between girders 1 and 3.

Due to the relatively large flexural stiffness of the thickened reinforced concrete deck at the connection with the top chord, large rotations that were concentrated on the top chord occurred near the ends of this connection. Figure 20 shows the separation between the deck and top chord. This separation caused high axial forces in the exterior stud connectors (i.e., connectors that were close to the ends of the deck–top chord connection). As these connectors fail, the connectors next in line and closer to the middle of the chords started to pick up the unbalanced force. At the end of the test, all the stud connectors over the top chords were ruptured, and significant plastic deformation in the top chords was visible. Additionally, the top chords were ruptured at the location of the last bolt hole due to high plastic strain concentration and low cycle fatigue.

Sequence of Yielding and Failure Modes

Figure 21 shows the envelope of base shear force versus girder differential displacement. The specimen exhibited larger elastic stiffness and yield strength compared with specimen F0A. Examination of the strain gages indicated that the ends of the chord members started yielding at 0.5% drift. As the transverse displacement is increased, the strains in the chords also increased, with corresponding increase in lateral force. The lateral stiffness and strength of the specimen dropped significantly when the top chords started yielding. The significant drop in strength shown in Figure 21 was due to fracture of the chord members near the connection to the gusset plate and failure of the stud

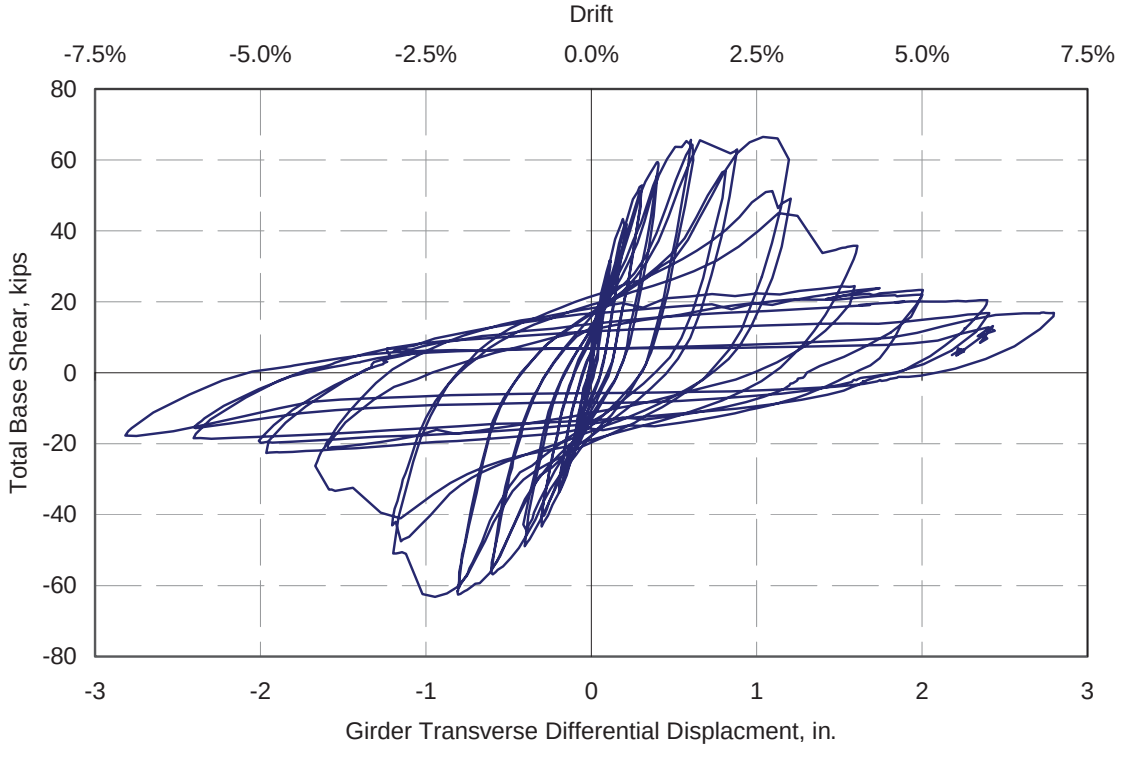

Fig. 18. Specimen F0B: actuator force versus girder differential displacement.

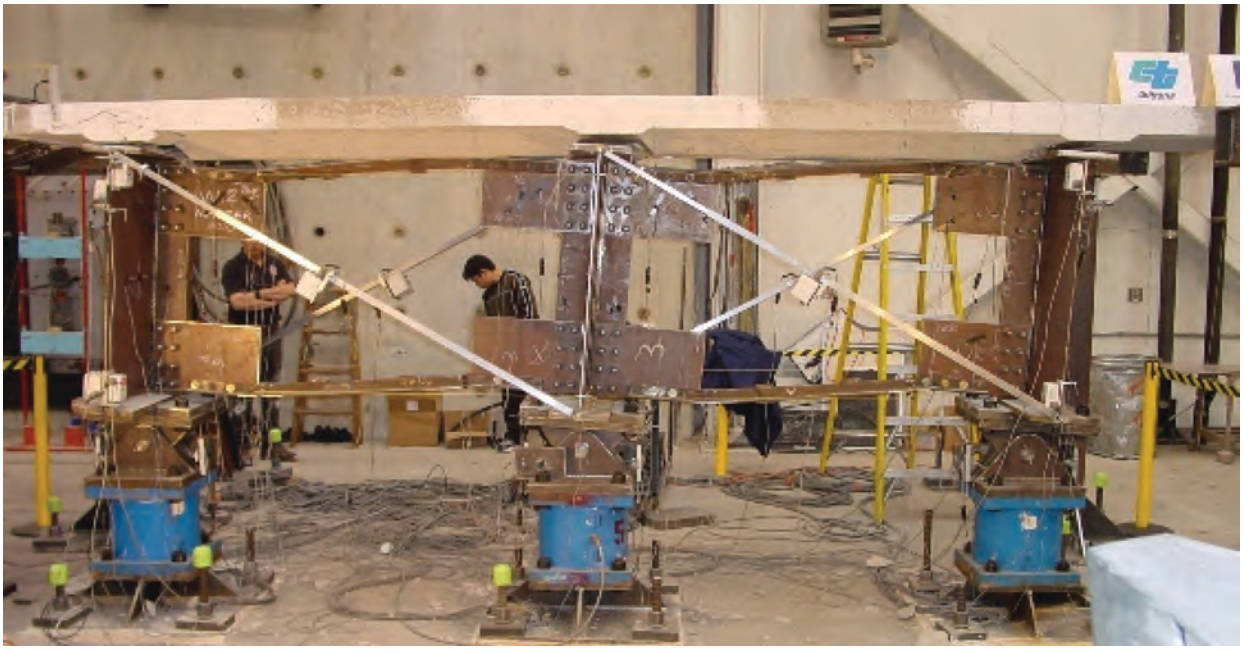

Fig. 19. Specimen F0B: deformed shape at 6% drift.

Fig. 20. Specimen F0B: rupture of stud connectors near the end of the top chord.

connectors. Although the specimen was able to resist higher lateral force and maintain higher lateral drift capacity, the deck experienced some damage.

LIMIT STATES OF TEST SPECIMENS

Based on these experiments, it was clear that stud connectors were subjected to combined shear and tension forces. Therefore, the interaction equation in Appendix D of ACI 318-08 (ACI, 2008) was used to better estimate their resistance under this combined loading. The strength of headed stud connector is given by:

$$\left(\frac{N_u}{N_r}\right)^{5/3} + \left(\frac{Q_u}{Q_r}\right)^{5/3} \leq 1.0 \qquad (1)$$

where N_u is the seismic axial force demand per connector, Q_u is the seismic shear force demand per connector, N_r is the factored tensile capacity of a single connector and Q_r is the factored shear capacity of a connector. The tensile capacity is determined based on the lesser of stud connector ultimate axial capacity or concrete breakout capacity. The concrete breakout typically governs the design when the haunch is unreinforced. This can be improved by providing reinforcement around the stud connectors. This is evident in specimen F0B, where failure was due to stud fracture instead of concrete breakout. The ACI equations were used to determine the lateral strength of both specimens.

Specimen F0A

The lateral resistance of specimen F0A can be evaluated by dividing the subassembly into two framing systems: (1) the framing system formed by the deck and the girder and (2) the framing system formed by the chord members and the girders. The capacity in the first framing system is governed by the deck-girder joint connection capacity while, in the second, it is governed by moment capacities of the chord members.

A schematic diagram of lateral deformation of specimen 0A is shown in Figure 22. Based on the rotation of the deck-girder joint shown in Figure 22b, it can be assumed that one line of stud connectors is under compression while the other two lines are under tension. These sets of forces can, therefore, be used to calculate the moment in the connection. Using the ACI equations, the breakout strength of the group of connectors under tension is 38.9 kips. Because there are 10 connectors in this group, breakout strength of each connector is 3.9 kips. The tensile capacity of each connector is 8.8 kips. Therefore, the limit state of these connectors is based on concrete breakout, which is similar to the observed failure in the experiment. Based on 2.5-in.

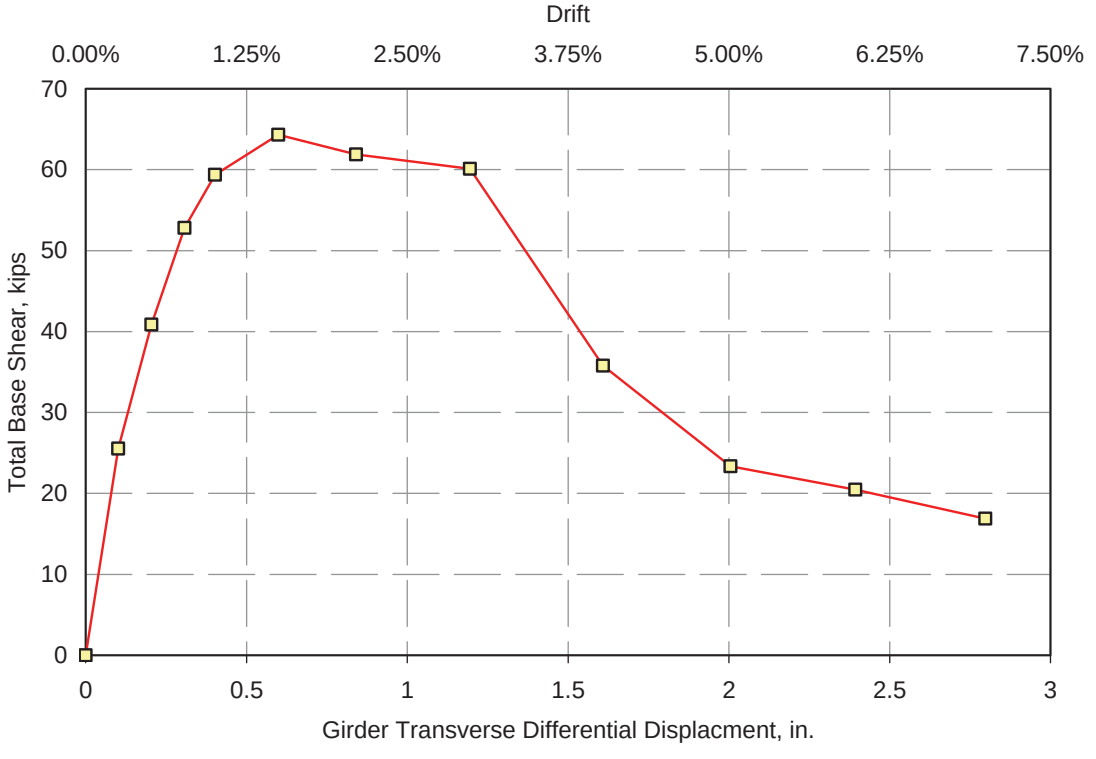

Fig. 21. Specimen F0B: base shear force-displacement plot.

transverse spacing between the connectors, the moment capacity of each deck-girder connection is equal to 145.9 kip-in. Because these moments act at the top of each girder, the lateral capacity provided by each connection can be calculated by dividing the moment capacity by the height from the top of girder to the centerline of the bearings, which is 48 in. The lateral capacity per girder is equal to 3.0 kips, and for the subassembly, it is equal to 9.0 kips.

The chord plastic moment capacity is 68 kip-in. based on a plastic section modulus of 1.27 in^3 and a measured yield strength of 54 ksi. The plastic hinges occur near the connection of the chord members to the gusset plates. The calculated lateral capacity due to the plastic moments is equal to 21.6 kips.

Therefore, the total lateral capacity of the subassembly based on combined capacity due to deck-girder frame action (9.0 kips) and chord-girder frame action (21.6 kips) is 30.6 kips. This calculated capacity closely match the experimental results of 30 kips as shown in Figure 16.

Specimen F0B

A schematic diagram of lateral deformation of specimen F0B is shown in Figure 23. The lateral force transfer mechanism in this model was mainly through the stud connectors connecting the deck to the top chord. The contribution of the deck-girder frame to the lateral capacity was considered negligible due to the small number of stud connectors on the girder top flange and because these connectors were placed 12 in. away from the centerline of subassembly as discussed previously. The degradation of the deck–top chord connection was due to high axial loads developed in the stud connectors, particularly at the ends of the connection, as illustrated in Figure 23b. In the experiment, it was observed that the limit state of the stud connectors at this location was fracture. This is because the connectors were subjected to large axial forces and deformations as the top chords deforms in flexure (Figure 23b).

The deck–top chord connection created a flexurally stiff composite section, which made specimen F0B stiffer than specimen F0A. It was shown in the experiment that the lateral stiffness of specimen F0B is more than three times the stiffness of specimen F0A.

Unlike in specimen F0A, a simplified model is not sufficient to evaluate the lateral capacity of specimen F0B due to distributed nonlinearity in the deck–top chord connection and flexural flexibility of the composite section of the top chord and deck. Therefore, a finite element model was developed to capture its response. Figure 24 shows the analytical model developed in SAP2000 (CSI, 2010). The deck, girders, stiffeners and gusset plates were modeled as shell elements while the stud connectors and chord members were modeled using frame elements. The connectors were modeled

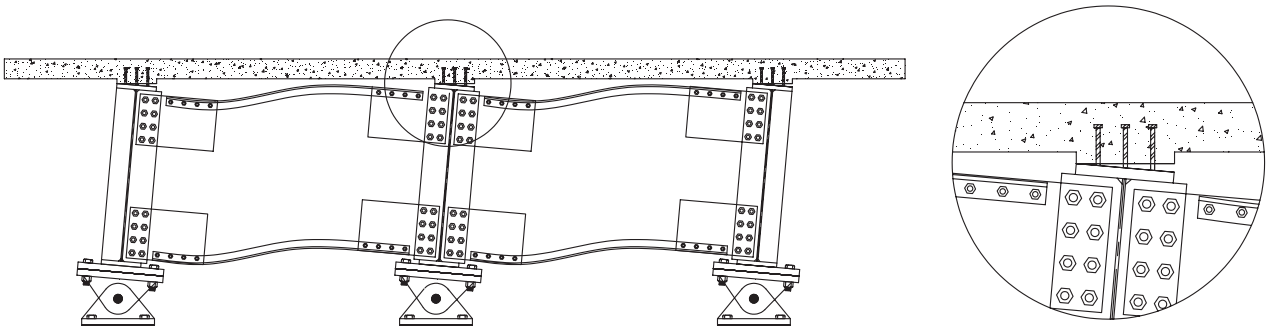

Fig. 22. Specimen F0A: (a) deformed shape of subassembly; (b) rotation at deck-girder joint.

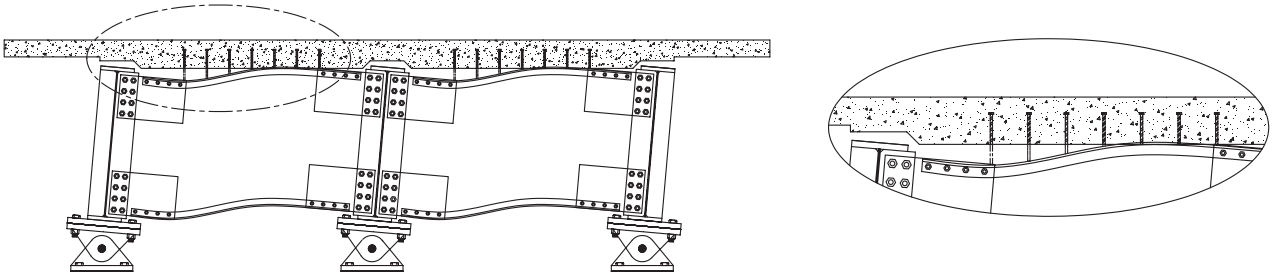

Fig. 23. Specimen F0B: (a) deformed shape of subassembly; (b) close-up of deformation at deck–top chord connection.

based on the truss analogy method developed by Bahrami, Itani and Buckle (2009). Plastic hinges were assigned to the chord elements near the connections. Figure 25 shows the pushover curve of the model compared with the envelope of base shear values at peak displacement cycles. The figure shows good correlation between the curves. The difference is attributed to the degradation of stiffness and strength in the deck–top chord connection.

SEISMIC DESIGN OF STEEL PLATE GIRDER SUPERSTRUCTURE

The findings of the preceding experiment, previous experimental and analytical investigations by other researchers and damage observed from earthquakes were used to develop a set of guidelines and specifications for seismic design of steel plate girder bridges (Itani, Grubb and Monzon, 2010). These have been adopted in the 2012 AASHTO LRFD Bridge Design Specifications (AASHTO, 2012) under the new Article 6.16, "Provisions for Seismic Design." These specifications concentrate on the seismic design and detailing of steel plate girder bridge superstructures. The common thread among these investigations was that these types of superstructures are vulnerable during earthquakes if they are not designed and detailed to resist the resulting seismic forces. A continuous and clearly defined load path is necessary for the transmission of the superstructure inertia forces to the substructure. The new specifications cover the design and detailing of reinforced concrete deck, stud connectors and cross frames and their connections.

SUMMARY AND CONCLUSIONS

Analytical investigations performed on steel plate girder superstructures showed that stud connectors are subjected to combined axial tensile and shear forces during seismic events. These forces are particularly large at the support locations, where the superstructure seismic forces are transferred to the substructure. As such, these connectors, if not designed properly, may fail prematurely during large earthquakes, altering the load path and subjecting other bridge components—such as intermediate cross frames—to forces for which they were designed. To verify this observation, two half-scale models of subassembly representing the deck, girder and chord members at the supports were constructed and subjected to cyclic testing. The test specimens represented two different configurations of transferring the deck seismic forces to the bearings and substructures: (1) the deck is connected to the girder top flange, and (2) the deck is connected to the top chords of the cross frames. Based on this study, the following observations and conclusions can be made:

- Stud connectors at support locations are essential in transferring the seismic forces to the cross frames.
- Seismic forces subject the stud connectors at support locations to combined axial tension and shear forces.
- Connecting the deck to the top chord at the supports increased the lateral stiffness and lateral strength of steel plate girder superstructure.

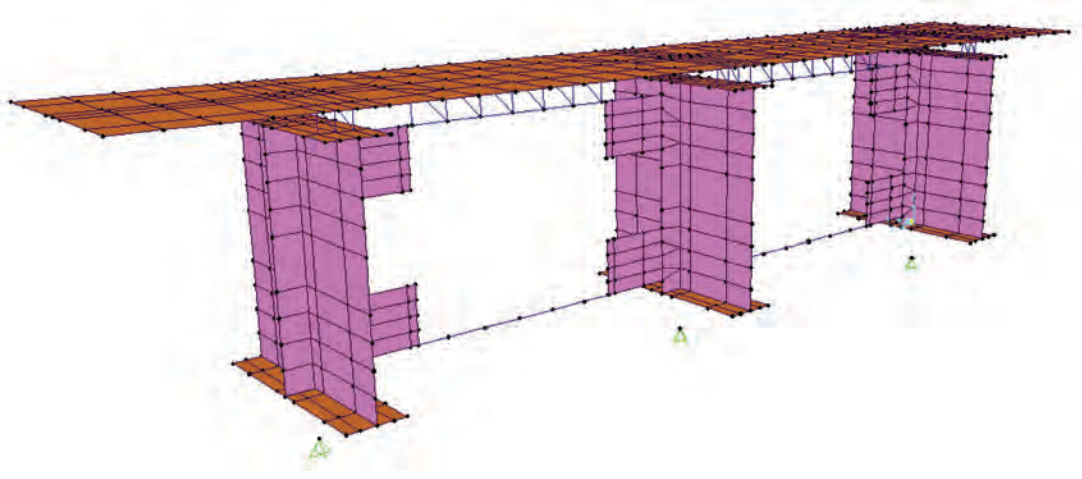

Fig. 24. Finite element model of specimen F0B.

- Interaction equation for stud connector resistance adopted in the new Article 6.16, "Provisions for Seismic Design," of the 2012 AASHTO LRFD Bridge Design Specifications must be used in seismic design of the connection between the reinforced concrete deck and the steel plate girder superstructure.

These observations and conclusions apply only to steel girder bridges with a drop cap. For steel girder bridges with an integral pier cap connection, design of stud connectors at the support is not required. The deck seismic forces are transferred directly from the deck to the concrete diaphragm and then to the substructure.

REFERENCES

AASHTO (2008). *AASHTO LRFD Bridge Design Specifications*, American Association of State Highway and Transportation Officials (AASHTO), Washington, DC.

AASHTO (2012). *AASHTO LRFD Bridge Design Specifications*, American Association of State Highway and Transportation Officials (AASHTO), Washington, DC.

ACI (2008). *Building Code Requirements for Structural Concrete (ACI 318-08) and Commentary*, American Concrete Institute (ACI), Farmington Hills, MI.

AISC (2005). *Seismic Provisions for Structural Steel Buildings*, American Institute of Steel Construction (AISC), Chicago, IL.

Bahrami, H., Itani, A.M. and Buckle, I.G. (2009). "Guidelines for the Seismic Design of Ductile End Cross-Frames in Steel Girder Bridge Superstructures," CCEER Report No. 09-04, Center for Civil Engineering Earthquake Research, University of Nevada, Reno, NV.

Caltrans (1992). "PEQIT Report-Highway Bridge Damage—Petrolia Earthquakes No. 1, No. 2, No. 3. of April 25–26, 1992," California Department of Transportation (Caltrans), Sacramento, CA.

Caltrans (2007). *Steel Girder Bridge Design Example,* AASHTO-LRFD, 3rd ed., with California Amendments, California Department of Transportation (Caltrans), Sacramento, CA.

Carden, L.P., Itani, A.M. and Buckle, I.G. (2005). "Seismic Load Path in Steel Girder Bridge Superstructures," CCEER Report No. 05-03, Center for Civil Engineering Earthquake Research, University of Nevada, Reno, NV.

CSI. (2010). SAP2000, Computers and Structures Inc., Berkeley, CA.

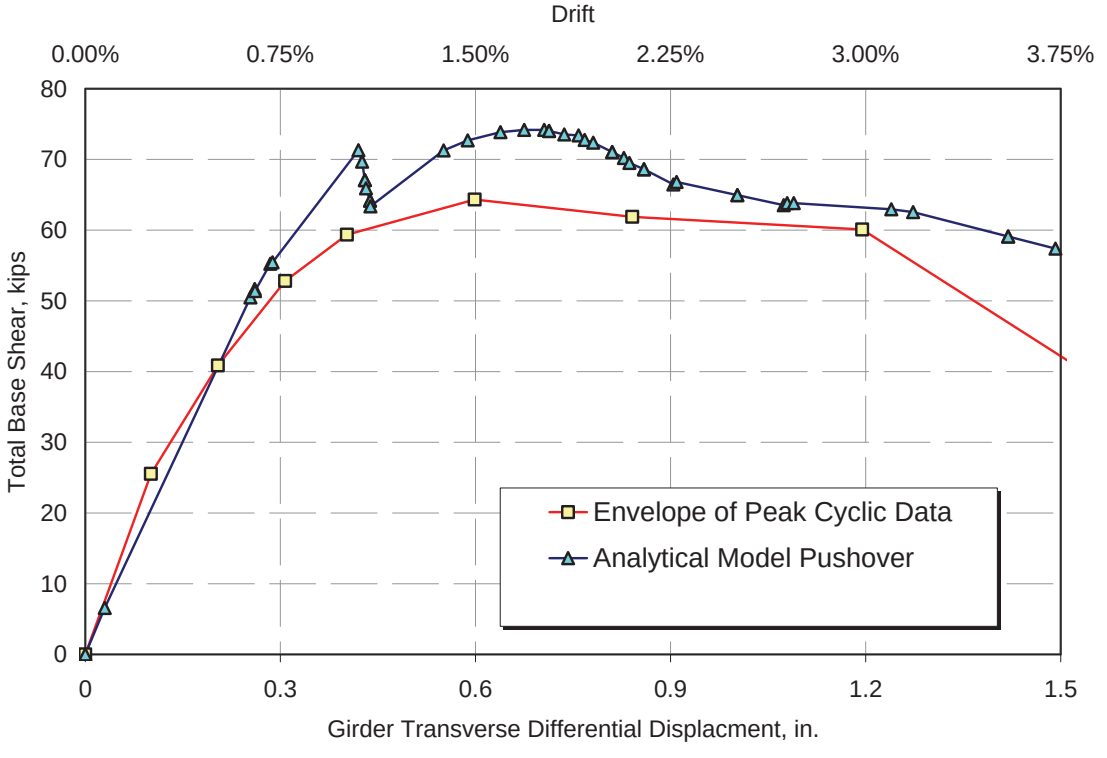

Fig. 25. Comparison of specimen F0B analytical model pushover result and experiment.

Gattesco, N. and Giuriani, E. (1996). "Experimental Study on Stud Shear Connectors Subjected to Cyclic Loading," *Journal of Constructional Steel Research*, Vol. 38, no. 1, pp. 1–21.

Hawkins, N.M. and Mitchell, D. (1984). "Seismic Response of Composite Shear Connections," *Journal of Structural Engineering*, Vol. 110, pp. 2120–2136.

Itani, A.M., Grubb, M. and Monzon, E.V. (2010). "Proposed Seismic Provisions and Commentary for Steel Plate Girder Superstructures," CCEER Report No. 10-03, Center for Civil Engineering Earthquake Research, University of Nevada, Reno, NV.

Lloyd, R.M. and Wright, H.D. (1990). "Shear Connection between Composite Slabs and Steel Beams," *Journal of Constructional Steel Research,* Vol. 15, No. 4, pp. 255–285.

McMullin, K.M. and Astaneh-Asl, A. (1994). "Cyclic Behavior of Welded Shear Studs," *Proceedings of Structures Congress XII*, Atlanta, GA. April 24–28.

Mouras, J.M., Sutton, J.P., Frank, K.H. and Williamson, E.B. (2008). "The Tensile Capacity of Welded Shear Studs," Report 9-5498-R2, Center for Transportation Research at the University of Texas, Austin, TX.

Oehlers, D.J. (1995). "Design and Assessment of Shear Connectors in Composite Bridge Beams," *Journal of Structural Engineering*, Vol. 121, No. 2, pp. 214–224.

Oehlers, D.J. and Johnson, R.P. (1987). "The Strength of Stud Shear Connections in Composite Beams," *The Structural Engineer*, Vol. 65B, No. 2, pp. 44–48.

Ollgaard, J.G., Slutter R.G. and Fisher, J.W. (1971). "Shear Strength of Stud Connectors in Lightweight and Normal-Weight Concrete," *Engineering Journal*, AISC, Vol. 8, pp. 55–64.

Seracino, R., Oehlers, D.J. and Yeo, M.F. (2003). "Behavior of Stud Shear Connectors Subjected to Bi-Directional Cyclic Loading," *Advances in Structural Engineering*, Vol. 6, No. 1, pp. 65–75.

GUIDE FOR AUTHORS

SCOPE: The ENGINEERING JOURNAL is dedicated to the improvement and advancement of steel construction. Its pages are open to all who wish to report on new developments or techniques in steel design, research, the design and/or construction of new projects, steel fabrication methods, or new products of significance to the uses of steel in construction. Only original papers should be submitted.

GENERAL: Papers intended for publication may be submitted by mail to the Editor, Keith Grubb, ENGINEERING JOURNAL, AMERICAN INSTITUTE OF STEEL CONSTRUCTION, One East Wacker Drive, Suite 700, Chicago, IL, 60601, or by email to grubb@aisc.org.

The articles published in the *Engineering Journal* undergo peer review before publication for (1) originality of contribution; (2) technical value to the steel construction community; (3) proper credit to others working in the same area; (4) prior publication of the material; and (5) justification of the conclusion based on the report.

All papers within the scope outlined above will be reviewed by engineers selected from among AISC, industry, design firms, and universities. The standard review process includes outside review by an average of three reviewers, who are experts in their respective technical area, and volunteers in the program. Papers not accepted will not be returned to the author. Published papers become the property of the American Institute of Steel Construction and are protected by appropriate copyrights. No proofs will be sent to authors. Each author receives three copies of the issue in which his contribution appears.

MANUSCRIPT PREPARATION: Manuscripts must be provided in Microsoft Word format. Include a PDF with your submittal. View our complete author guidelines at **www.aisc.org/ej**.

There's always a solution in steel.

ENGINEERING JOURNAL
American Institute of Steel Construction
One East Wacker Drive, Suite 700
Chicago, IL 60601

312.670.2400 www.aisc.org